

N  
55

L.P. Jester.

ED33

REMTECH

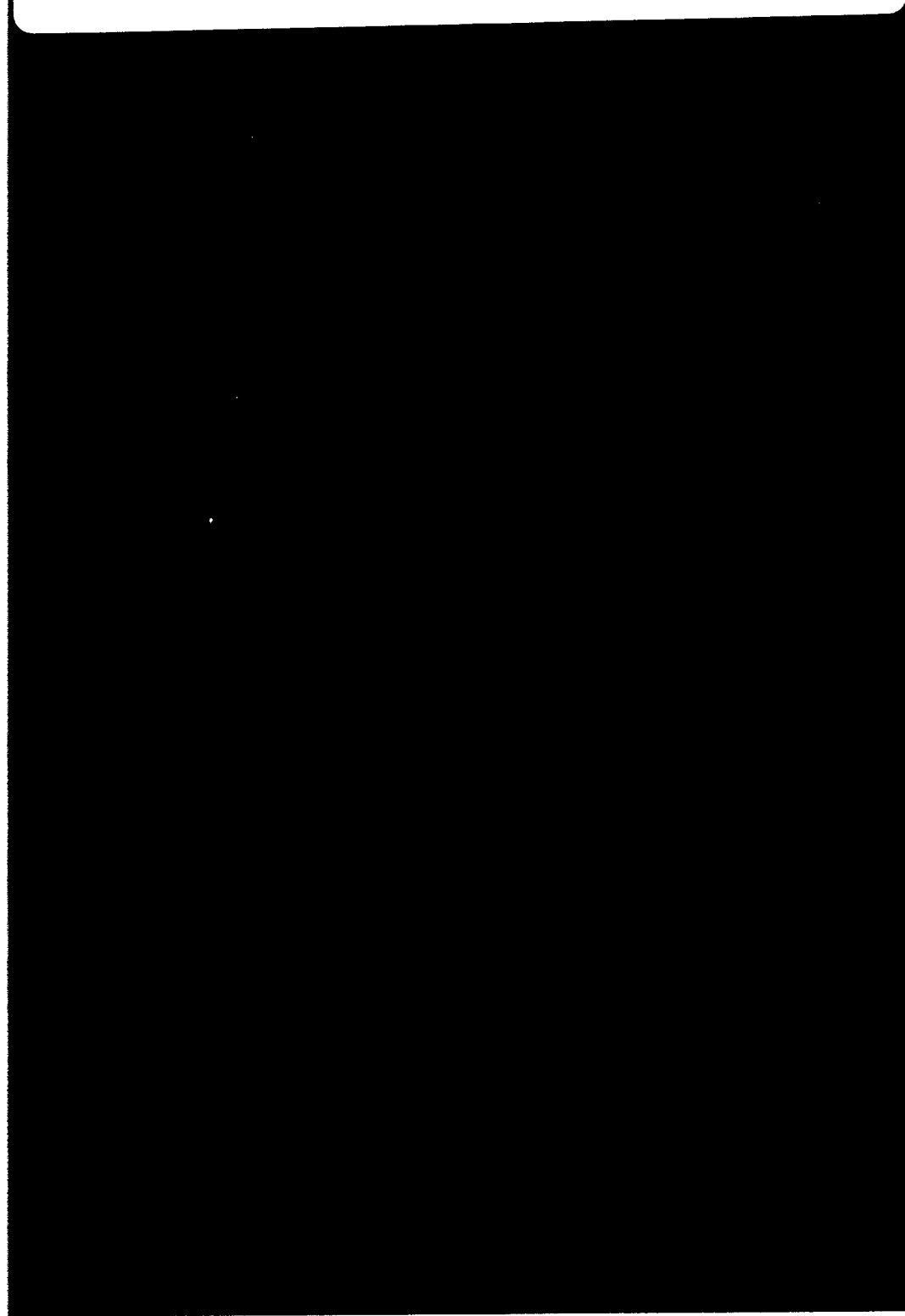
RTR 227-01

(NASA-CR-199514) EXTERNAL TANK  
AEROTHERMAL DESIGN CRITERIA  
VERIFICATION Final Report  
(Remtech) 80 p

N93-25055

Unclas

G3/18 0163032



## FOREWORD

This final report presents work conducted for the Marshall Space Flight Center (MSFC), National Aeronautics and Space Administration, in response to the requirements of Contract NAS8-38185. The work presented here was performed by REMTECH inc., Huntsville, AL, and is titled "External Tank Aerothermal Design Criteria Verification."

The project manager for this project was Dr. Sarat C. Prahraj. The NASA contract monitor for this project was Mr. Lee D. Foster, ED33, of the Induced Environments Branch of the Aerophysics Division.

## ABSTRACT

If an SSME fails during the initial 160 seconds of the Shuttle flight, a return-to-launch-site maneuver will be implemented. The period of concern for this task is the pitch-around maneuver when the vehicle is flying backward. The intent of this report is to identify and define the flowfield at the most critical locations from an environment perspective. The solution procedure used to predict the plume heating rates involves both computational analysis and engineering modeling.

## Contents

FOREWORD . . . . .	i
ABSTRACT . . . . .	ii
List of Figures . . . . .	iv
List of Tables . . . . .	iv
Nomenclature . . . . .	v
1 INTRODUCTION . . . . .	1
2 MODELING FOR ABORT CASES . . . . .	6
2.1 Trajectories . . . . .	6
2.2 CFD Modeling . . . . .	6
2.3 Engineering Modeling (Heating Indicator Approach) . . . . .	13
3 GENERATION OF ABORT ENVIRONMENTS . . . . .	16
4 CONCLUSIONS AND RECOMMENDATIONS . . . . .	21
4.1 Conclusions . . . . .	21
4.2 Recommendations . . . . .	21
5 REFERENCES . . . . .	23
Appendix A Two-Species Variable Gamma Formulation for a Forward-Firing Rocket Nozzle . . . . .	24
Appendix B Variable Gamma Computations for a Forward-Firing Space Shuttle Main Engine . . . . .	52

## List of Figures

1	Return-to-Launch-Site (RTLS) Abort Profile . . . . .	2
2	RTLS Trajectory: Altitude vs. Time . . . . .	3
3	RTLS Trajectory: Angle-of-Attack vs. Time . . . . .	4
4	RTLS Flight Path Positions . . . . .	5
5	SSME #1 Out Generic RTLS/PPA Trajectory Altitude Profile . . . . .	10
6	SSME #1 Out Generic RTLS/PPA Trajectory Angle-of-Attack Profile . . . . .	11
7	SSME #1 Out Generic RTLS/PPA Trajectory Mach Number Profile . . . . .	12
8	Correlation of Stagnation Heating Rate Plume Parameter with Radius . . . . .	14
9	Altitude-Velocity Profiles for PPA Maneuver . . . . .	17
10	Heating Rate History for Aeroheating Trajectory . . . . .	18
11	Heating Rate History for Plume Heating Trajectory . . . . .	19

## List of Tables

1	Generic RTLS Plume Trajectory with SSME #1 Out (With Pitot Pressure) . . . . .	7
---	--	---

## Nomenclature

$\mu$	Viscosity
$p_s$	Stagnation pressure
$\dot{q}$	Heating rate
$c_p, c_v$	Specific heats at constant pressure and volume, respectively
$R_{eff}$	Effective radius
$k$	Stagnation heating rate plume parameter
$M$	Mach number
$Nu$	Nusselt number
$St$	Stanton number
$T$	Temperature
$t$	Time
$H$	Enthalpy
$R$	Gas constant
$c$	Species mass fraction
$\rho$	Density
$a$	Speed of sound
$\gamma$	Ratio of specific heats
$e$	Energy per unit mass
$D_{ij}$	Diffusion coefficient
$V_i$	Diffusion velocity
$h$	Enthalpy per unit mass
$Re$	Reynolds number
$Sc$	Schmidt number

### Subscripts

$c$	Continuum
$FM$	Free molecular
$\infty$	Free stream
$m$	Mixture
$int$	Internal
$t$	Total
$i$	Species $i$

### Superscripts

$\hat{\quad}$	Universal (gas constant)
$\bar{\quad}$	Normalized

## Section 1 INTRODUCTION

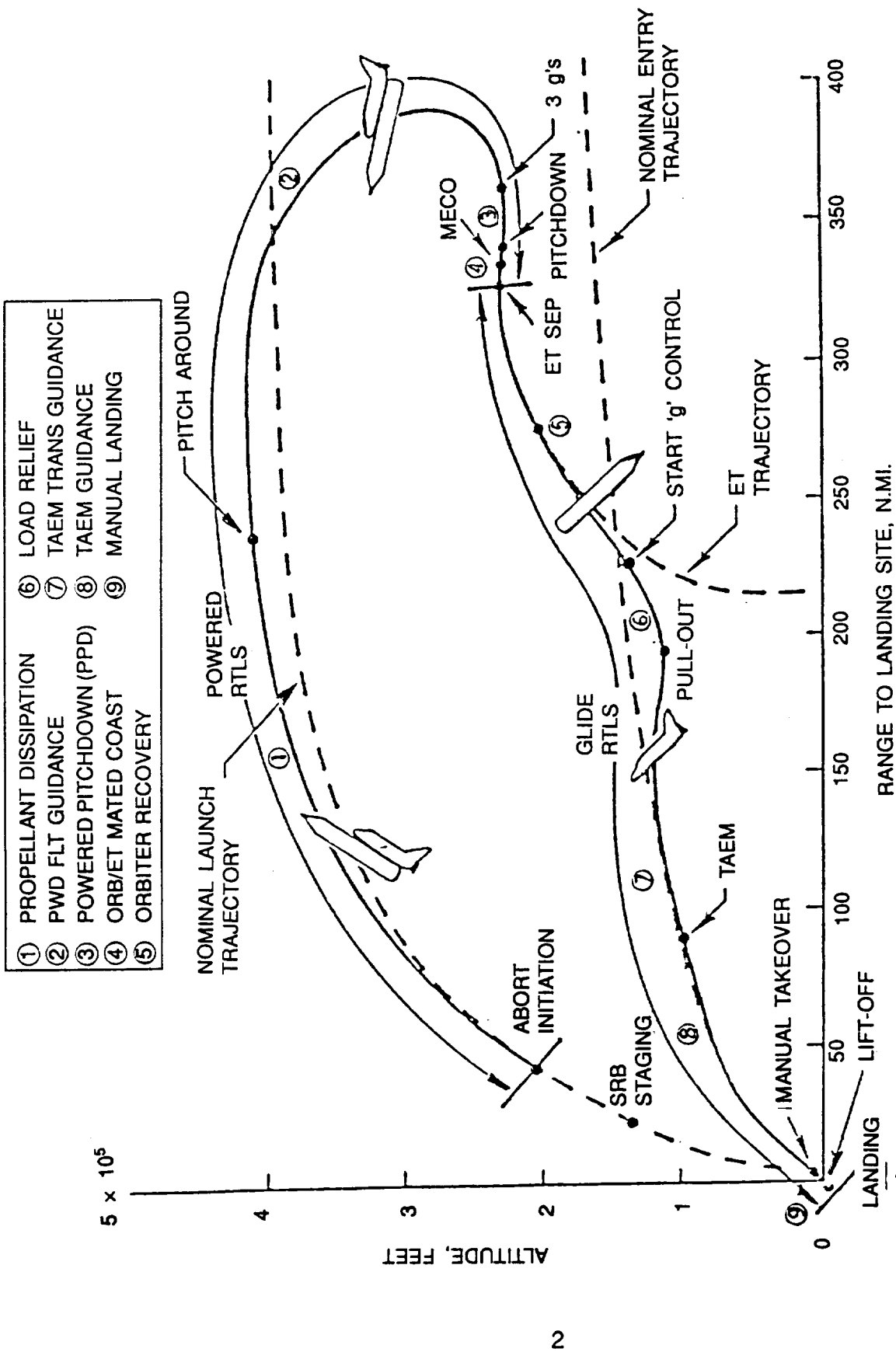
If an SSME fails during the initial 160 seconds of flight, a return-to-launch-site (RTLS) maneuver will be implemented as shown in Fig. 1. The period of concern for this task is the pitch-around maneuver where the vehicle is flying backward. Typical altitude and angle-of-attack histories during this portion of flight are shown in Figs. 2 and 3, respectively. Several distinct points have been identified during the turnaround maneuver. These points correspond to flight path directions on Fig. 4 where the estimated plume boundary and shock location for position F, flying backward, are given. Thus, to define the plume with a CFD analysis will require a large grid structure. At positions C and H, the free-stream flow along the plume boundary will produce a shear layer which may impinge on the ET and orbiter.

Three flight path positions were chosen for CFD analysis. Currently, the three positions which were selected are:

- Position C: High Mach number, possible shear layer impingement along plume boundary.
- Position F: Flying backward, simplest applied case where plume is axisymmetric, similar to validation case.
- Position H: Low altitude, low Mach number, possible shear layer impingement along plume boundary.

The intent is to identify and define the flowfield at the most critical locations from an environment perspective. The boundary of the plume will generate a plume shock which will affect the airflow over the vehicle, hence, its stability. Plume/air mixture ratios will also vary depending upon the location of the vehicle in its trajectory, and this has a strong influence on the heat load to the vehicle, specifically to the ET and Orbiter. Heating due to aerodynamic frictional heating is dominant if plume impingement is negligible. However, a large portion of the hot plume will be forced back to the vehicle due to the vehicle's orientation against the oncoming free stream. Therefore, the most critical location from a heating concern is associated with the greatest plume impingement. The solution procedure used to predict the plume heating rates involves computational analysis (CFD) and engineering modeling (heating indicator approach).

Following this section, Section 2 details the trajectory used for the RTLS maneuver and the modeling (both CFD and engineering) needed to determine the flowfield. Section 3 discusses the procedure for generating abort environments and provides the environments for appropriate body points. Section 4 provided the conclusions reached by the Thermal Panel and makes a set of useful recommendations for future work.



Return-to-launch-site (RTLS) abort profile is illustrated. Dotted line shows a normal ascent and normal reentry profile in comparison with the profile that would be flown should an emergency occur forcing an RTLS during about the first 262 sec of flight. Pitch-around maneuver is timed for proper main engine cutoff (MECO) timing followed by external tank (ET) separation from the orbiter. Terminal area energy management phase (TAEM) portion of the abort has tight dynamic loading margins.

Figure 1: Return-to-Launch-Site (RTLS) Abort Profile



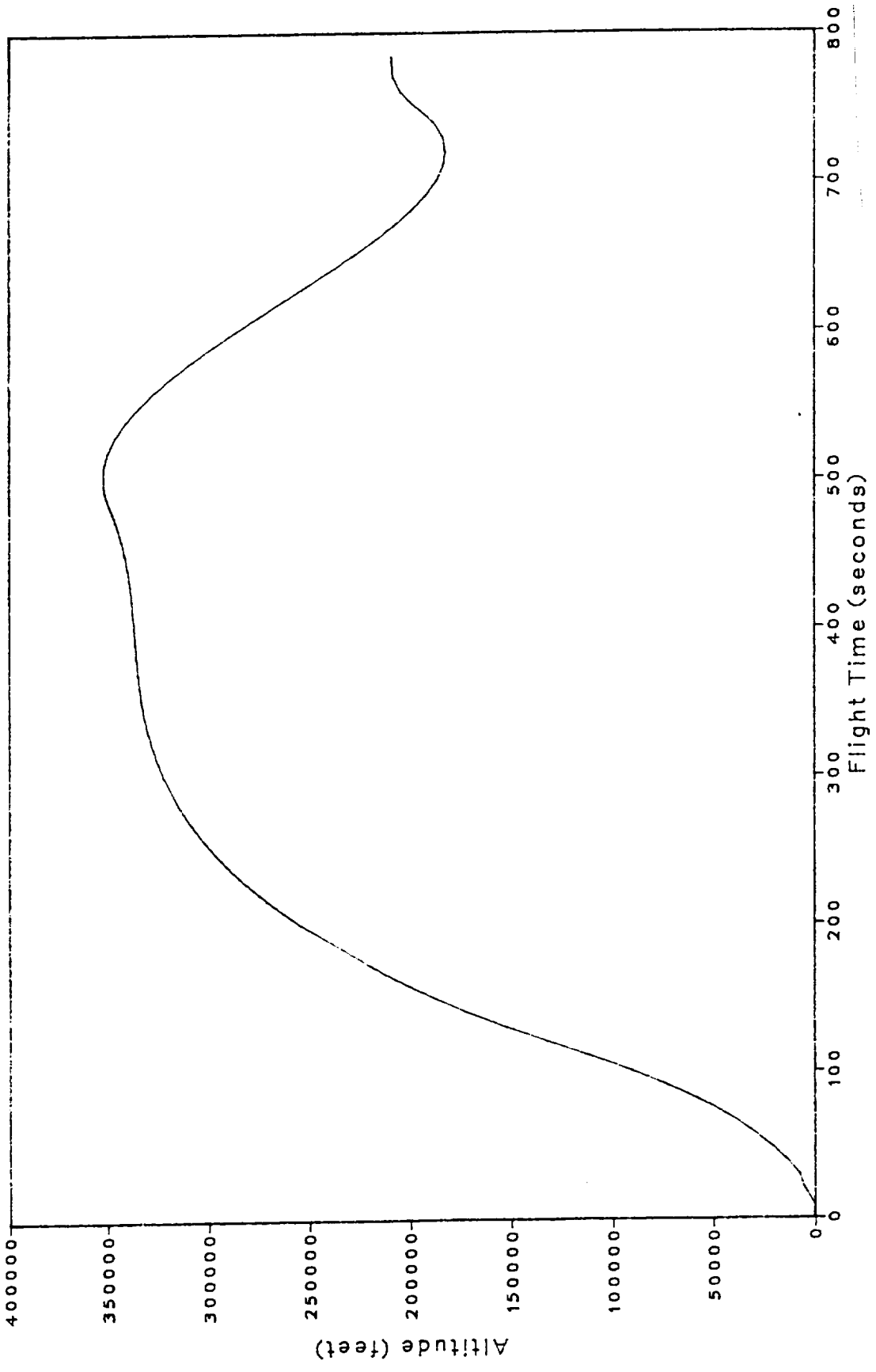


Figure 2: RTLS Trajectory: Altitude vs. Time

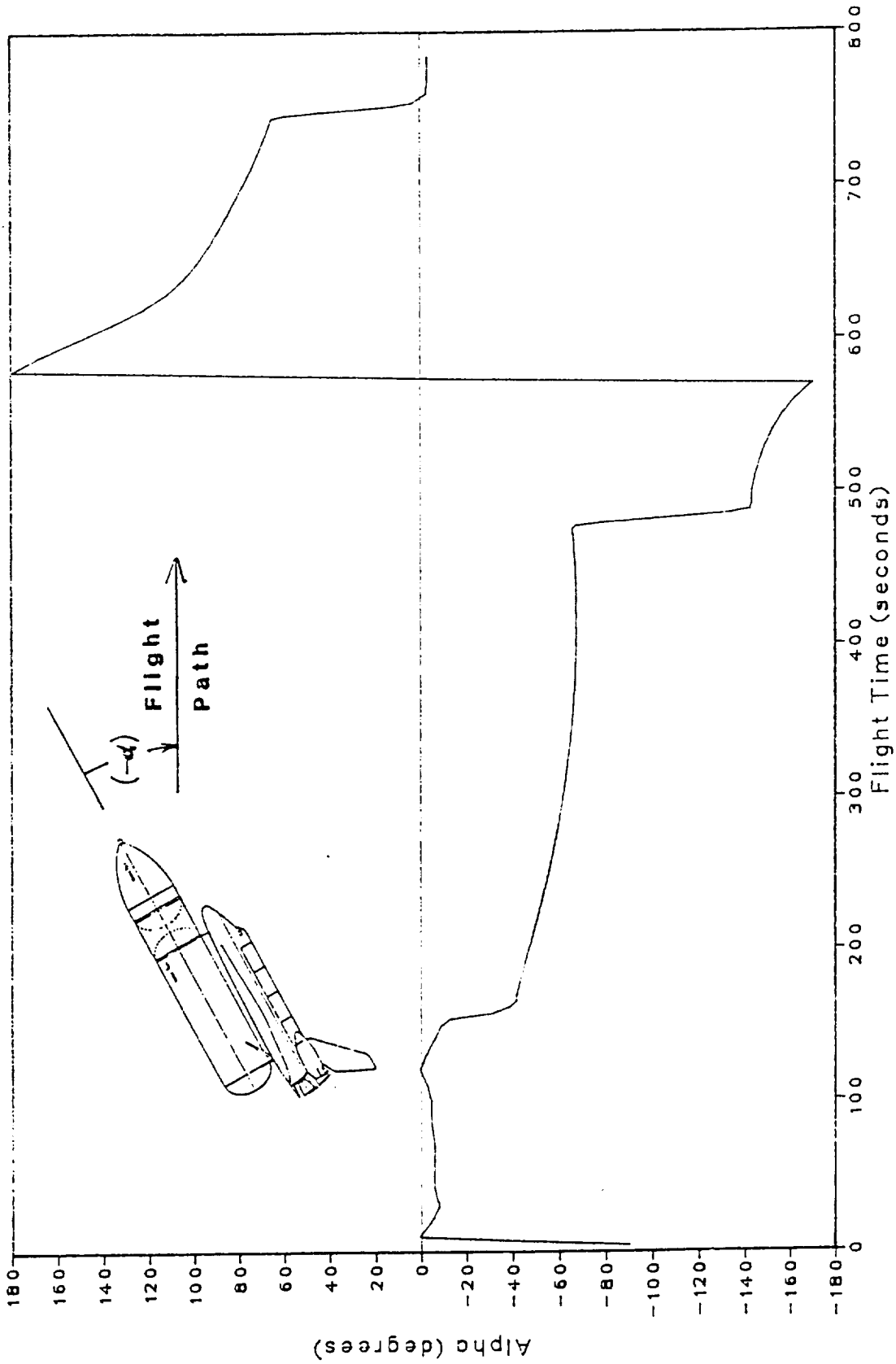
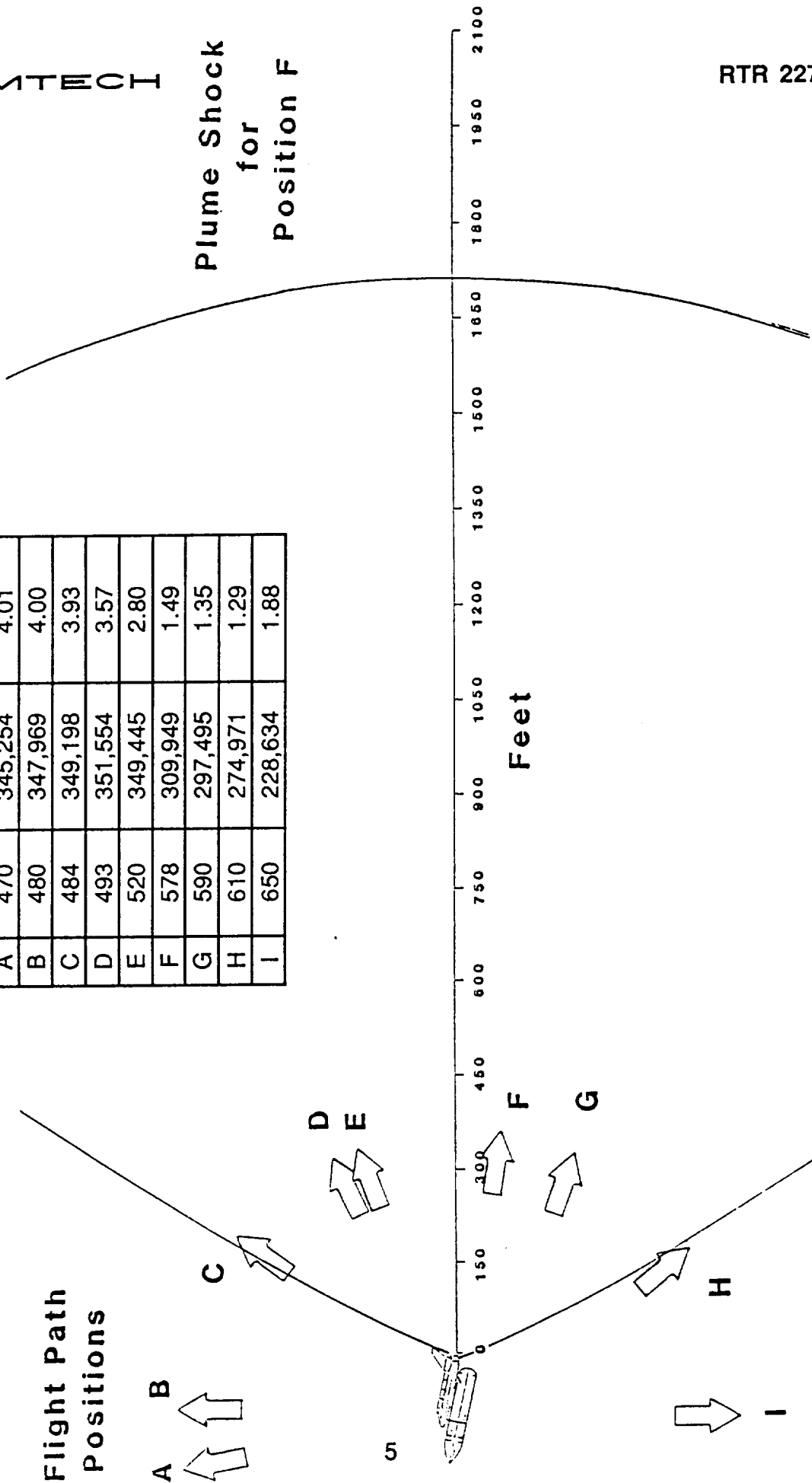


Figure 3: RTLS Trajectory: Angle-of-Attack vs. Time

Time	Altitude	$M_\infty$
A	345,254	4.01
B	347,969	4.00
C	349,198	3.93
D	351,554	3.57
E	349,445	2.80
F	309,949	1.49
G	297,495	1.35
H	274,971	1.29
I	228,634	1.88



Flight Path Positions

Figure 4: RTLS Flight Path Positions

## Section 2

# MODELING FOR ABORT CASES

### 2.1 Trajectories

The trajectory used to study the intact-abort return-to-launch-site maneuver was provided by Rockwell [1]. For the abort trajectories, the SSME engine #1 out and #3 out cases were analyzed. The trajectories were based on statistically acceptable limits which would result in conditions to maximize plume heating. Only dispersed trajectories were considered in the plume heating calculations. For the above abort cases,  $1\sigma$  dispersed trajectories were used for an SSME #1 out case and an SSME #3 out case.

Table 1 provides the data for the plume trajectory with SSME #1 engine out (with pitot pressure). The power-pitch-around (PPA) portion of the trajectory is marked in this table. The trajectory is plotted in Fig. 2. The details of the PPA portion of this trajectory are given in Figs. 5 through 7, where altitude, angle-of-attack and Mach number history profiles are provided.

### 2.2 CFD Modeling

The following paragraphs describe the CFD study that was conducted to define the return-to-launch-site plume-induced thermal environment for the Space Shuttle. The task addressed herein is the CFD approach to model the plume flowfield during the PPA maneuver. The motivation of the CFD study was to determine the flowfield in sufficient detail to perform convective and radiative heating calculations.

First, it was necessary to develop a CFD procedure by validating the results against measured data. The following assumptions were made to simplify the complexities of the flowfield:

1. No yaw was considered.
2. The flowfields consisted of two frozen species mixing via convection only — one frozen specie refers to the exhaust species and the other refers to air.
3. Diffusion and chemical reactions were neglected.

The algorithm used for the Navier-Stokes solver consists of the following features:

1. Upgrade PARC2D to include the species continuity equation for two species with no diffusion and chemical reaction.
2. Lag the species continuity equation behind the N-S equations.
3. Couple the species boundary conditions implicitly to species continuity equation.
4. Transfer information from the species continuity equation to the flow solver via mixture gamma and transport properties.
5. Use the original PARC2D solution as a restart to two-species computation.

Table 1: Generic RTLS Plume Trajectory with SSME #1 Out (With Pitot Pressure)

TIME SEC	ALTITUDE		VELOCITY		ANGLE--OF ATTACK		YAW		DENSITY SLUG/FT*3	TEMPERATURE (STATIC) DEG	PRESSURE (STATIC) PSIF	PRESSURE (PITOT) PSIF
	FT	FT/SEC	DEG	DEG	DEG	DEG						
0.23	-23.7	27.4	-90.15	88.68	0.2367E-02	519.8	0.2112E+04	0.00				
0.72	-22.2	28.2	6.08	75.88	0.2367E-02	519.8	0.2112E+04	0.00				
2.00	-1.1	37.9	4.97	46.53	0.2366E-02	519.7	0.2110E+04	0.00				
4.00	80.9	63.0	4.44	26.32	0.2359E-02	519.3	0.2104E+04	0.00				
6.00	225.7	93.5	3.75	17.81	0.2348E-02	519.3	0.2093E+04	0.00				
8.00	438.4	127.7	3.14	13.39	0.2332E-02	518.8	0.2077E+04	0.00				
10.00	723.4	164.1	2.46	9.85	0.2311E-02	518.3	0.2058E+04	0.00				
12.00	1084.0	203.3	1.03	5.70	0.2284E-02	517.5	0.2029E+04	0.00				
14.00	1521.9	245.6	0.24	0.93	0.2252E-02	516.7	0.1997E+04	0.00				
16.00	2035.4	290.7	-0.41	-3.09	0.2215E-02	515.6	0.1960E+04	0.00				
18.00	2624.1	338.6	-4.19	-3.53	0.2173E-02	514.4	0.1919E+04	0.00				
20.00	3291.9	388.1	-6.92	-2.07	0.2127E-02	513.0	0.1873E+04	0.00				
22.00	4042.9	437.2	-7.19	-1.32	0.2076E-02	511.4	0.1822E+04	0.00				
24.00	4877.9	485.7	-7.17	-1.01	0.2021E-02	509.5	0.1767E+04	0.00				
26.00	5793.2	532.2	-7.33	-0.77	0.1962E-02	507.4	0.1709E+04	0.00				
28.00	6784.9	576.8	-7.95	-0.69	0.1900E-02	505.1	0.1647E+04	0.00				
30.00	7850.9	620.0	-8.32	-0.69	0.1836E-02	502.4	0.1583E+04	0.00				
32.00	8989.8	662.1	-8.31	-0.68	0.1770E-02	499.5	0.1517E+04	0.00				
34.00	10200.0	703.7	-8.36	-0.60	0.1702E-02	496.2	0.1450E+04	0.00				
36.00	11480.3	745.1	-7.60	-0.46	0.1634E-02	492.3	0.1381E+04	0.00				
38.00	12828.1	786.3	-6.66	-0.37	0.1566E-02	488.2	0.1312E+04	0.00				
40.00	14240.4	827.3	-6.05	-0.31	0.1497E-02	483.6	0.1243E+04	0.00				
42.00	15714.5	868.3	-5.78	-0.22	0.1428E-02	478.8	0.1174E+04	0.00				
44.00	17248.8	908.7	-5.33	-0.16	0.1359E-02	473.5	0.1105E+04	0.00				
46.00	18841.4	949.3	-4.83	-0.17	0.1292E-02	467.9	0.1037E+04	0.00				
48.00	20490.6	990.7	-5.01	-0.17	0.1224E-02	462.0	0.9707E+03	0.00				
50.00	22195.9	1032.1	-5.33	-0.14	0.1158E-02	455.7	0.9057E+03	0.00				
52.00	23956.5	1073.0	-5.33	-0.11	0.1093E-02	449.0	0.8421E+03	0.00				
54.00	25770.1	1114.0	-5.40	-0.05	0.1029E-02	442.0	0.7807E+03	0.00				
56.00	27637.6	1156.8	-5.82	-0.10	0.9662E-03	434.6	0.7207E+03	0.00				
58.00	29562.9	1201.6	-6.23	-0.15	0.9050E-03	427.0	0.6633E+03	0.00				
60.00	31550.6	1247.9	-6.15	-0.12	0.8442E-03	419.2	0.6074E+03	0.00				
62.00	33604.6	1296.6	-6.06	-0.11	0.7841E-03	411.6	0.5539E+03	0.00				
64.00	35728.9	1347.8	-5.88	-0.14	0.7249E-03	404.0	0.5028E+03	0.00				
66.00	37927.6	1399.9	-5.66	-0.21	0.6648E-03	397.7	0.4538E+03	0.00				
68.00	40204.5	1454.4	-5.75	-0.20	0.6059E-03	391.9	0.4075E+03	0.00				
70.00	42564.9	1511.3	-5.95	-0.18	0.5483E-03	386.9	0.3641E+03	0.00				
72.00	45014.4	1574.7	-6.41	-0.23	0.4934E-03	381.8	0.3232E+03	0.00				
74.00	47559.3	1644.7	-6.26	-0.28	0.4416E-03	376.2	0.2852E+03	0.00				
76.00	50203.7	1720.1	-5.71	-0.31	0.3927E-03	370.9	0.2500E+03	0.00				
78.00	52949.3	1800.4	-5.27	-0.34	0.3459E-03	366.5	0.2176E+03	0.00				
80.00	55797.6	1886.4	-4.90	-0.35	0.3010E-03	364.2	0.1882E+03	0.00				
82.00	58747.7	1974.8	-4.48	-0.39	0.2588E-03	364.4	0.1619E+03	0.00				
84.00	61796.3	2066.7	-4.10	-0.40	0.2193E-03	368.4	0.1387E+03	0.00				
86.00	64940.1	2159.3	-3.55	-0.51	0.1847E-03	373.7	0.1185E+03	0.00				
88.00	68174.1	2249.2	-2.76	-0.49	0.1552E-03	379.1	0.1010E+03	0.00				
90.00	71491.9	2339.5	-2.00	-0.49	0.1303E-03	384.0	0.8591E+02	0.00				

Table 1: (continued) Generic RTLS Plume Trajectory with SSME #1 Out (With Pitot Pressure)

TIME SEC	ALTITUDE FT	VELOCITY FT/SEC	ANGLE--OF ATTACK		DENSITY SLUG/FT**3	TEMPERATURE (STATIC) DEG	PRESSURE (STATIC) PSIF	PRESSURE (PITOT) PSIF
			DEG	YAW DEG				
92.00	74886.3	2427.6	-1.42	-0.55	0.1096E-03	387.6	0.7295E+02	0.00
94.00	78353.9	2517.3	-1.52	-0.62	0.9209E-04	391.1	0.6182E+02	0.00
96.00	81893.3	2610.0	-1.75	-0.66	0.7727E-04	394.2	0.5229E+02	0.00
98.00	85501.7	2702.6	-1.92	-0.72	0.6470E-04	397.6	0.4416E+02	0.00
100.00	89176.3	2793.3	-2.00	-0.77	0.5404E-04	401.2	0.3723E+02	0.00
102.00	92914.6	2872.1	-1.85	-0.84	0.4508E-04	405.1	0.3134E+02	0.00
104.00	96712.9	2957.9	-1.84	-0.87	0.3754E-04	409.2	0.2637E+02	0.00
106.00	100567.6	3040.4	-1.80	-0.92	0.3113E-04	415.4	0.2218E+02	0.00
108.00	104473.7	3126.8	-1.86	-0.96	0.2572E-04	423.0	0.1865E+02	0.00
110.00	108427.5	3217.5	-2.05	-0.70	0.2139E-04	428.6	0.1571E+02	0.00
112.00	112425.0	3301.6	-2.22	-0.45	0.1778E-04	434.1	0.1323E+02	0.00
114.00	116453.2	3369.4	-2.20	-0.29	0.1479E-04	440.1	0.1116E+02	0.00
116.00	120483.1	3417.4	-2.10	-0.13	0.1232E-04	446.6	0.9433E+01	0.00
118.00	124485.1	3445.8	-1.95	-0.02	0.1028E-04	453.5	0.7996E+01	0.00
120.00	128440.7	3462.0	-1.96	-0.05	0.8648E-05	459.9	0.6817E+01	0.00
122.00	132338.5	3472.5	-2.56	-0.19	0.7301E-05	466.1	0.5833E+01	0.00
124.00	136170.8	3471.1	-3.42	-0.36	0.6199E-05	472.1	0.5016E+01	0.00
126.00	139932.7	3460.7	-4.21	-0.46	0.5299E-05	477.0	0.4333E+01	0.00
128.00	143621.5	3454.3	-4.99	-0.52	0.4555E-05	481.3	0.3758E+01	0.00
130.00	147235.8	3451.3	-5.87	-0.65	0.3960E-05	482.0	0.3272E+01	0.00
131.36	149650.8	3446.9	-6.44	-0.71	0.3611E-05	482.0	0.2983E+01	0.00
137.76	160595.8	3441.1	-8.48	-0.81	0.2386E-05	479.2	0.1960E+01	0.00
138.24	161389.5	3442.2	-8.28	-0.78	0.2315E-05	479.0	0.1901E+01	0.00
150.00	179594.2	3455.0	-3.98	-0.48	0.1162E-05	471.2	0.9389E+00	0.00
153.60	184675.2	3468.1	-12.92	-0.45	0.9579E-06	468.7	0.7697E+00	10.51
156.00	187945.9	3476.6	-25.32	-0.44	0.8457E-06	466.8	0.6768E+00	9.71
168.96	204389.4	3537.5	-39.25	-0.64	0.4536E-06	451.6	0.3512E+00	5.38
184.32	221420.7	3586.3	-42.76	-0.56	0.2424E-06	410.3	0.1705E+00	2.94
186.00	223126.6	3592.7	-43.13	-0.55	0.2276E-06	405.2	0.1581E+00	2.77
199.68	235906.6	3637.6	-45.96	-0.33	0.1254E-06	391.6	0.8405E-01	1.56
215.04	247982.0	3693.5	-48.84	-0.04	0.6842E-07	378.0	0.4417E-01	0.87
230.40	257784.1	3771.5	-51.51	-0.04	0.4184E-07	367.0	0.2621E-01	0.56
240.00	262819.2	3825.2	-53.04	-0.05	0.3250E-07	361.4	0.2004E-01	0.44
245.76	265455.6	3859.1	-53.92	-0.05	0.2848E-07	358.4	0.1742E-01	0.40
261.12	271144.6	3955.0	-56.09	-0.05	0.2141E-07	352.0	0.1286E-01	0.31
276.48	275005.0	4057.8	-58.03	-0.05	0.1764E-07	347.7	0.1047E-01	0.27
279.71	275598.8	4080.2	-58.40	-0.05	0.1712E-07	347.0	0.1015E-01	0.25
291.84	277173.9	4165.1	-59.83	-0.05	0.1582E-07	345.3	0.9329E-02	0.26
307.20	277764.8	4276.9	-61.40	-0.05	0.1536E-07	344.6	0.9040E-02	0.26
322.56	276942.5	4392.7	-62.76	-0.05	0.1600E-07	345.5	0.9445E-02	0.29
337.92	274881.1	4511.5	-63.91	-0.05	0.1775E-07	347.8	0.1054E-01	0.34
353.28	271763.5	4632.9	-64.87	-0.05	0.2075E-07	351.3	0.1244E-01	0.41
355.20	271309.0	4648.2	-64.98	-0.05	0.2123E-07	351.8	0.1275E-01	0.43
362.88	269382.0	4649.6	-94.72	0.37	0.2338E-07	354.0	0.1413E-01	0.47
364.80	268875.0	4638.1	-95.31	0.42	0.2399E-07	354.6	0.1452E-01	0.48
368.64	267820.7	4615.3	-95.48	0.36	0.2529E-07	355.8	0.1535E-01	0.50
384.00	263085.0	4514.3	-98.72	-0.25	0.3207E-07	361.1	0.1976E-01	0.61

Table 1: (concluded) Generic RTLS Plume Trajectory with SSME #1 Out (With Pitot Pressure)

TIME	ALTITUDE	VELOCITY	ANGLE--OF		DENSITY	TEMPERATURE	PRESSURE	PRESSURE
SEC	FT.	FT/SEC	ATTACK	YAW	SLUG/FT**3	(STATIC)	(STATIC)	(PITOT)
			DEG	DEG		DEG	PSIF	PSIF
399.36	257597.4	4400.4	-99.65	-0.34	0.4224E-07	367.2	0.2647E-01	0.76
414.72	251508.9	4279.9	-101.54	-1.02	0.5733E-07	374.1	0.3661E-01	0.98
430.08	244952.6	4138.6	-104.54	-0.89	0.7965E-07	381.4	0.5191E-01	1.27
445.44	238020.9	3983.0	-107.11	-1.08	0.1128E-06	389.2	0.7510E-01	1.68
460.80	230817.4	3806.0	-109.57	-1.35	0.1619E-06	397.3	0.1102E+00	2.20
476.16	223448.2	3596.5	-112.02	-1.53	0.2245E-06	404.9	0.1558E+00	2.74
491.52	216020.6	3359.8	-114.49	-1.72	0.2947E-06	427.8	0.2161E+00	3.16
506.88	208642.1	3098.6	-116.99	-1.96	0.3892E-06	442.0	0.2949E+00	3.57
522.24	201421.0	2809.6	-119.56	-2.27	0.5065E-06	456.1	0.3960E+00	3.86
537.60	194467.5	2480.9	-122.31	-2.58	0.6596E-06	462.4	0.5229E+00	3.98
552.96	187894.5	2114.0	-125.35	-2.89	0.8473E-06	466.9	0.6782E+00	3.81
568.32	181817.8	1744.3	-128.62	-3.59	0.1068E-05	470.2	0.8608E+00	3.42
583.68	176358.4	1351.0	-132.49	-4.48	0.1314E-05	472.7	0.1065E+01	2.78
599.04	171645.3	922.5	-138.06	-6.57	0.1573E-05	474.5	0.1279E+01	2.08
614.40	167819.2	457.3	-151.53	-13.45	0.1817E-05	476.3	0.1484E+01	1.68
629.76	165010.3	226.8	-155.32	-15.44	0.1845E-05	476.5	0.1507E+01	1.66
645.12	163364.2	719.1	102.74	-27.99	0.2020E-05	477.7	0.1654E+01	1.71
660.48	163102.6	1336.9	58.88	-8.47	0.2149E-05	478.4	0.1762E+01	2.38
675.84	164477.2	2021.0	50.05	-4.47	0.2170E-05	478.5	0.1780E+01	4.53
691.20	167768.0	2773.9	44.83	-2.84	0.2061E-05	477.9	0.1688E+01	8.56
706.56	173294.3	3607.6	40.52	-1.93	0.1821E-05	476.3	0.1487E+01	13.58
721.92	181486.2	4539.6	36.82	-1.20	0.1477E-05	473.9	0.1200E+01	18.22
735.78	191635.4	5432.2	33.56	-0.64	0.1082E-05	470.4	0.8720E+00	20.88
750.90	191736.3	5439.7	30.64	-0.21	0.7348E-06	464.5	0.5851E+00	20.19
737.28	192908.5	5518.8	30.61	-0.21	0.7320E-06	464.4	0.5828E+00	20.16
739.18	194537.5	5615.5	27.85	-0.20	0.7000E-06	463.6	0.5563E+00	19.84
752.64	203717.0	6287.0	17.95	-0.23	0.6578E-06	462.4	0.5215E+00	16.60
755.56	204919.9	6444.6	-3.41	-0.32	0.4648E-06	453.1	0.3610E+00	17.13
763.56	206767.8	6483.2	-3.48	-0.31	0.4450E-06	450.4	0.3436E+00	17.13
768.00	206942.4	6480.3	-3.94	-0.31	0.4164E-06	446.3	0.3185E+00	17.13
768.56	206921.4	6480.2	-3.97	-0.32	0.4138E-06	445.9	0.3162E+00	17.13
768.56	206921.4	6480.2	-3.97	-0.32	0.4141E-06	445.9	0.3165E+00	17.13

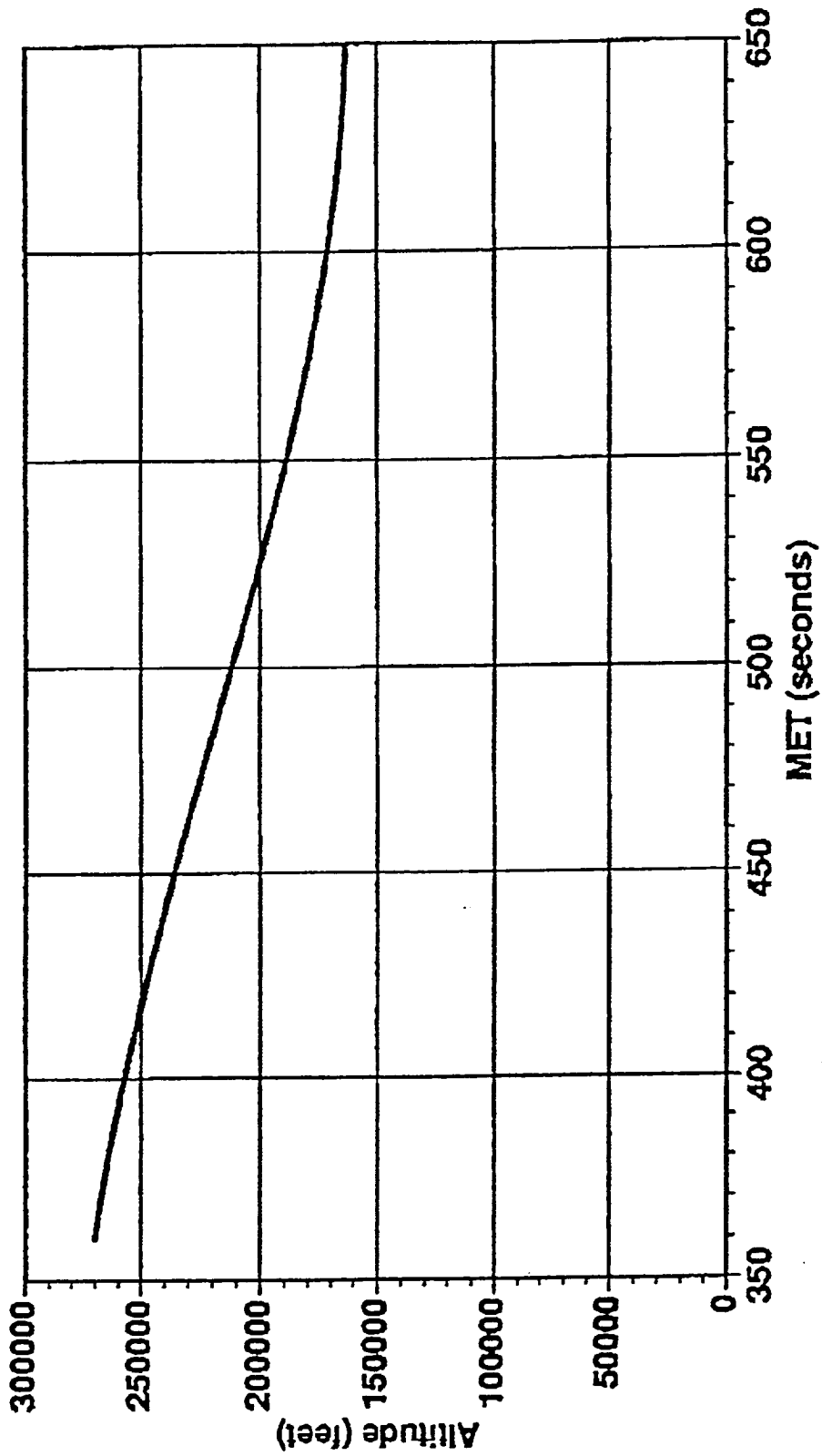


Figure 5: SSME #1 Out Generic RTLS/PPA Trajectory Altitude Profile



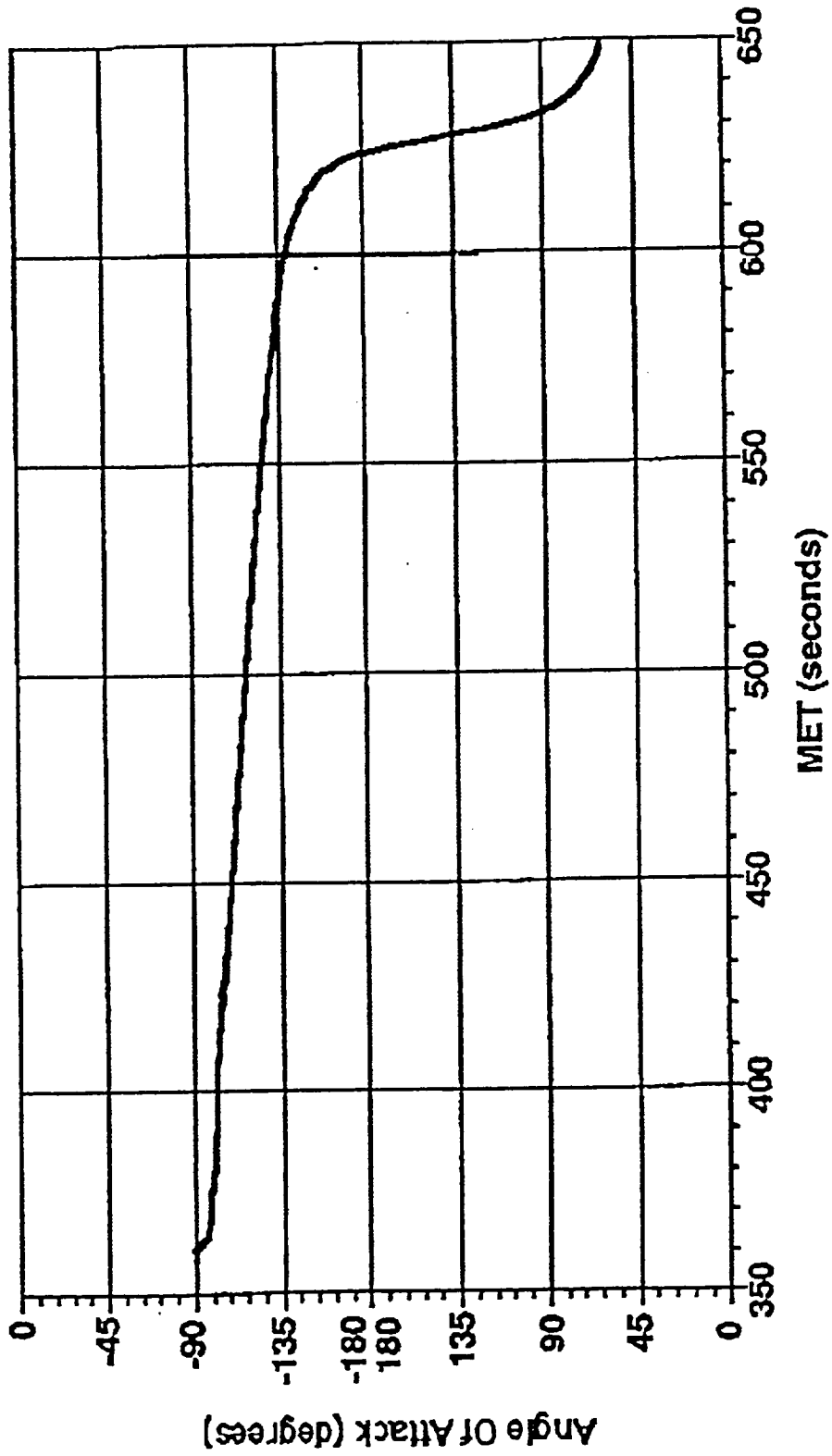


Figure 6: SSME #1 Out Generic RTLS/PPA Trajectory Angle-of-Attack Profile

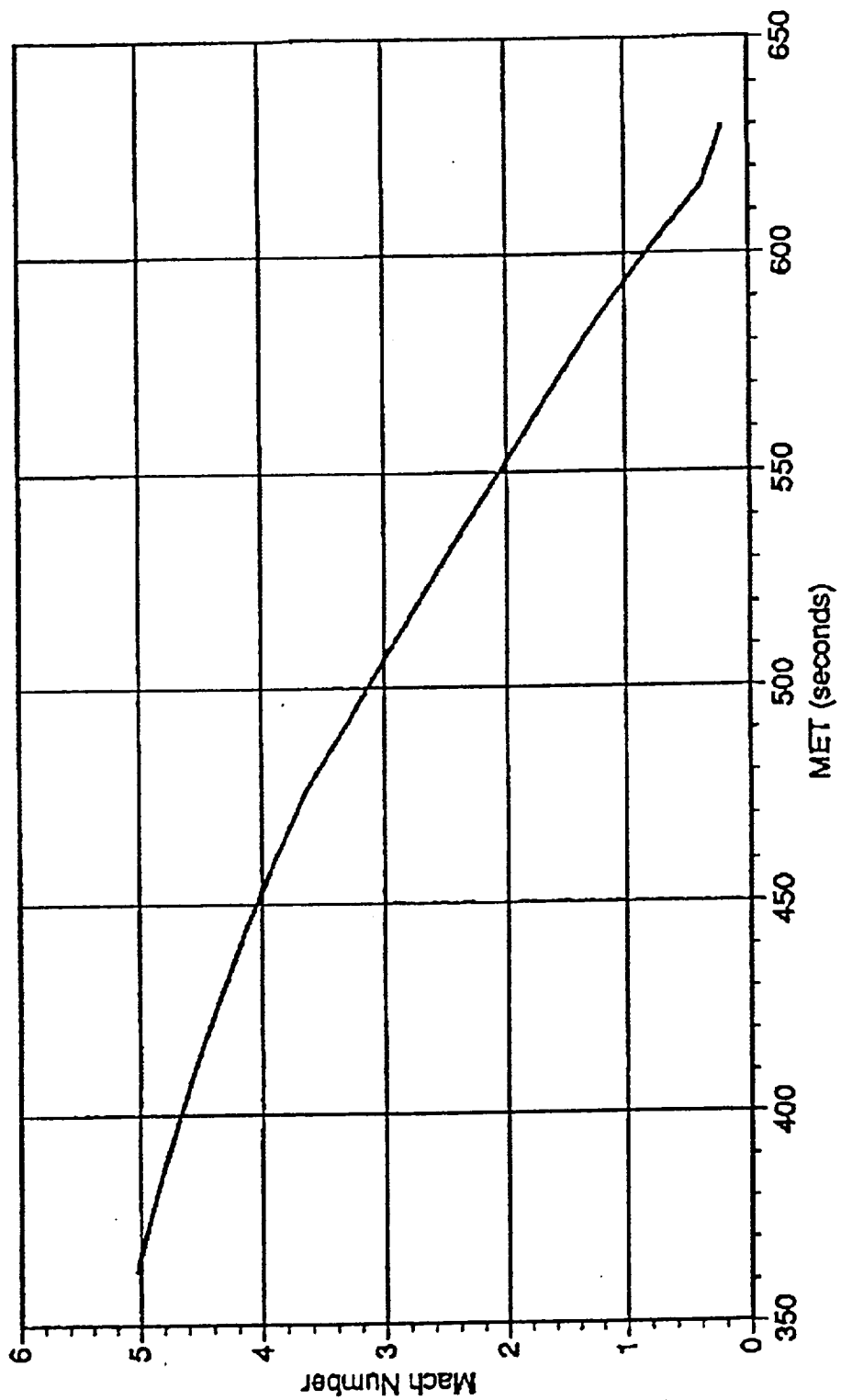


Figure 7: SSME #1 Out Generic RTLS/PPA Trajectory Mach Number Profile

The second step to the CFD modeling was to use a composite plume for two SSME plumes. Then the CFD methodology developed in the first step was used for an axisymmetric flowfield corresponding to location F in Fig. 4. This is the trajectory point where the angle-of-attack is 180 deg. In order to cover the whole range of angle-of-attack in the PPA maneuver, trajectory locations varying from C through H (Fig. 4) must be covered. At CFD points C and H, for example, a possibility of shear layer impingement on the vehicle surface exists. Of these two locations, location C seems to be more critical where the angle-of-attack is on the order of  $-135$  deg, and there is a possibility of shear layer impingement on the tank base.

Only the first two steps of the problem were covered during this investigation. The two technical notes resulting from the first two steps of this work are documented in appendices A and B.

### 2.3 Engineering Modeling (Heating Indicator Approach)

While conducting the CFD study, an easier method has to be sought to estimate the upper level of heating on the ET during the power pitch-around maneuver of the RTLS. If a conservative method of prediction can be found which produces results not impacting the ET TPS design, then flight assessments and design environments can be produced in a simple manner for this extremely complex flow process. An early attempt was made by Rader [2] in the early 1970's at Northrop. This method has also been utilized by Rockwell in a modified way. Both of these methods disregard most of the free-stream/plume interaction effects. The plume gas is assumed to be reversed and impinge at free-stream conditions on the ET components producing the worst case heating. These heating rates are computed on a stagnation point.

Review of the method developed by Rader and used in part by Rockwell reveals interesting results. The correlation due to Rader is essentially a different version of a Fay-Riddell equation,

$$\dot{q} = k \sqrt{\frac{2^n p_s}{R_{eff}}}$$

where  $p_s$  = Stagnation pressure  
 $R_{eff}$  = Effective radius  
 $n$  = 0, 2D  
 = 1, axisymmetric  
 $k$  = Stagnation heating rate plume parameter

Figure 8 shows the variation of  $k$  with  $p_s$  for various  $R_{eff}$ . For smaller values of  $R$ , i.e., at  $R_{eff} = 0.406$  in., the  $k$  values are near the frozen flow limit. As  $R$  is increased, the  $k$  values move toward the equilibrium values. These computations were all made by Rader [2]. A cross plot of the ratio of  $k$  and  $k_{eq}$  vs. radius was made in Fig. 8 for two external values of stagnation pressure. Since no data are available beyond

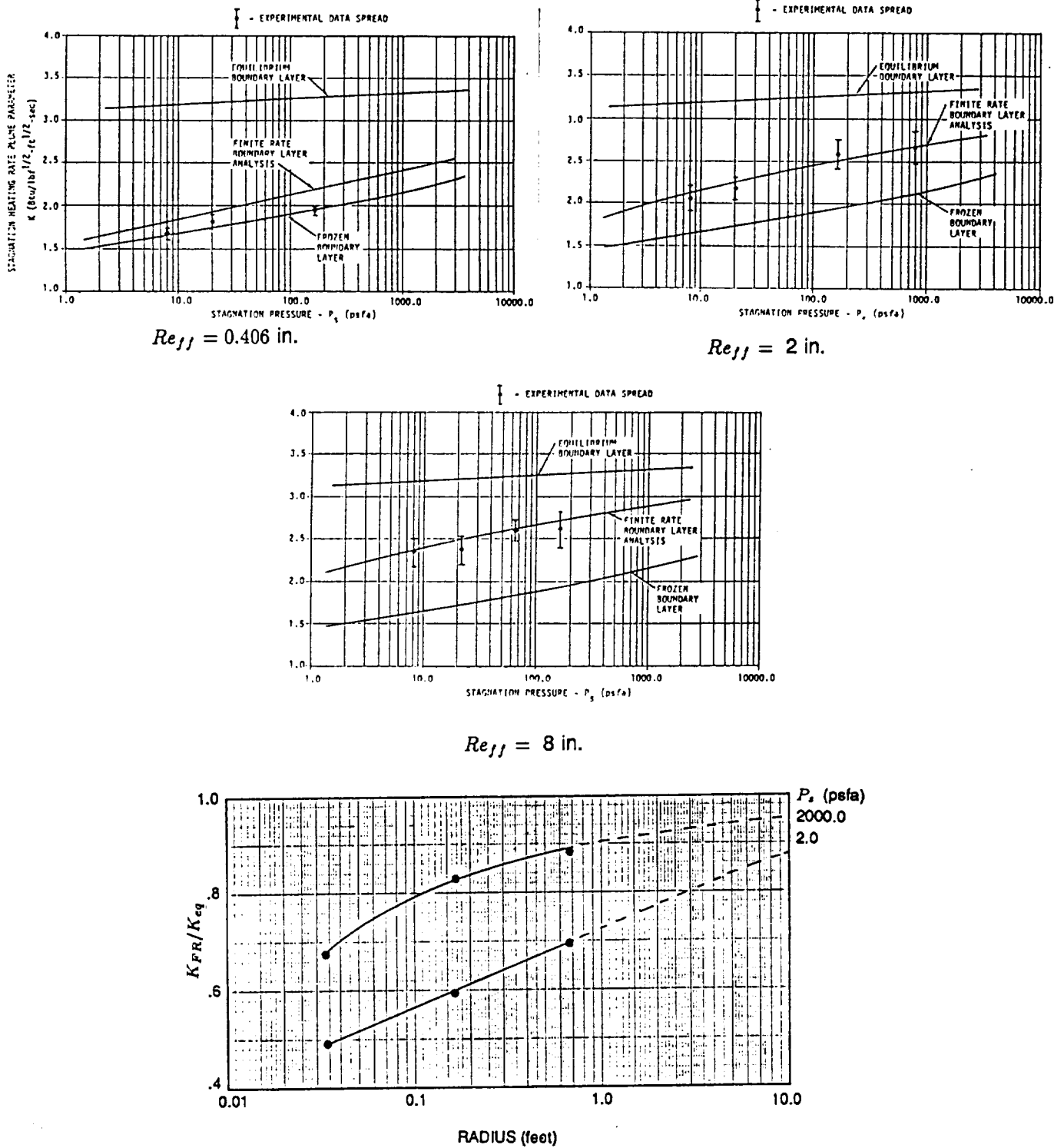


Figure 8: Correlation of Stagnation Heating Rate Plume Parameter with Radius

$R_{eff} = 8$  in., an extrapolation of the plotted data was performed up to  $R = 10.0$  ft. The ratio extrapolates to a value of 0.8 or higher, indicating that the equilibrium value is being reached for large radii.

In order to generate a new heating indicator procedure, a conservative philosophy was applied at REMTECH. The following assumptions were made in running a heating indicator to an RTLS trajectory.

1. The flow considered chemistry effects.

Whether the flow chemistry is in equilibrium or the flow has finite reaction rates was considered by the code by turning on the appropriate flag in the input. In order to check the chemistry of the flow, the equilibrium option must be turned on and the results compared against the finite rate results. The code used for doing these computations was BLIMPK [3].

2. The total enthalpy of the gas,  $H_t$ , was assumed to be equal to total enthalpy of the plume gas.

In other words, no mixture of plume gas and air exists, thus giving the most conservative value for  $H_t$ .

3. The total pressure of the gas,  $p_t$ , was assumed to be post-shock total pressure based on free-stream air.

No angle-of-attack effects were considered in the heating indicator calculations.

### Section 3

## GENERATION OF ABORT ENVIRONMENTS

The total scope of this section should cover the environments of various body points located on the ET. However, complete environments over the various body points are not available now for reasons that will become clear later. The objective of generating these environments is to check any exceedances over design.

Work was initiated to compute the abort environments on the nose of the ET aft dome. This point may be the hottest of all other body points located in the rear of the ET. The radius of the ET dome (=10 ft) was used to compute a heating indicator with the assumptions made in Section 2.3. Two design trajectories, one for aeroheating and the other for plume heating, were examined to compute the above heating. The altitude-velocity profiles near the PPA maneuver are given in Fig. 9. The heating rate history for the aeroheating trajectory is given in Fig. 10. During the PPA period, the highest heating occurs around 530 sec with a heating rate of 2 BTU/ft<sup>2</sup>-sec. A similar set of calculations was made for the plume heating trajectory. Figure 11 shows the heating rate history. Assuming equilibrium edge properties, both equilibrium and finite rate computations were made using BLIMPK. The differences between these two computations are minimal. Both of these computations used 100 percent plume gas. When compared against RI data book environments, the disparities are obvious. The RI peak heating is 0.9, as opposed to a value of 2.5 from the heating indicator. For comparison, the air-only computations are also given in this figure. A number of discussions, teleconferences and presentations have been held among REMTECH/MSFC, Lockheed/JSC and RI to resolve these differences. Although a lot of understanding of the methods from different organizations has developed, a definite consensus has yet to be reached as to the validity of the RI approach. Figure 11 shows results from Lockheed/JSC which are essentially the same as these from REMTECH. Another consideration was applied to REMTECH's computations. Since the PPA maneuver occurs in a relatively rarer atmosphere, it is worthwhile to check if the heating is transitional. Accordingly, a bridging relationship due to Sherman was used in the following way:

Bridging Relationship: (Sherman)

$$N_{u_t} = \frac{N_{u_{FM}}}{1 + \frac{N_{u_{FM}}}{N_{u_c}}}$$

where  $N_{u_{FM}}$  = free molecular value (obtained from Schaaf and Chambré [4] and  $N_{u_c}$  = continuum value (computed from the BLIMPK code).

Then,

$$\dot{q}_t = \frac{N_{u_t} K \Delta T}{D} \equiv St_t \rho_\infty U_\infty \Delta H$$

At  $t = 537.6$  sec (plume trajectory),  $St_c = 0.0106$  and  $St_{FM} = 0.089$ .  $St_t = 0.00947$   
 $\Rightarrow \dot{q} = 2.35$  BTU/ft<sup>2</sup>-sec.

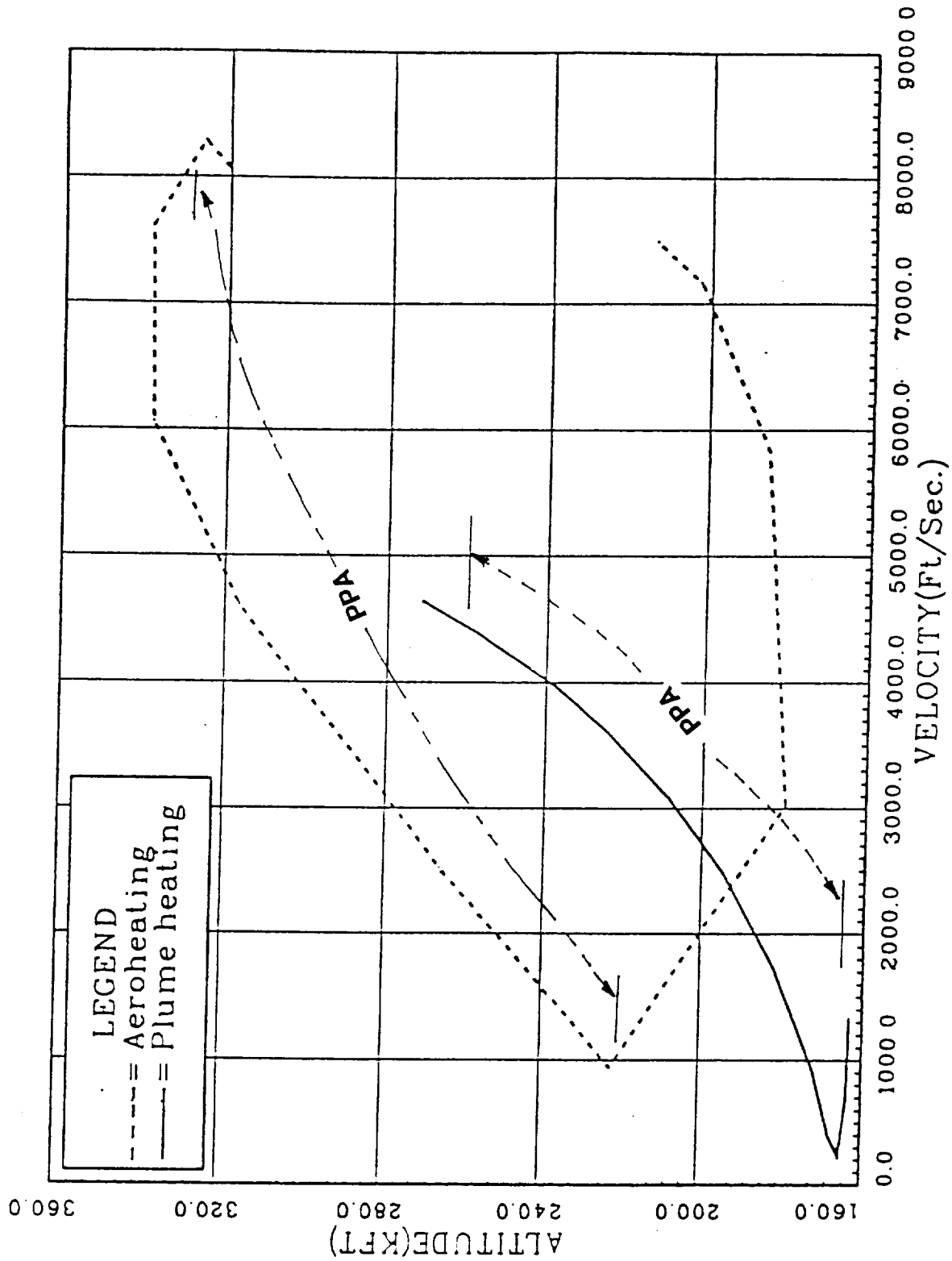


Figure 9: Altitude-Velocity Profiles for PPA Maneuver

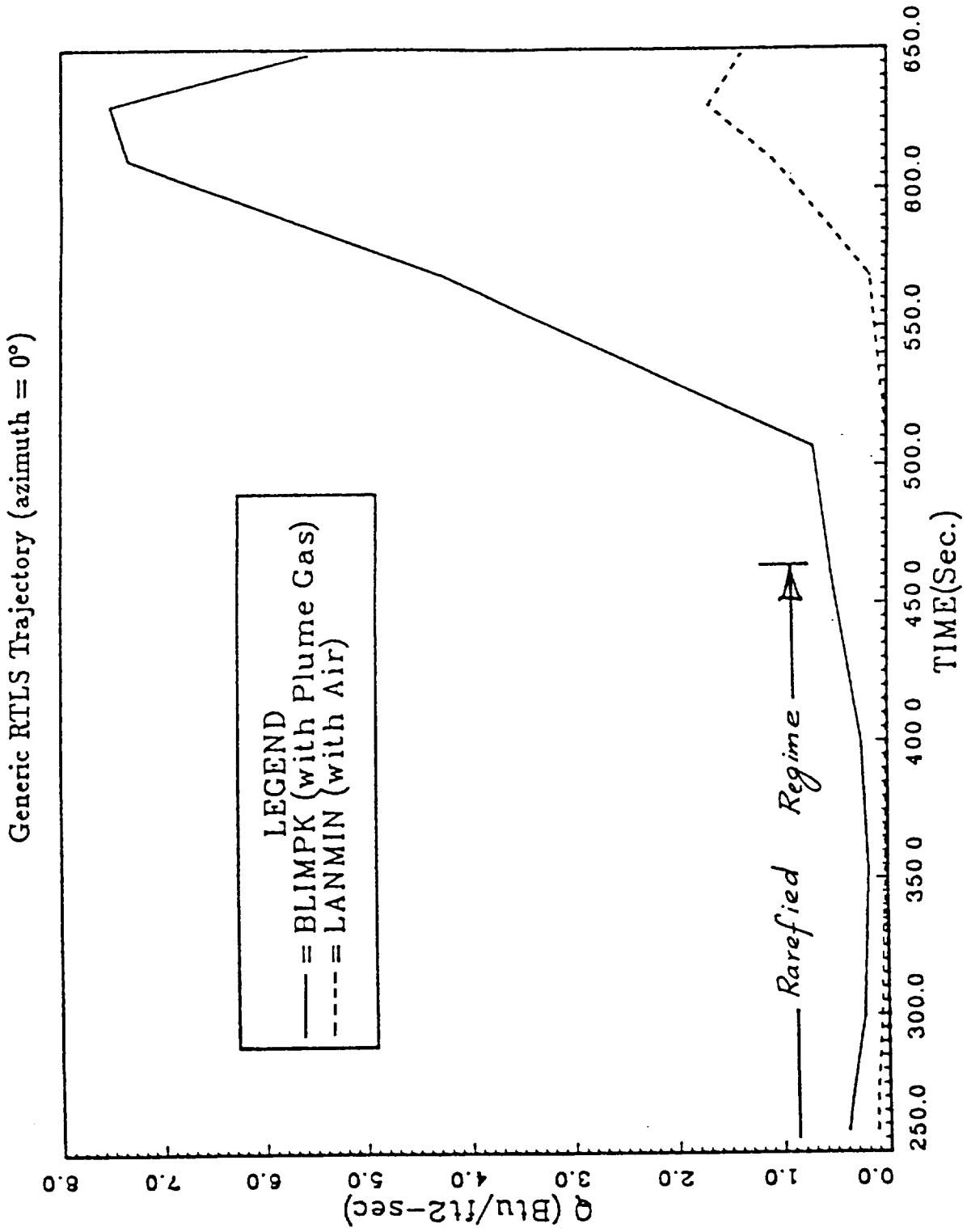
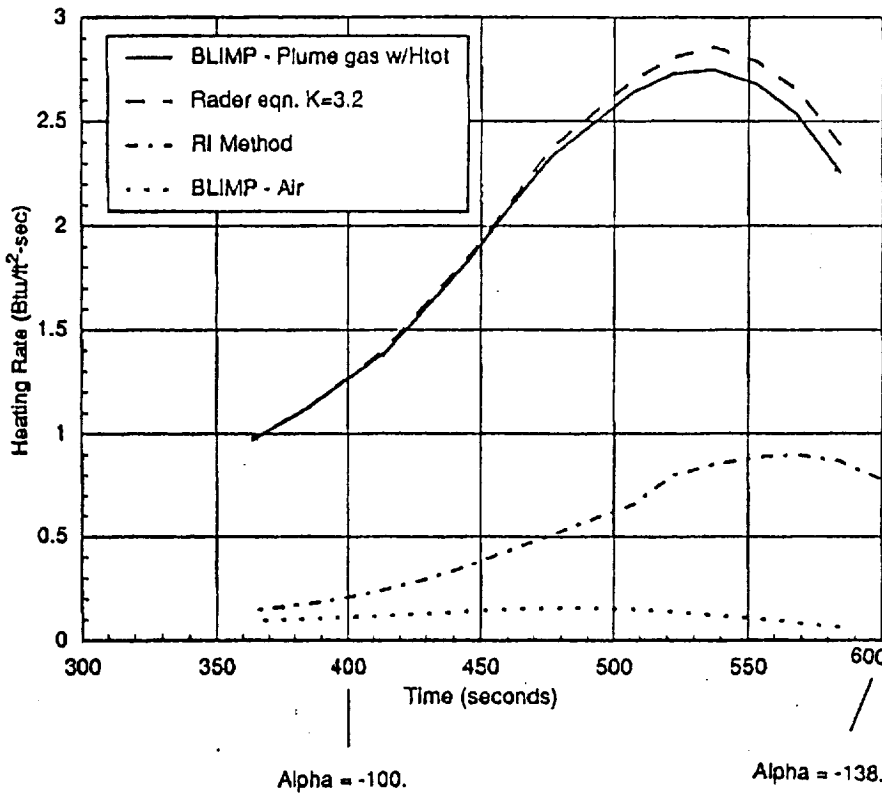
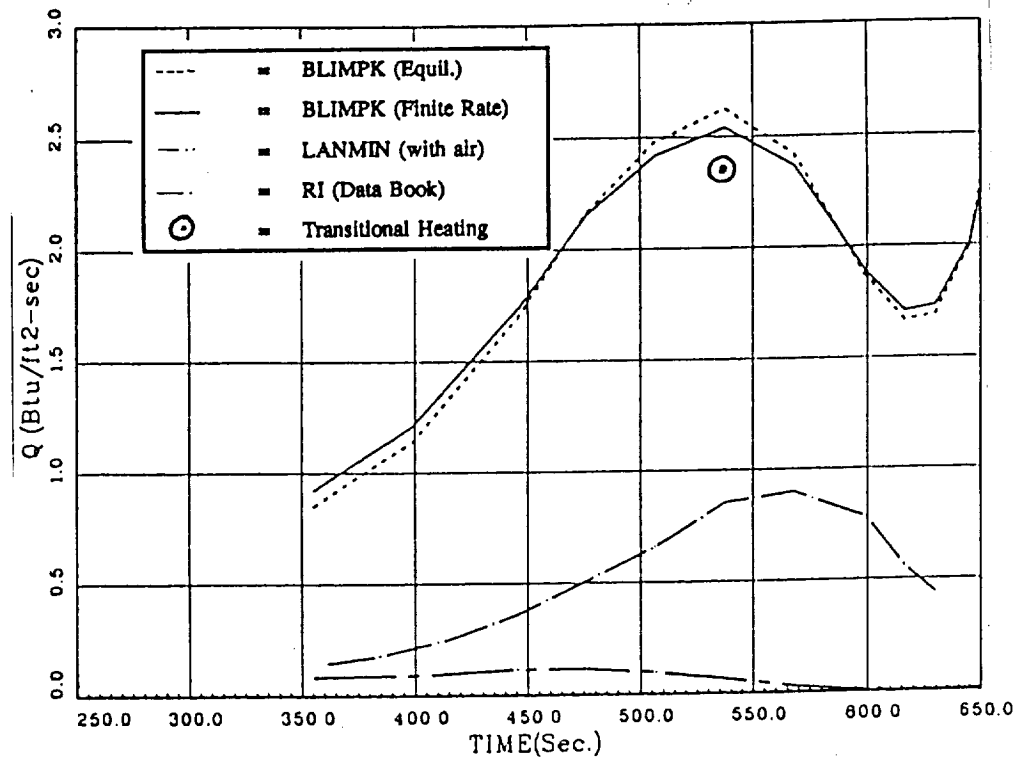


Figure 10: Heating Rate History for Aeroheating Trajectory



REMTECH's  
RESULTS



LOCKHEED's  
RESULTS

Figure 11: Heating Rate History for Plume Heating Trajectory

The data point was plotted in Fig. 11 showing that the transitional heating computation did not bring the level of peak heating to the RI level.

Since the CFD computations for both 180 deg and 135 deg angle-of-attack have not been completed, it was not possible to compute either the convective or the radiative environments. Although the 180 deg case has been reported in Appendix B, there seems to be some sensitivity to the grid. As a result, this flowfield could not be used for heating environments calculations.

## Section 4

# CONCLUSIONS AND RECOMMENDATIONS

### 4.1 Conclusions

The following conclusions have been made by the thermal panel after the numerous discussions and presentations:

1. The basis for RI/Downey's RTLS methodology is not clear.
2. A heating indicator approach alone will not be able to provide thermal environments for design purposes.
3. However, a heating indicator can provide relative environments from one trajectory to the next.
4. A suitable CFD study is required to define the flowfield for the complex interaction region during a PPA maneuver.
5. The completed CFD studies both by REMTECH and other companies are not accurate enough to define the required thermal environments over the ET.
6. Several conclusions were drawn from the CFD experience of Rockwell/Huntsville and REMTECH in application to this problem:
  - a. The total flowfield is so large that initial gridding is difficult for proper capturing of the shock structure.
  - b. Gridding for the total flowfield makes gridding for detailed flow around the Shuttle configuration difficult.
  - c. The subsonic flowfield is quite large, making the placement of the outflow plume boundary inaccurate if it is not placed far enough away from the mixing region.

### 4.2 Recommendations

Problems remain in validating the CFD flowfield for the Shuttle PPA maneuver. Since no wind tunnel or flight data are available, the CFD codes must be evaluated based upon the physics of the flowfield and sensitivity to the grid structure. The required tasks to be addressed are:

#### Task 1 — Grid Sensitivity Studies

- 1.1. Perform a detailed grid sensitivity study of 180 deg angle-of-attack case
- 1.2. Exercise the 3-D code for 135 deg angle-of-attack and provide details of the plume-air mixtures and thermodynamic properties of the flow near the Orbiter/ET base.

**Task 2 — Physical Phenomena Validation**

- 2.1. Use available data such as CALSPAN test data as benchmark cases to evaluate the modeling of
  - a. Hot gas/air turbulent mixing, and
  - b. Shock/shear layer interaction

**Task 3 — Document results and prepare a presentation of the results. Give salient features, conclusions and recommendations and provide graphical data to support each aspect of the problem.**

## Section 5

### REFERENCES

- [1] Space Shuttle Generic ETR Plume Heating Data Book — External Tank — Ascent, Doc. No. SSD90D0016, Rockwell International, June 1990.
- [2] Rader, R. J., "Stagnation Heating Rates in Rocket Engine Exhaust Plumes Considering Equilibrium, Frozen, and Finite Rate Chemistry," Northrop TR-230-1186, Jan. 1973.
- [3] Murray, A. L., "Further Enhancements of the BLIMP Computer Code and User's Guide," AFWAL-TR-88-3010, June 1988.
- [4] Schaaf, S. A. and Chambré, P. L., *Flow of Rarefied Gases*, No. 8, Princeton University Press, Princeton, NJ, 1961.

**Appendix A**  
**Two-Species Variable Gamma Formulation**  
**for a Forward-Firing Rocket Nozzle**

## REMTECH TECHNICAL NOTE

---

**SUBJECT:** Two-Species Variable Gamma Formulation for a Forward-Firing Rocket Nozzle

**DATE:** October 8, 1990

**AUTHORS:** Anthony J. Saladino and Sarat C. Prahara]

**CONTRACT NO.:** NAS8-38185

**PREPARED FOR:** George C. Marshall Space Flight Center

---

### BACKGROUND

In the event of an SSME failure during the initial 160 seconds of the shuttle flight, a return-to-launch-site (RTLS) maneuver will be implemented. The period of concern is the power pitch-around maneuver where the vehicle is flying backward at angles-of-attack close to 180 deg. At these attitudes, a very complex flowfield involving severe free-stream/plume interaction affects results. This interaction includes mixing of a high Mach number hot exhaust gas from the two SSME's with the low Mach number free-stream flow. It is believed that the hot gas is basically frozen in concentration levels and is allowed to mix with air through convection and diffusion. The object of this technical note is to develop an algorithm for an axisymmetric case to study the effects of variable  $\gamma$  on the flowfield of a two-species mixture. Since the species diffusion may not play a significant part in the solution of the species continuity equation, it has been neglected in this analysis.

### ANALYSIS

The PARC2DR [1] code was used as the foundation for the Navier-Stokes solver, and the species continuity equation for mass fraction,  $c$ , of the exhaust species was coupled in an explicit fashion to the Navier-Stokes equations via the variable gamma. In two dimensions, the species continuity equation, after it was approximated by dropping the production term and neglecting the diffusion term, is written in physical space coordinates  $(t, x, y)$  as

$$\frac{\partial c}{\partial t} + u \frac{\partial c}{\partial x} + v \frac{\partial c}{\partial y} = 0 \quad (1)$$

which is transformed to computational space coordinates  $(\tau, \xi, \eta)$  as

$$\frac{\partial c}{\partial \tau} + U \frac{\partial c}{\partial \xi} + V \frac{\partial c}{\partial \eta} = 0 \quad (2)$$

where  $\tau = t$ ,  $\xi = \xi(x, y, t)$ ,  $\eta = \eta(x, y, t)$  and the derivatives are transformed by

$$\begin{aligned}\partial_t &= \partial_\tau + \xi_t \partial_\xi + \eta_t \partial_\eta \\ \partial_x &= \xi_x \partial_\xi + \eta_x \partial_\eta \\ \partial_y &= \xi_y \partial_\xi + \eta_y \partial_\eta\end{aligned}\quad (3)$$

$U$  and  $V$  given by

$$\begin{aligned}U &= \xi_t + u\xi_x + v\xi_y \\ V &= \eta_t + u\eta_x + v\eta_y\end{aligned}\quad (4)$$

are the contravariant velocities in the  $\xi$  and  $\eta$  directions respectively, and  $\xi_x$ ,  $\xi_y$ ,  $\eta_x$  and  $\eta_y$  are the metrics ( $\xi_x = \frac{\partial \xi}{\partial x}$ , etc.) required for the transformation of the velocities,  $u$  and  $v$ , in the physical space (in the  $x$  and  $y$  directions, respectively) to computational space. The time derivatives of  $\xi$  and  $\eta$  are zero since the grid is stationary.

Although the Navier-Stokes equations are solved in a steady state mode, the time derivative of the dependent variable is retained so that the resulting equations can be advanced in time steps of  $\Delta\tau$  to a steady state, thereby allowing the solution to adjust to a converged condition over many iterations. Similarly, the species continuity equation (2) retains the time derivative and is solved in a steady-state fashion, where each solution at time step  $n$  is used as the initial condition for the next time step  $n + 1$ ; this process is repeated until the solution  $c$  and the solution vector for the Navier-Stokes equations  $[\rho, \rho u, \rho v, \rho e_{tot}]$  do not change within a predetermined tolerance. Equation (2) can be written in discretized form as

$$c^{n+1} - c^n + \Delta\tau [U\partial_\xi + V\partial_\eta] c^{n+1} = 0 \quad (5)$$

$$\text{with } \partial_\xi = \frac{\partial}{\partial \xi} = \frac{1}{\Delta\xi}$$

$$\text{and } \partial_\eta = \frac{\partial}{\partial \eta} = \frac{1}{\Delta\eta}$$

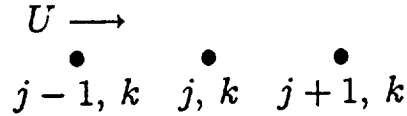
Rewriting Eq. (5) in a direction-split form (ADI, or alternating direction-implicit), results in

$$[I + \Delta\tau U\partial_\xi][I + \Delta\tau V\partial_\eta] c^{n+1} = c^n \quad (6)$$

in which  $I$  is the unit matrix, and a term  $(\Delta\tau^2 UV\partial_\xi\partial_\eta)$ , which is a second order term in time, has been neglected. At small  $\Delta\tau$ , this term is much smaller than terms of the order  $\Delta\tau$ . Therefore, Eq. (6) is the required form for the species continuity equation, and it is first order accurate in time.



In addition, upwinding is necessary so that communication between neighboring points is physically correct. For example, if computations are being performed at grid point  $(j, k)$ , and the



contravariant velocity  $U$  is in the direction toward  $(j, k)$  from  $(j-1, k)$ , then the derivative of  $c$  in the direction of  $\xi$  would be

$$c_{\xi} = c_{j,k} - c_{j-1,k}$$

Since  $c_{j,k}$  is unknown and  $c_{j-1,k}$  is a known value, upwinding also provides computational stability. Covering all possible signs for  $c$ , upwinding for  $c$  in the  $\xi$ -direction becomes

$$\partial_{\xi} c = \begin{cases} c_{j,k} - c_{j-1,k} & , \quad U > 0 \\ \frac{c_{j+1,k} - c_{j-1,k}}{2} & , \quad U = 0 \\ c_{j,k} - c_{j+1,k} & , \quad U < 0 \end{cases} \quad (7)$$

and in the  $\eta$ -direction,

$$\partial_{\eta} c = \begin{cases} c_{j,k} - c_{j,k-1} & , \quad V > 0 \\ \frac{c_{j,k+1} - c_{j,k-1}}{2} & , \quad V = 0 \\ c_{j,k} - c_{j,k+1} & , \quad V < 0 \end{cases} \quad (8)$$

Equations (7) and (8) are associated with the following form of Eq. (6), where absolute values have been taken of  $U$  and  $V$ :

$$[I + \Delta\tau|U|\partial_{\xi}][I + \Delta\tau|V|\partial_{\eta}]c^{n+1} = c^n \quad (9)$$

The solution of Eq. (9) involves solving each direction separately:

$$[I + \Delta\tau|V|\partial_{\eta}]c^{n+1} = \bar{c}^n \quad (10)$$

$$c^{n+1} = \bar{\bar{c}}^n \quad (11)$$

where

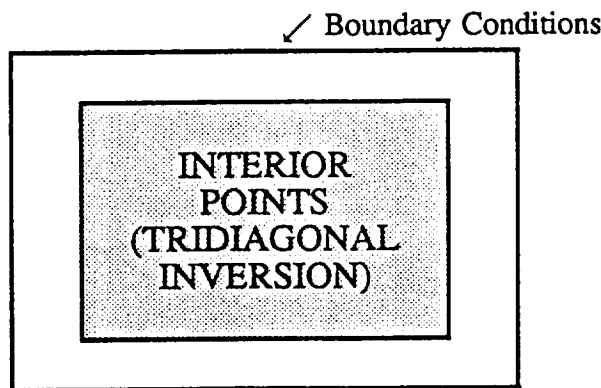
$$\bar{c}^n = [I + \Delta\tau|U|\partial_{\xi}]^{-1} c^n \quad (12)$$

$$\begin{aligned}
 \bar{\bar{c}}^n &= [I + \Delta\tau|V|\partial_{\eta}]^{-1} \bar{c}^n \\
 &= [I + \Delta\tau|V|\partial_{\eta}]^{-1} [I + \Delta\tau|U|\partial_{\xi}]^{-1} c^n
 \end{aligned} \quad (13)$$

Inversion of the bracketed terms in Eqs. (12) and (13) is accomplished by first noting that the resulting solution at point  $j, k$  will involve, at the condition  $U = 0$  (say) points  $j + 1, k$  and  $j - 1, k$ , which corresponds to an equation of no more than 3 points. Therefore, a tridiagonal solver is used to invert Eqs. (12) and (13). The value of  $\Delta\tau$  that is used in the species continuity equation is kept equal to the  $\Delta\tau$  computed from the Navier-Stokes flow solver portion of the code. Using the same  $\Delta\tau$  allows the solution to progress in "time" at the same rate in both the flow solver and the mass fraction solver. Furthermore, the tridiagonal inversion procedure incorporates the mass fraction boundary conditions implicitly to increase the accuracy of and reduce the convergence time of the species continuity solver.

The reason for choosing an implicit, instead of an explicit, mass fraction solver is described briefly below.

When considering the explicit mass fraction solver, only the interior flowfield points are directly involved in the inversion procedure. The boundary points are imposed on the interior points explicitly. For example, if a boundary condition is fixed (free stream) or free (supersonic outflow), these conditions are set at the points corresponding to the indices associated with those boundaries. After this step, the flowfield points are inverted and the boundary points are supposed to feed back into the interior through derivatives.



This is the same procedure which is used to invert the flow solver or Navier-Stokes (N-S) equations in PARC. However, whereas the interior points in the N-S solver transfer information to the boundary points via the derivative term in velocity, there is no such transfer from the interior [Eq. (9)] to the boundary for the mass fraction. For example, the tridiagonal terms in the matrix below are  $D, E$  and  $F$ :

$$\begin{bmatrix} E & F & & & 0 \\ D & & & & \\ & & & & \\ & & & & \\ 0 & & & D & E \end{bmatrix}$$

matrix for interior points in j-direction

where  $E$  is along the diagonal and corresponds to the points  $(j, k)$ ,  $D$  corresponds to points  $(j - 1, k)$  and  $F$  corresponds to points  $(j + 1, k)$ . Eq. (9) can be written for the  $j$ -direction only as

$$[I + \Delta\tau U \partial_\xi] c^{n+1} = c^n \tag{14}$$

so that if  $U$  is greater than zero, then Eq. 14 can be written as

$$c_{j,k}^{n+1} + \Delta\tau U (c_{j,k}^{n+1} - c_{j-1,k}^{n+1}) = c_{j,k}^n \tag{15}$$

for a single value of  $j$  and  $k$ . Equation (15) can be rewritten in matrix form for different values of  $j$  and constant  $k$  as

$$\begin{bmatrix} (1 + \Delta\tau U) & & & 0 \\ (-\Delta\tau U)(1 + \Delta\tau U) & & & \\ & \ddots & & \\ & & & (-\Delta\tau U) & (1 + \Delta\tau U) \\ & & 0 & & \end{bmatrix} \begin{bmatrix} c_{2,1} \\ c_{3,1} \\ \vdots \\ \vdots \\ c_{J_m,1} \end{bmatrix}^{n+1} = \begin{bmatrix} c_{2,1} \\ c_{3,1} \\ \vdots \\ \vdots \\ c_{J_m,1} \end{bmatrix}^n \tag{16}$$

where  $j$  goes from 2 to  $J_m$  ( $j = 1$  and  $j = j_{max}$  are boundaries),

$$J_m = j_{max} - 1 \tag{17}$$

and

$$\begin{aligned} D &= -\Delta\tau U \\ E &= 1 + \Delta\tau U \\ F &= 0 \end{aligned} \tag{18}$$

As Eq. (15) indicates for  $j = 2$ , values of  $c$  at location  $(1, k)$  would be required to evaluate  $c_{2,k}$ . However, location  $(1, k)$  is a boundary point and cannot be included in the vector of  $c$  values in Eq. (16) since this is a matrix inversion for interior points only. Consequently, the boundary information for  $c$  is not being communicated to the interior points, resulting in a non-changing value for  $c_{2,k}$ , regardless of the initial values (for  $U < 0$ , the same argument holds true at inflow boundaries; since there are boundaries in the forward-firing nozzle problem in which  $U < 0$  coexists with  $U > 0$ , the final value of  $c$  will be zero everywhere, regardless of the initial values, due to the influence of both types of boundaries on the interior point calculations).

Another way of describing the situation above is by making reference to the N-S equations. The explicit solution of the N-S equations as programmed in the original PARC code did not encounter such boundary communication problems for the solution to the interior points. The corresponding vector  $c$  in Eq. (16) would be a vector of  $Q$  values such that in a single direction,

$$[I + \Delta\tau \partial_\xi A] \Delta Q^{n+1} = RHS \tag{19}$$

where  $A$  is proportional to  $U$ . Since the N-S equations include terms related to the spatial derivative of velocity  $((\partial_\xi U) Q^{n+1})$ , the tridiagonal terms, for a boundary point at  $(j-1, k)$  and interior points at  $(j, k)$  and  $(j+1, k)$ , are proportional to

$$\begin{aligned} D &\propto \Delta\tau U(j-1, k) \\ E &\propto 1 + \Delta\tau U(j, k) \\ F &\propto \Delta\tau U(j+1, k) \end{aligned} \quad (20)$$

The situation for the mass fraction equation is such that terms  $(U \partial_\xi c^{n+1})$  result, leading to

$$\begin{aligned} D, F &\propto \Delta\tau U(j, k) \\ E &\propto 1 + \Delta\tau U(j, k) \end{aligned} \quad (21)$$

where the  $U$  is now evaluated at point  $(j, k)$  only, so that there is no communication from the boundary to the interior through  $U$ . Although derivative terms for  $c$  do appear in Eq. (9), these are part of the solution vector  $c^{n+1}$  whose indices only include the interior points.

Therefore, the implicit method was applied to the solution of the mass fraction equation by appending the boundary condition equation to the interior point Eq. (9). The form for the boundary condition equations is different from those of the interior according to the boundary type — fixed (Dirichlet-type), isothermal (Neumann-type), etc.

Once the mass fraction  $c$  of the exhaust species is computed at all points, the ratio of specific heats  $\gamma$  for the mixture is found as

$$\gamma_m = \frac{c c_{p1} + (1-c)c_{p2}}{c c_{v1} + (1-c)c_{v2}} = \frac{c_{p_m}}{c_{v_m}} \quad (22)$$

$c_p$  and  $c_v$  are the specific heats at constant pressure and constant volume, respectively, for species 1 or 2, and subscript  $m$  denotes a mixture. Coupling between the species continuity equation and the flow solver is accomplished through an equation of state of the form

$$p = (\gamma_m - 1)\rho e_{int} \quad (23)$$

where  $p$  is pressure,  $\rho$  is density and  $e_{int}$  is internal energy, with  $\gamma_m$  following from Eq. (22).

To accommodate the difference in the free-stream and exit nozzle value of gamma in the normalization of PARC, the following changes had to be made.

Within the PARC code, the equation of state variables are normalized with respect to free-stream conditions as

$$\begin{aligned} \bar{p} &= \frac{p}{\rho_\infty a_\infty^2} & \bar{\rho} &= \frac{\rho}{\rho_\infty} \\ \bar{T} &= \frac{T}{T_\infty} & \bar{a} &= \frac{a}{a_\infty} \end{aligned} \quad (24)$$

where the overbar denotes a non-dimensional quantity,  $a$  is the speed of sound,  $T$  is the temperature, and  $\infty$  corresponds to free stream.

In the calculation of the speed of sound or temperature, the updated code utilizes the nondimensional equations:

$$a^2 = \frac{\gamma_m p}{\rho} \longrightarrow \bar{a}^2 = \frac{\gamma_m \bar{p}}{\bar{\rho}} \quad (25)$$

$$p = \rho R T \longrightarrow \bar{T} = \frac{\gamma_\infty \bar{p}}{\bar{\rho}} \quad (26)$$

where the  $\gamma_m$  in Eq. (25) was equal to  $\gamma_\infty$  in the original code [1], since  $\gamma$  was the same at every point in the flow. For the present variable gamma approach, the constant GAMAREF was changed to GAMMA(J,K) (as computed from Eq. 22), with the reference or constant (free-stream) value GAMAFS used in the calculation of temperature only and the local value of GAMMA(J,K) used to determine the speed of sound.

One final consideration is needed to correctly account for the two-species variable gamma effects on the flowfield. This becomes important whenever the two species have different atomic weights. The equation of state is written in the usual form for a single species as

$$p = \rho R T \quad (27)$$

where  $R = \frac{\hat{R}}{M}$ , and  $\hat{R}$  is the universal gas constant. Eq. (27) can be normalized as

$$\bar{p} \rho_\infty a_\infty^2 = \bar{\rho} \rho_\infty R \bar{T} T_\infty$$

$$\text{or,} \quad \bar{p} = \bar{\rho} \bar{T} \frac{T_\infty R}{a_\infty^2} \quad (28)$$

$$\text{or,} \quad \bar{p} = \frac{\bar{\rho} \bar{T}}{\gamma_\infty}$$

since

$$\gamma_\infty R T_\infty = a_\infty^2 \quad (29)$$

For two species,  $R$  must be replaced by the gas constant for the mixture,  $R_m$ :

$$p = \rho R_m T \quad \text{where,} \quad (30)$$

$$R_m = \frac{\hat{R}}{M_m}$$

and  $M_m$  is the local mixture mass, so that upon normalizing Eq. (30),

$$\bar{p} = \bar{\rho} \bar{T} \frac{R_m T_\infty}{a_\infty^2} \quad (31)$$

The mixture gas constant involves a summation over each species  $i$ ,

$$R_m = \sum_i c_i R_i \quad (32)$$

$$\begin{aligned} \bar{p} &= \bar{\rho} \bar{T} \frac{T_\infty}{a_\infty^2} \sum_i c_i R_i \\ &= \frac{\bar{\rho} \bar{T}}{\gamma_\infty R_\infty} \sum_i c_i R_i \quad \text{from Eq. (29)} \end{aligned} \quad (33)$$

Also,

$$R_i = c_{p_i} - c_{v_i} \quad (34)$$

Substituting Eq. (34) into Eq. (33) results in

$$\begin{aligned} \bar{p} &= \frac{\bar{\rho} \bar{T}}{\gamma_\infty} \frac{\sum_i c_i (c_{p_i} - c_{v_i})}{R_\infty} \\ &= \frac{\bar{\rho} \bar{T}}{\gamma_\infty} \frac{c_{p_m} - c_{v_m}}{R_\infty} \quad \text{from Eq. (22)} \\ &= \frac{\bar{\rho} \bar{T}}{\gamma_\infty} \frac{(\gamma_m - 1) c_{v_m}}{R_\infty} \end{aligned} \quad (35)$$

Finally, the equation of state for two species can retain the form it had for a single species by writing Eq. (35) as

$$\bar{p} = \frac{\bar{\rho} \bar{T}}{\bar{\gamma}} \quad (36)$$

where

$$\bar{\gamma} = \frac{\gamma_\infty R_\infty}{(\gamma_m - 1) c_{v_m}} \quad (37)$$

A similar normalization of the first law of thermodynamics results in

$$\bar{p} = (\gamma_m - 1) \bar{\rho} \overline{e_{int}} \quad (38)$$

in nondimensional form. The temperature is then obtained from Eq. (36) in place of Eq. (26).

## RESULTS

In order to validate the above algorithm, a few cases were examined. Results for a forward-firing sonic jet are shown for two cases below. Both cases have a ratio of specific heats equal to 1.382 in the external region of the flowfield and a free-stream Mach number of 6.7. Case 1 uses a  $\gamma$  of 1.4 at the nozzle exit, and Case 2 uses a  $\gamma$  of 1.3 at the nozzle exit. Case 1 corresponds to the experimental test case [2], which has nitrogen as the exhaust gas and a combusted mixture of methane and air as the free-stream gas. In both cases the conditions in the free stream are

$$M_{\infty} = 6.7$$

$$p_{\infty} = 0.3084 \text{ psia}$$

$$T_{\infty} = 332.53^{\circ} \text{ R.}$$

$$T_{t\infty} = 3318^{\circ} \text{ R.}$$

$$Re_{\infty}/\text{ft} = 1.4 \times 10^6$$

$$\gamma_{\infty} = 1.382$$

and the total conditions in the sonic nozzle are

$$T_t = 495^{\circ} \text{ R.}$$

$$p_t = 44.206 \text{ psia}$$

$$p_{t_j}/p_{t_2} = 2.46$$

Since the O/F ratio of the nozzle exhaust was not known from any of the literature available, evaluation of the exhaust and free-stream conditions was made in the following manner. Determination of a mixture  $\gamma$  at each flowfield point requires knowing  $c_{p_i}$  and  $c_{v_i}$ . Values of  $c_p$  for the free stream and exhaust species were obtained from JANNAF tables, where air was assumed to be the free-stream fluid, and  $N_2$  was taken as the exhaust specie. The corresponding value of  $\gamma$  for air is 1.382, which was obtained from [3], and the exhaust  $\gamma$  was chosen to be either 1.4 (Case 1) or 1.3 (Case 2). The specific heat at constant volume was then calculated from the relation

$$c_{v_i} = \frac{c_{p_i}}{\gamma_i}, \quad i = 1, 2 \quad (39)$$

This procedure allows the computation of  $\gamma_m$  to be made, but since the value of  $R_m$  is sensitive to the physically correct values of  $c_{p_i}$  and  $c_{v_i}$ ,  $\bar{\gamma}$  will not be physically accurate (correct values of  $c_p$ ,  $c_v$  and  $\gamma$  can be determined for the exhaust and free-stream gas when the ODE (One-Dimensional-Equilibrium) computer code is run). Therefore, within the species solver,  $\bar{\gamma}$  was taken to be equal to  $\gamma_m$ . Diffusion was assumed to be negligible for the blunt-body flowfield of the forward-firing nozzle. Inclusion of diffusion will be exercised at a later date to assess the importance of this term. A figure taken from Ref. [2] is shown in Fig. 1 to clarify the nomenclature used in the following discussion.

## Case 1

Contour plots of pressure, mass fraction of the exhaust species ( $c = 1$  at the nozzle exhaust and  $c = 0$  in the external region) and of the ratio of specific heats is shown in Figs. 3 through 5, where a plot of normalized pressure contours is given in Fig. 2 for the case where  $\gamma = 1.4$  everywhere for a single species model.

The value of gamma is equal to 1.4 everywhere in Fig. 2; in Fig. 3, gamma in the free stream is 1.382 and at the nozzle exit is 1.4. Comparison of Figs. 2 and 3 indicate equivalent pressure contour values and shock locations. In addition, the mainstream bow shock is slightly closer to the nozzle for the case where  $\gamma$  in the free stream is 1.382 (Fig. 3) as compared to the case where  $\gamma$  is 1.4 in the free stream (Fig. 2). Figures 4 and 5 show similar trends in  $c$  and  $\gamma$ , respectively, in which the values at the nozzle exit change smoothly to the free-stream values as one moves from the nozzle outward. The location of maximum change in  $c$  and  $\gamma$  occurs in a region normal to the nozzle axis, and is associated with the shear layer located between the mainstream bow shock and the jet normal shock. Figure 6 is a side-by-side comparison of Mach number contours generated by the variable-species option and the experimental results of [2]. The reattachment shock starting behind the jet lip is clearly seen in the Mach number plot.

The next set of plots depicts the case in which  $\gamma_e = 1.4$ , but includes a Wilke mixture formulation for both viscosity  $\mu$  and thermal conductivity  $k$  to account for the effects of a frozen mixture of two species. This is accomplished by utilizing a Sutherland formula for each species  $i$  to compute individual transport properties  $\mu_i$  and  $k_i$ . These values are combined along with the mass fraction  $c_i$  into a mixture value for  $\mu$  and  $k$ . Figures 7 through 10 show no difference in the behavior of the flowfield as compared to the Sutherland approximation for a single species as a function of temperature (Figs. 3 through 6). Nevertheless, the Wilke formulation will be important for problems in which diffusion is not negligible and/or problems with more than two dominant species.

## Case 2

In anticipation of a forward-firing SSME engine with an equivalent mass flow rate equal to two SSME's, whose nozzle exhaust gamma is 1.3, the gamma for the nozzle in this study was changed to 1.3 (while retaining a free-stream gamma of 1.382). Results for this case appears in Figs. 11 to 14. Pressure contours (Fig. 11) indicate that the jet normal shock is somewhat farther from the nozzle exit as compared to the case where gamma at the exit was equal to 1.4. A calculation of  $p^*/p_t$  for a sonic nozzle (sonic divided by total) shows that the pressure is indeed larger at the nozzle exit when the value of gamma is smaller. The shock system between Case 1 and Case 2 is very similar. Exhaust mass fraction contours (Fig. 12) range from 1.0 at the nozzle exit to 0.0 in the free stream with a similar trend as in Case 1. The region of lower contour values near the nozzle corner is due to recirculation which can be seen in the Mach number plot. This region of reduced exhaust mass fraction occurs in the expansion fan emanating from the jet lip.



Evidently, lower value of  $c$  corresponding to the regions farther from the nozzle made their way to the expansion fan and did not reduce to zero as it did in Case 1.

Figure 13 indicates the gamma contours with  $\gamma = 1.3$  at the nozzle exit and  $\gamma = 1.382$  in the free stream. The region of largest gradient is along the axis and corresponds to the jet-free-stream interface or shear layer. As the flow travels to the backside of the nozzle, the (convective) mixing region extends over a larger portion of the flowfield; the gradients in the mass fraction and gamma are more gradual on account of the decreased velocity. A Mach contour plot (Fig. 14) describes the velocity field as in Case 1, where the jet normal shock stands farther out from the nozzle exit with the lower  $\gamma$ . The secondary reattachment shock is clearly indicated in Fig. 14.

The final plot (Fig. 15) is a side-by-side comparison of the Mach number contours from the two-species variable gamma cases (with  $\gamma_e = 1.4$  and  $\gamma_e = 1.3$ ). This figure reveals the difference in the locations of the respective jet normal shocks. Only the Sutherland transport property formulation for a single species is used. The lower gamma at the exhaust results in a jet normal shock that lies slightly farther from the nozzle exit.

## REFERENCES

1. Liver, P. A. and Praharaj, S. C., "Upgrade of and Numerical Experiment with PARC for Hypersonic Flow over a Hemisphere-Cylinder Configuration," REMTECH Report RTR 181-01, Feb. 1989.
2. Nowak, Robert J., "Gas-Jet and Tangent-Slot Film Cooling Tests of a 12.5° Cone at Mach Number of 6.7," NASA Technical Paper 2786, May 1988.
3. Macaraeg, M. G., "Numerical Models of Two Complex Hypersonic Flows," *Journal of Thermophysics*, Vol. 3, No. 2, April 1989, pp. 97-104.

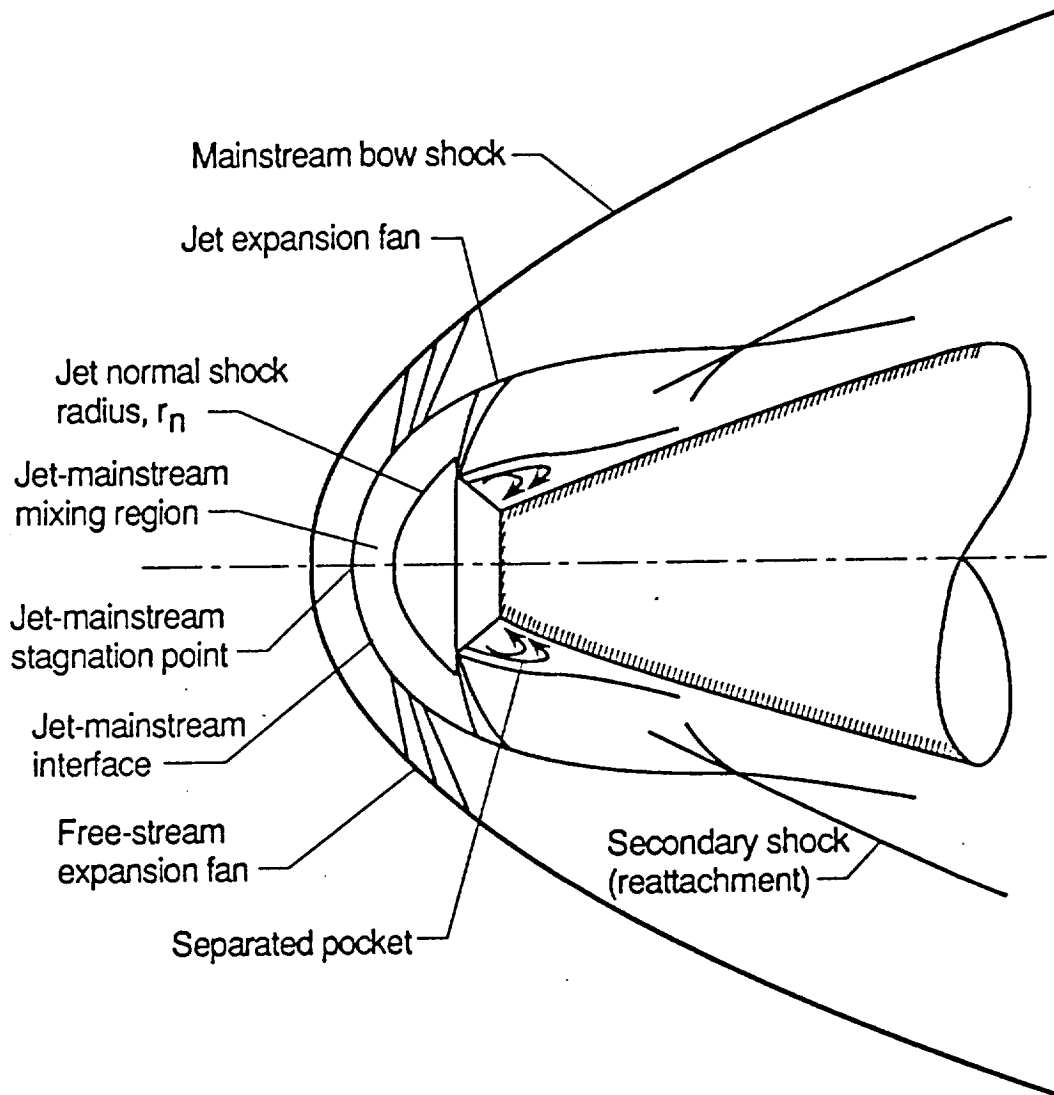


Figure 1: Gas-Jet Shock Schematic (Adapted from Ref. 2)

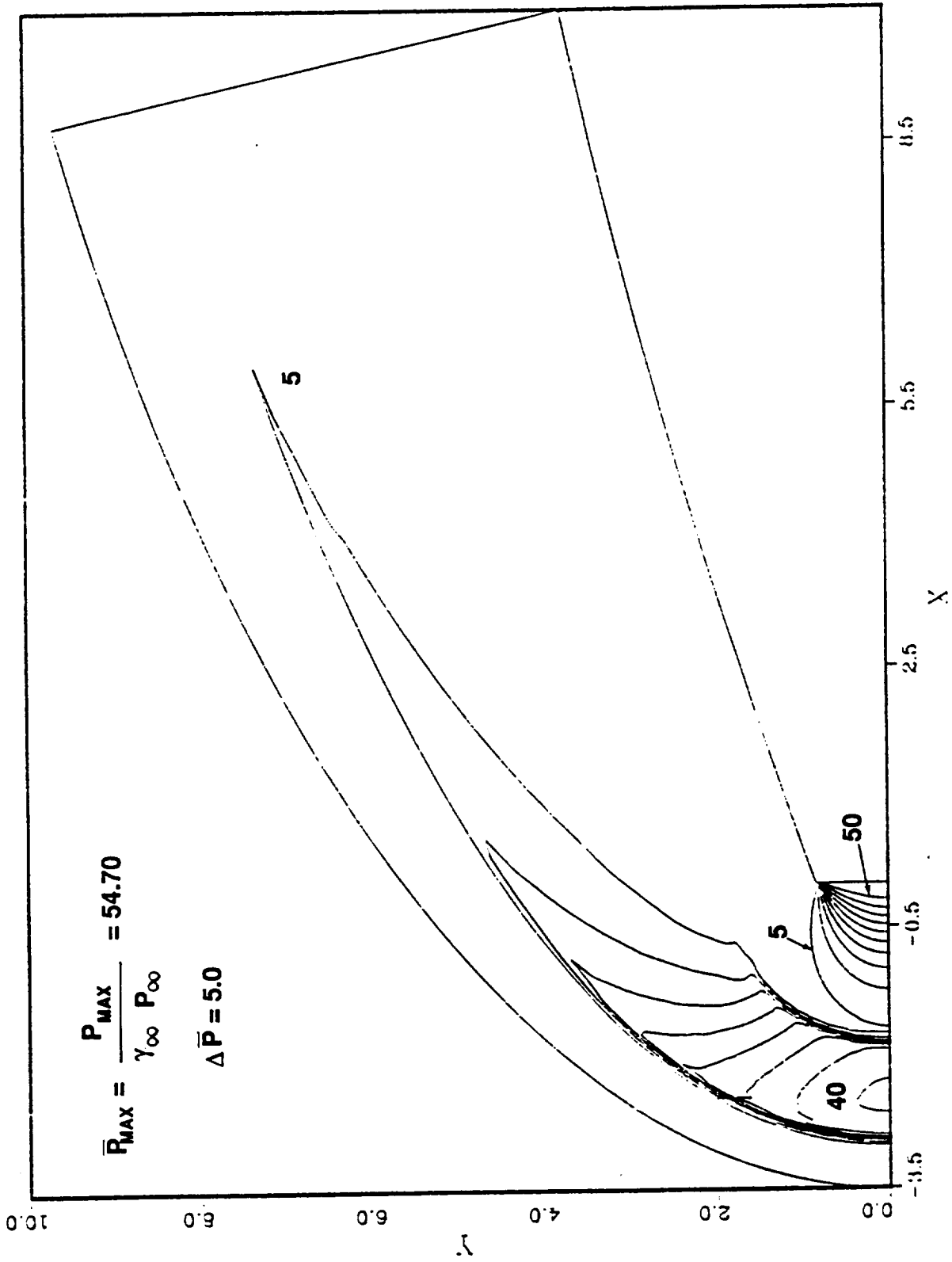


Figure 2: Normalized Pressure Contours for the Single-Species Formulation with Gamma = 1.4 Everywhere

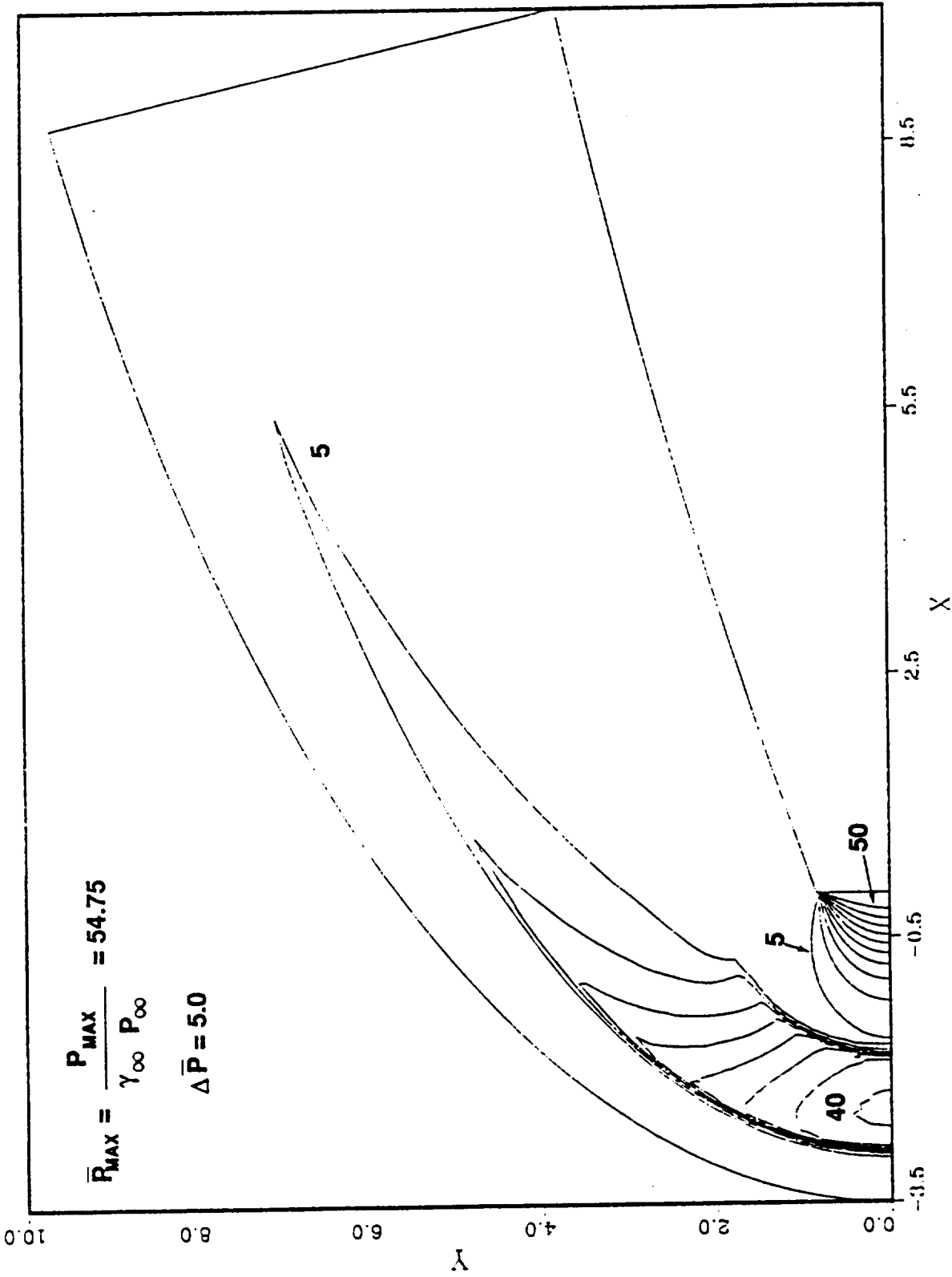


Figure 3: Normalized Pressure Contours for the Two-Species Formulation (Exhaust Gamma = 1.4, Free-Stream Gamma = 1.382)

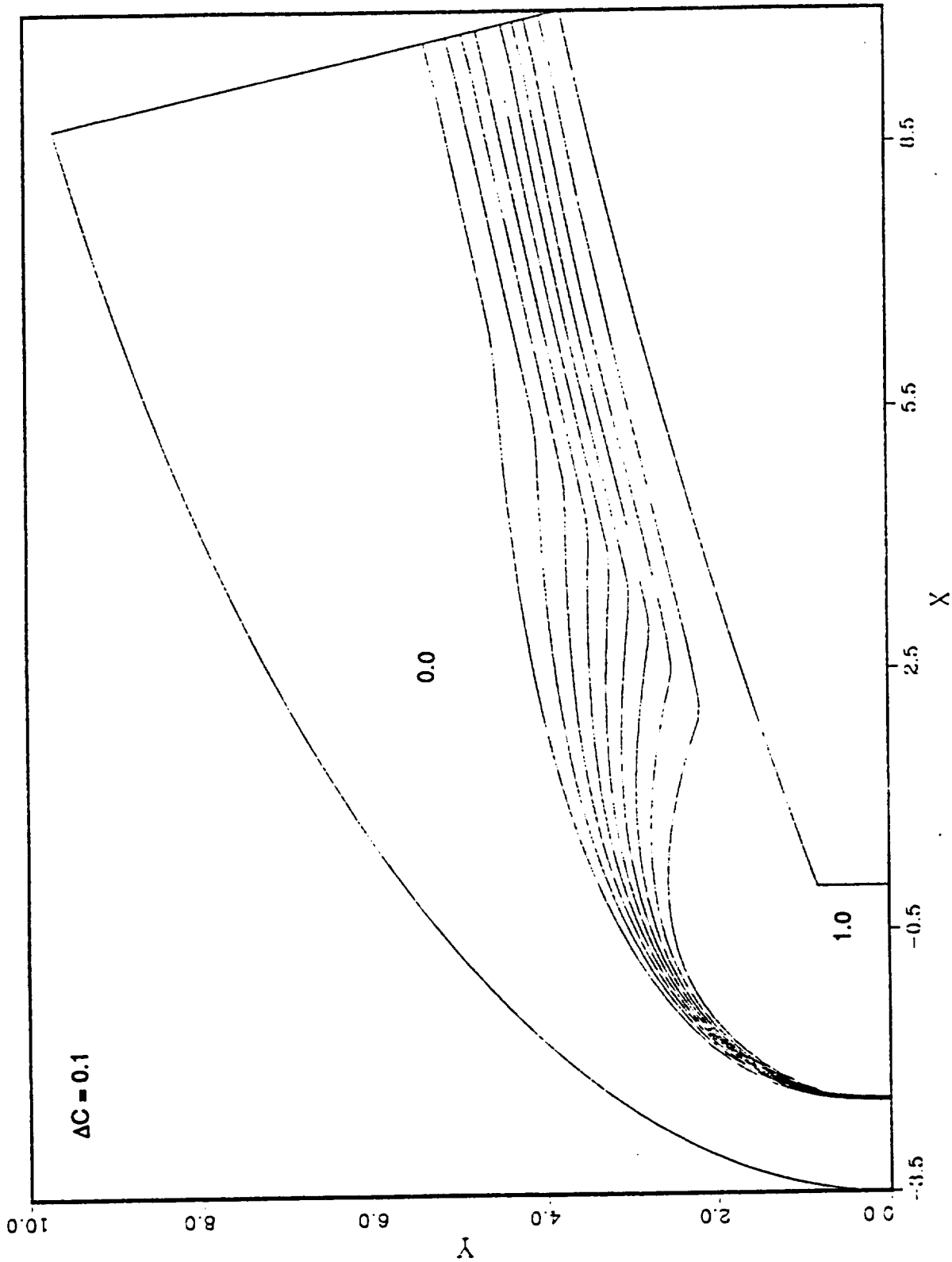


Figure 4: Exhaust Mass Fraction Contours for the Two-Species Formulation (Exhaust Gamma = 1.4, Free-Stream Gamma = 1.382)

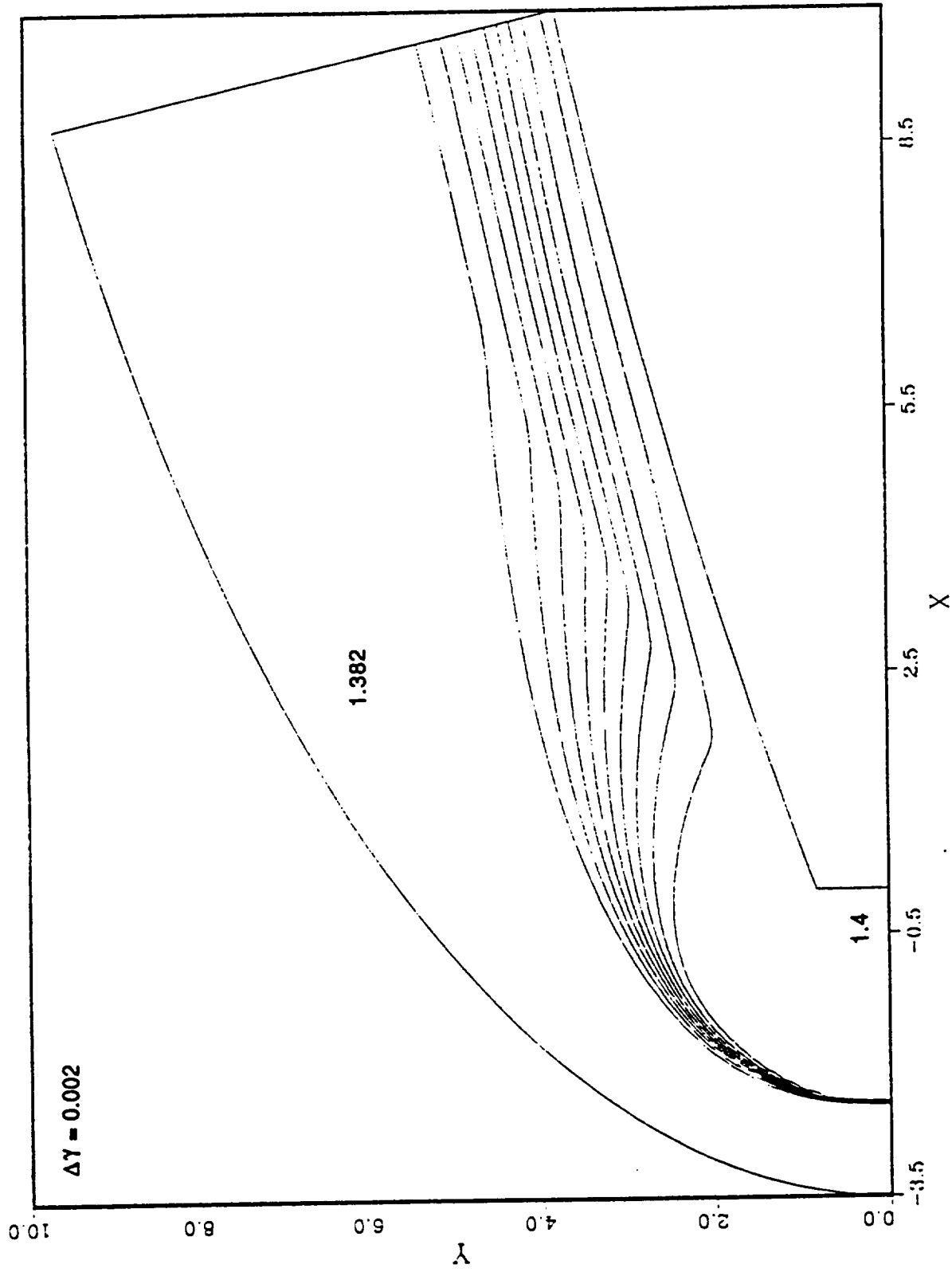


Figure 5: Variable Gamma Contours for the Two-Species Formulation (Exhaust Gamma = 1.4, Free-Stream Gamma = 1.382)

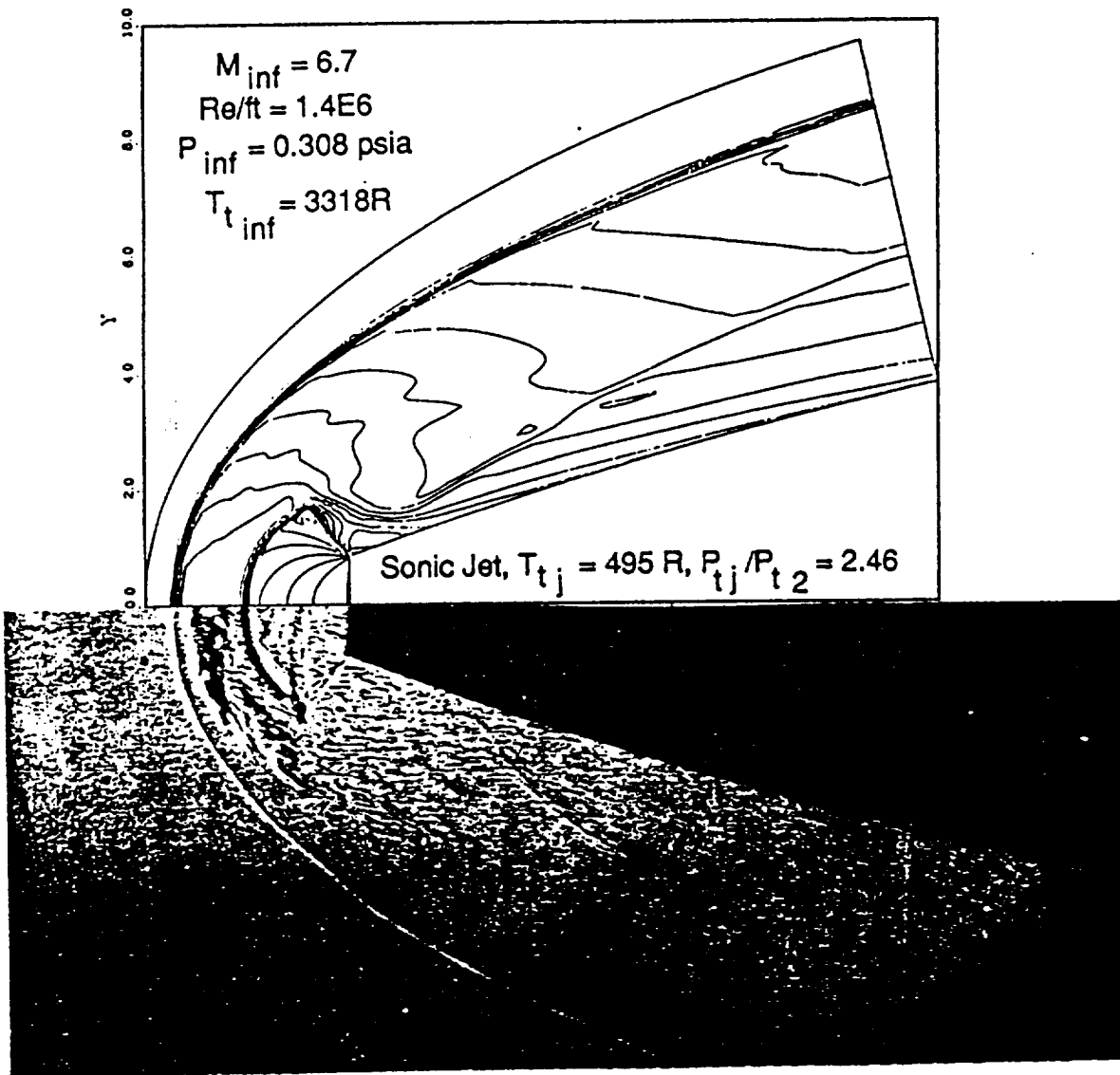


Figure 6: Mach Contour Comparison Between Two-Species Variable Gamma Results (Exhaust Gamma = 1.4, Free-Stream Gamma = 1.382) and Ref. 2

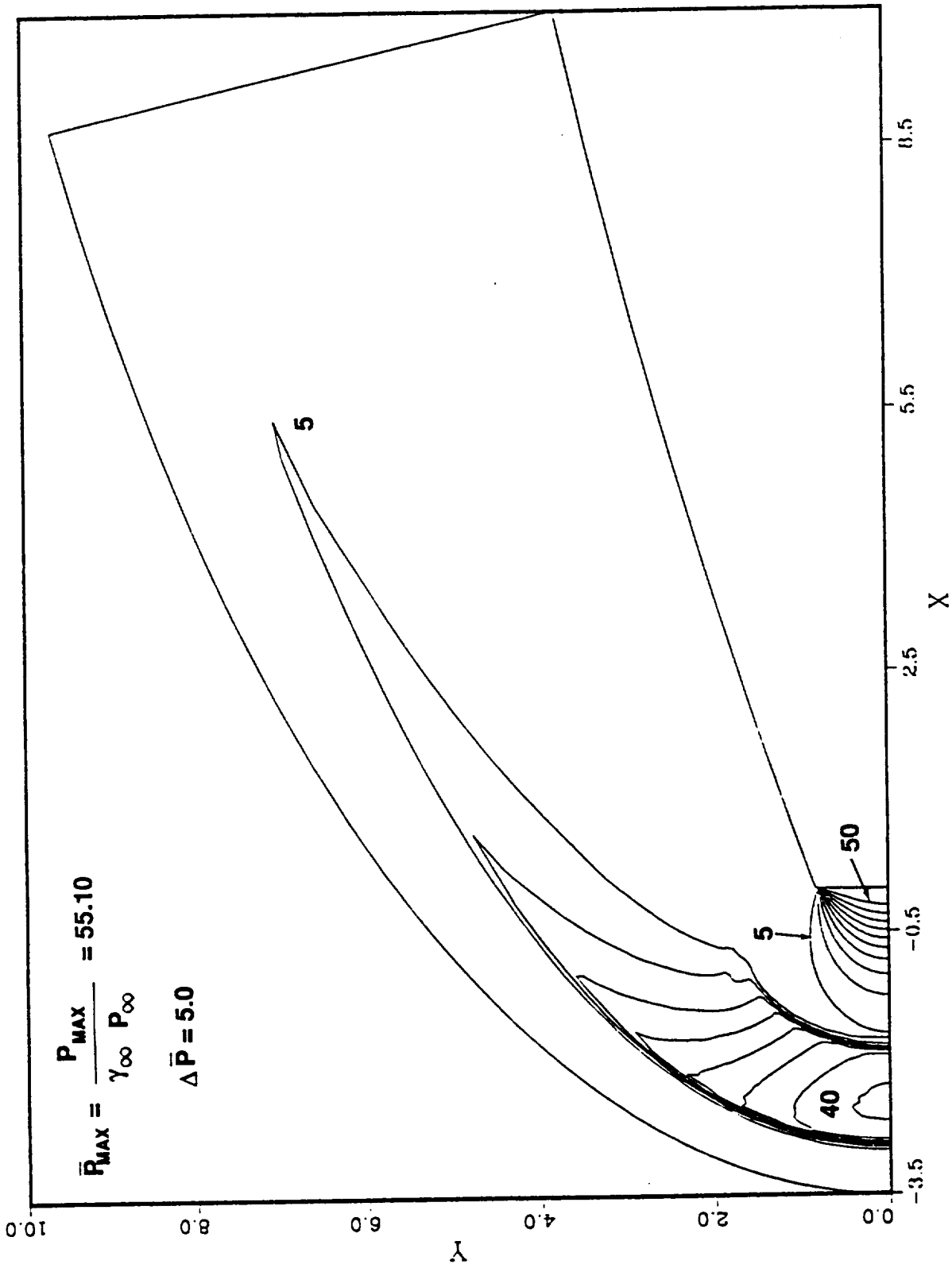


Figure 7: Normalized Pressure Contours for the Two-species Formulation Using Wilke Mixture Formulas for  $\mu$  and  $k$  (Exhaust Gamma = 1.4, Free-Stream Gamma = 1.382)



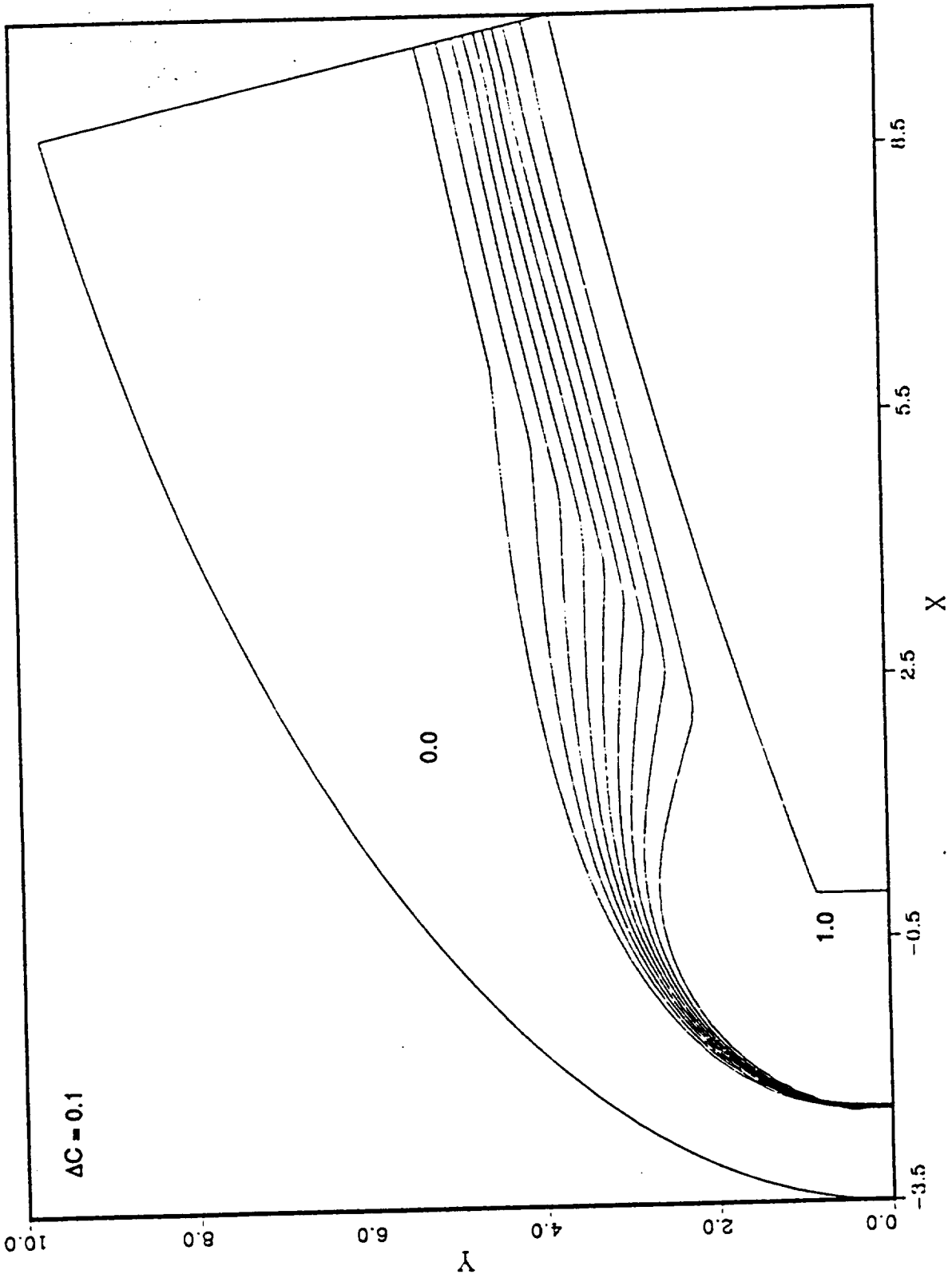


Figure 8: Exhaust Mass Fraction Contours for the Two-Species Formulation Using Wilke Mixture Formulas for  $\mu$  and  $k$  (Exhaust Gamma = 1.4, Free-Stream Gamma = 1.382)

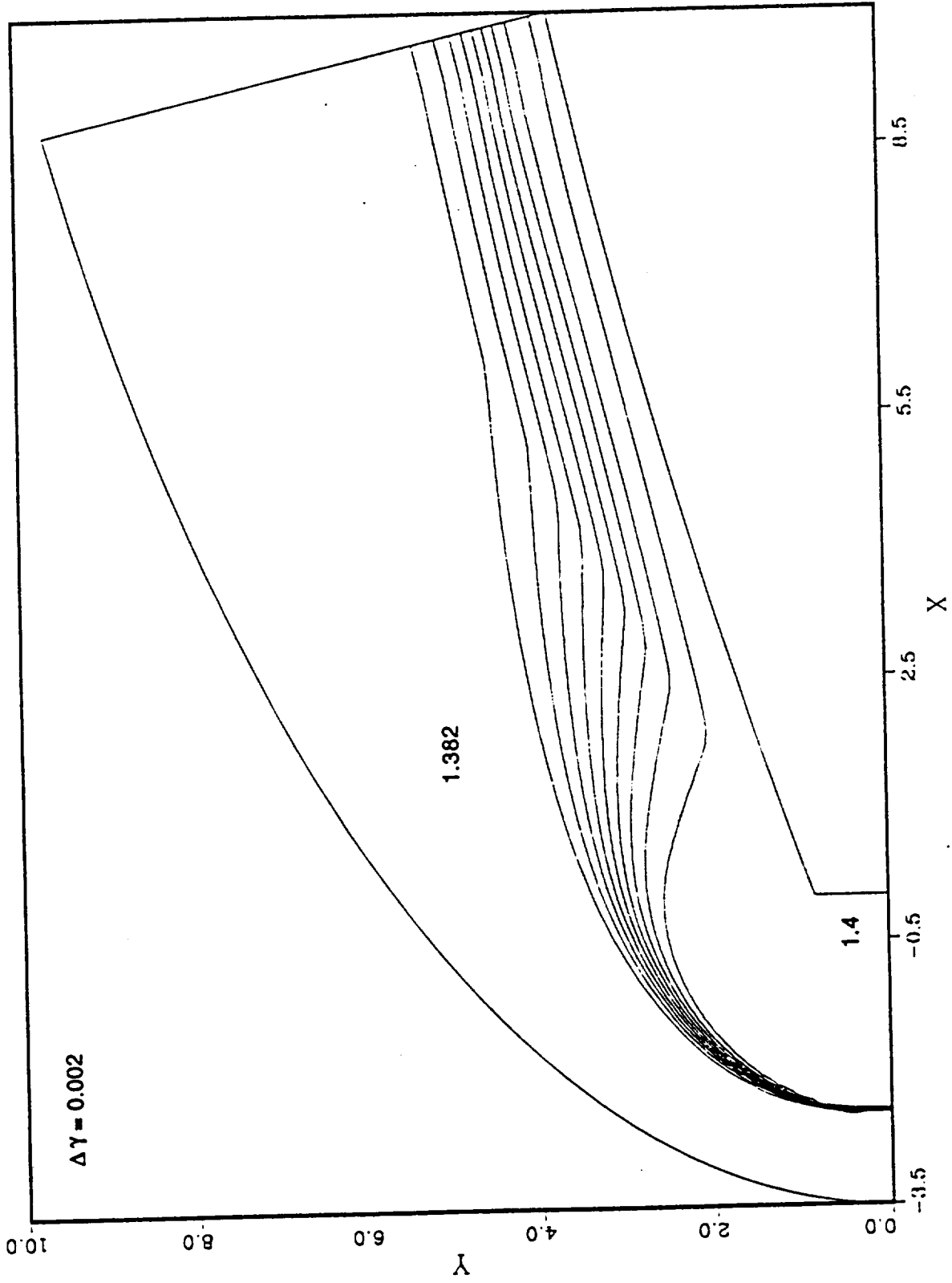


Figure 9: Variable Gamma Contours for the Two-Species Formulation Using Wilke Mixture Formulas for  $\mu$  and  $k$  (Exhaust Gamma = 1.4, Free-Stream Gamma = 1.382)

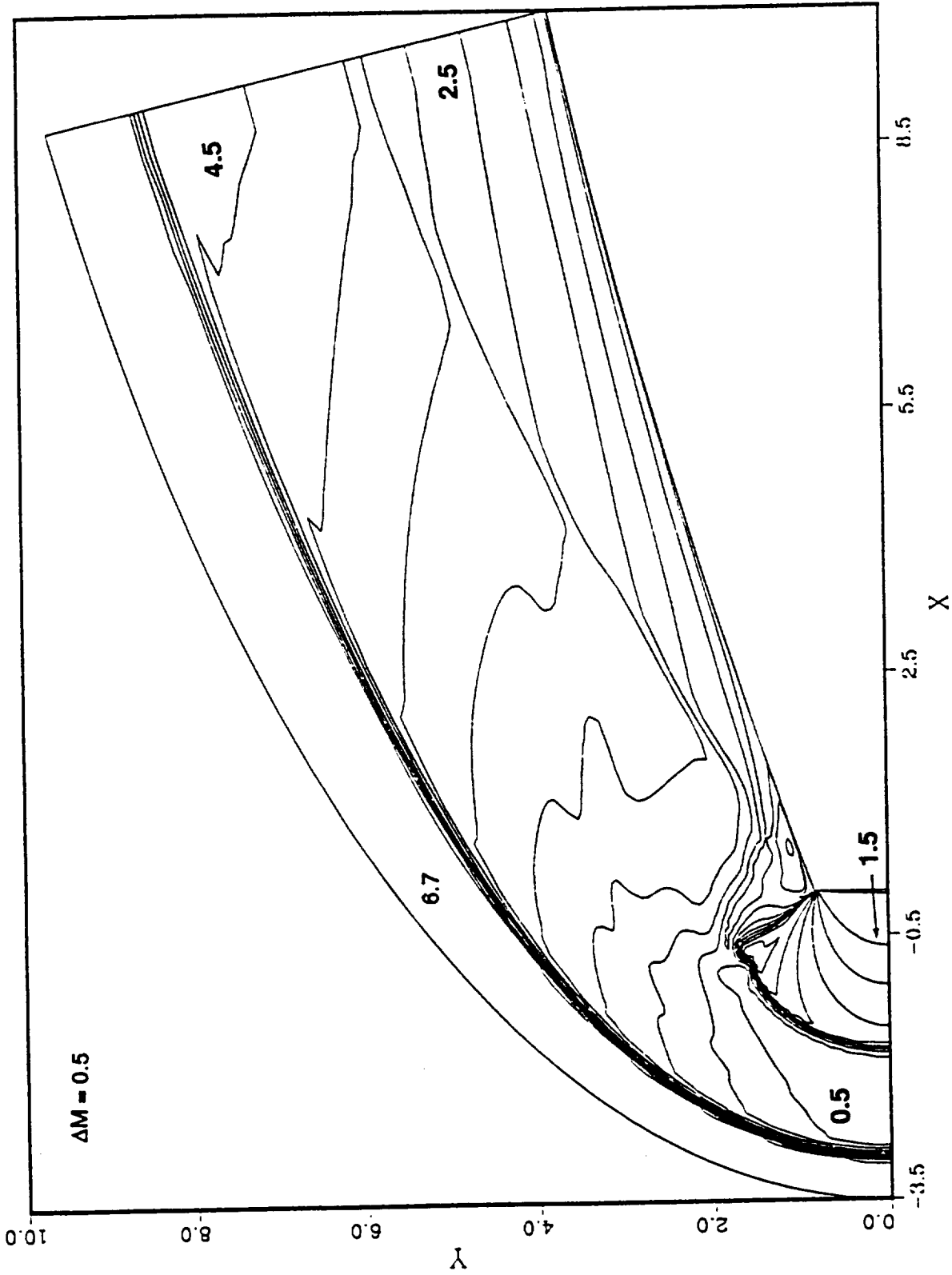


Figure 10: Mach Number Contours for the Two-Species Formulation Using Wilke Mixture Formulas for  $\mu$  and  $k$  (Exhaust Gamma = 1.4, Free-Stream Gamma = 1.382)

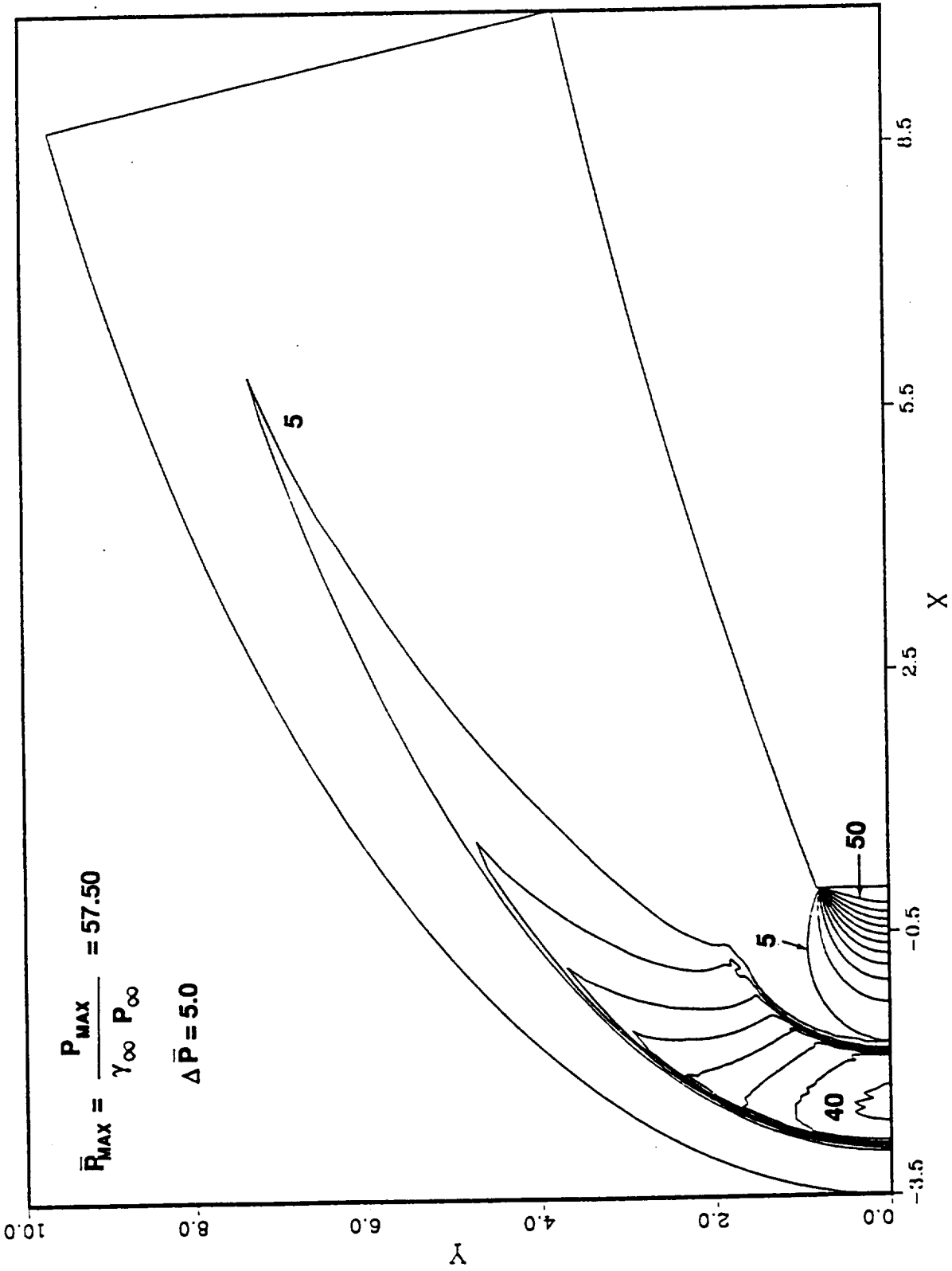


Figure 11: Normalized Pressure Contours for the Two-Species Formulation (Exhaust Gamma = 1.3, Free-Stream Gamma = 1.382)

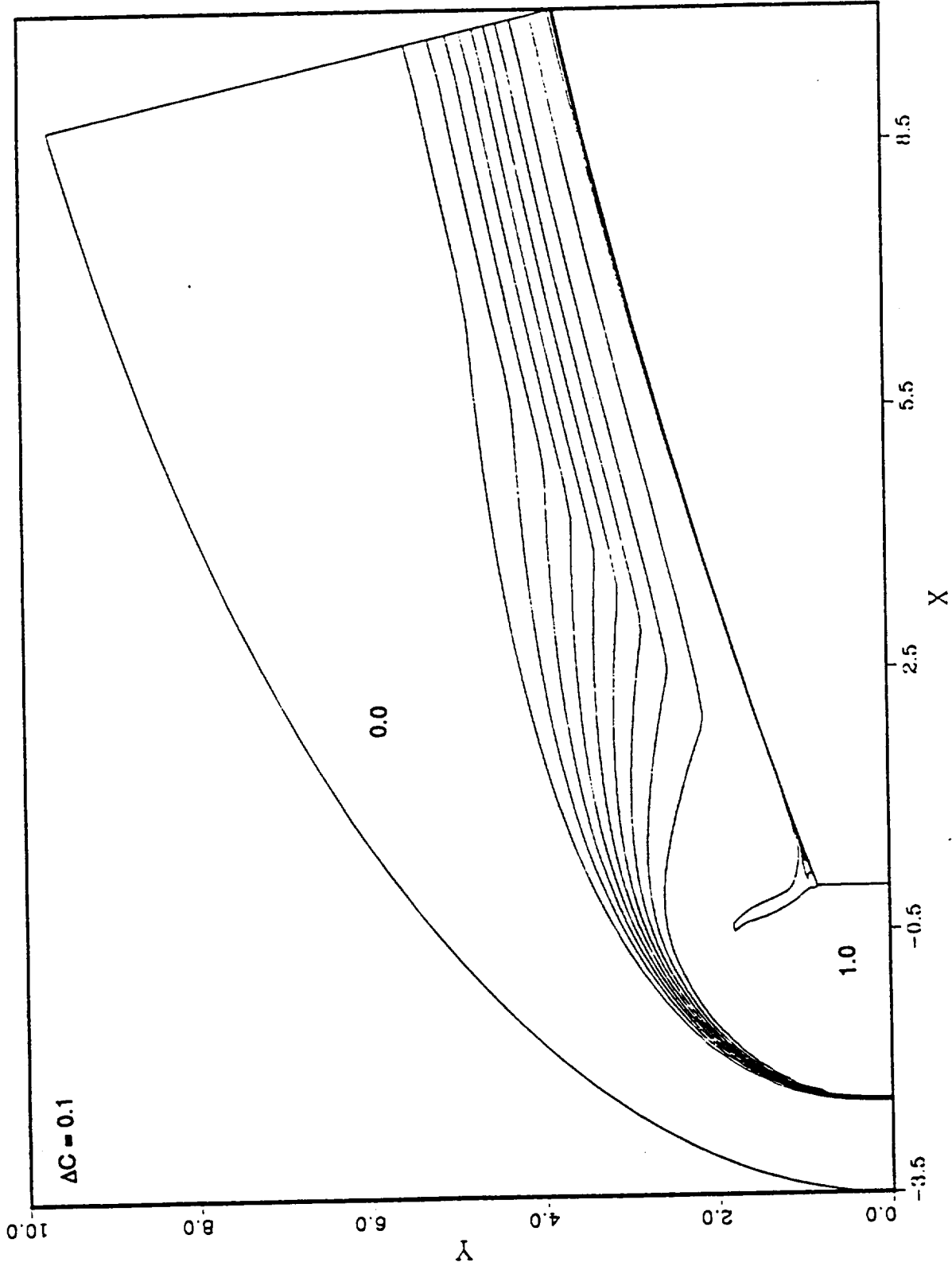


Figure 12: Exhaust Mass Fraction Contours for the Two-Species Formulation (Exhaust Gamma = 1.3, Free-Stream Gamma = 1.382)

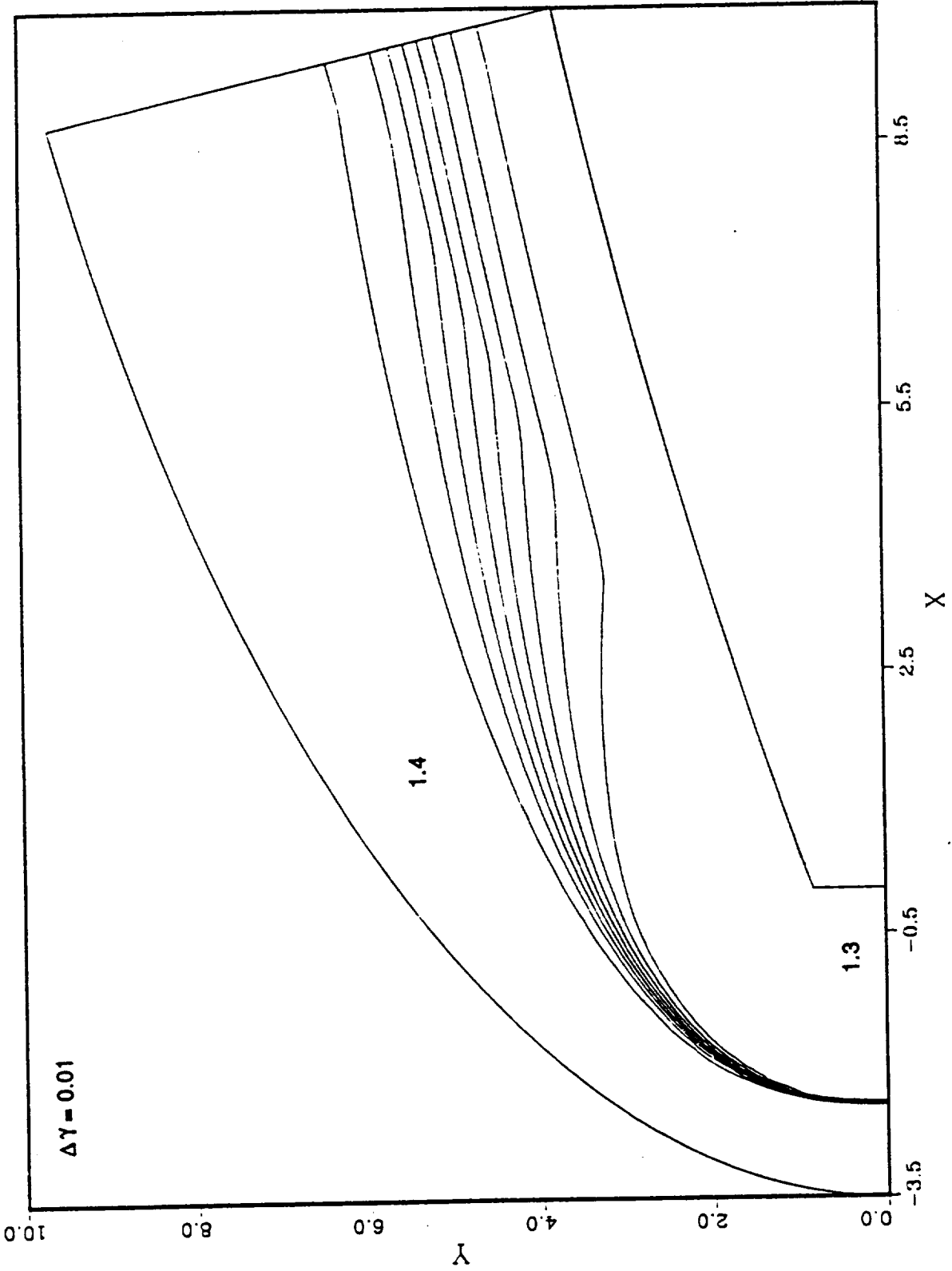


Figure 13: Variable Gamma Contours for the Two-Species Formulation (Exhaust Gamma = 1.3, Free-Stream Gamma = 1.382)

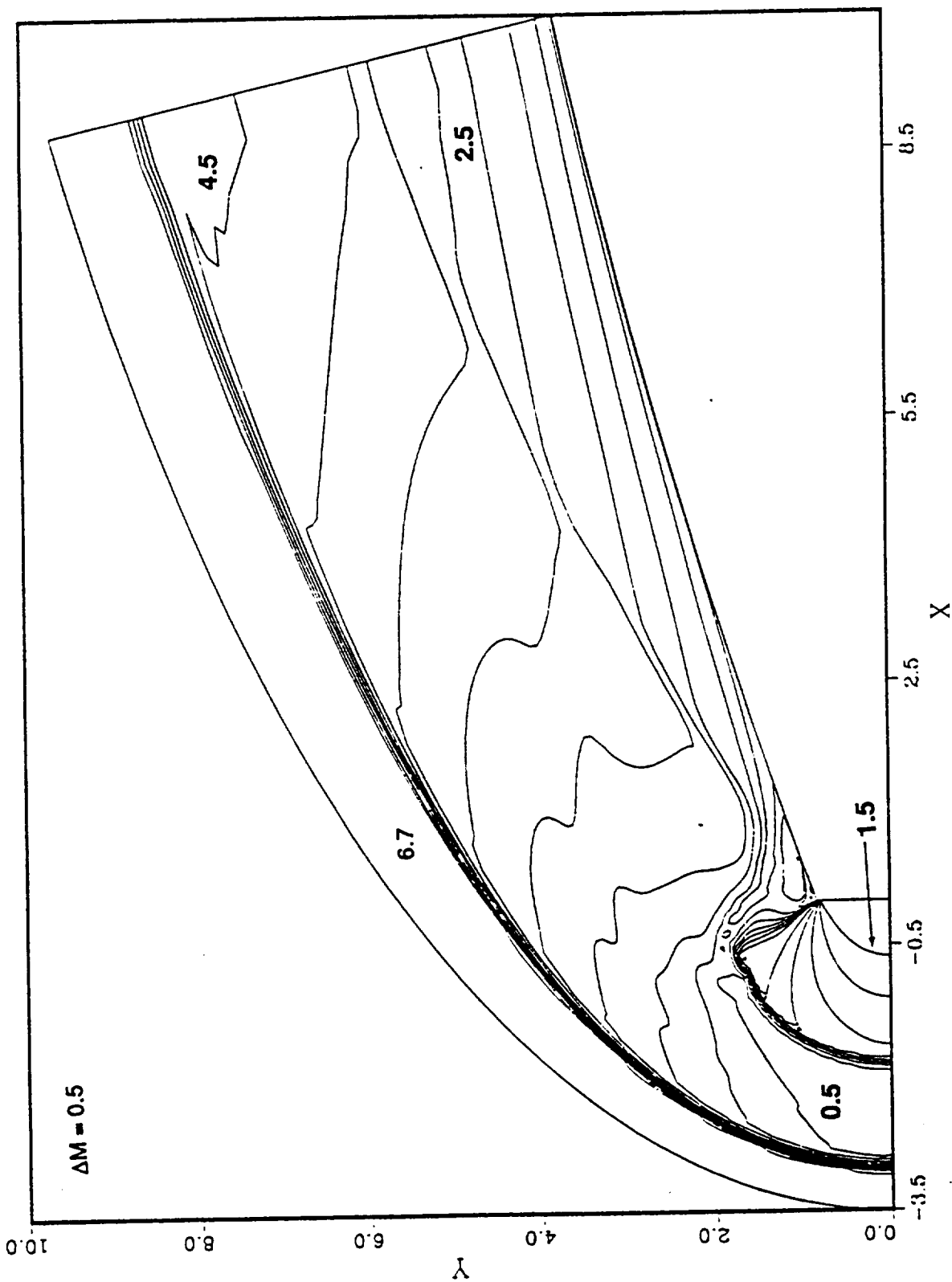


Figure 14: Mach Number Contours for Two-Species Formulation (Exhaust Gamma = 1.3, Free-Stream Gamma = 1.382)

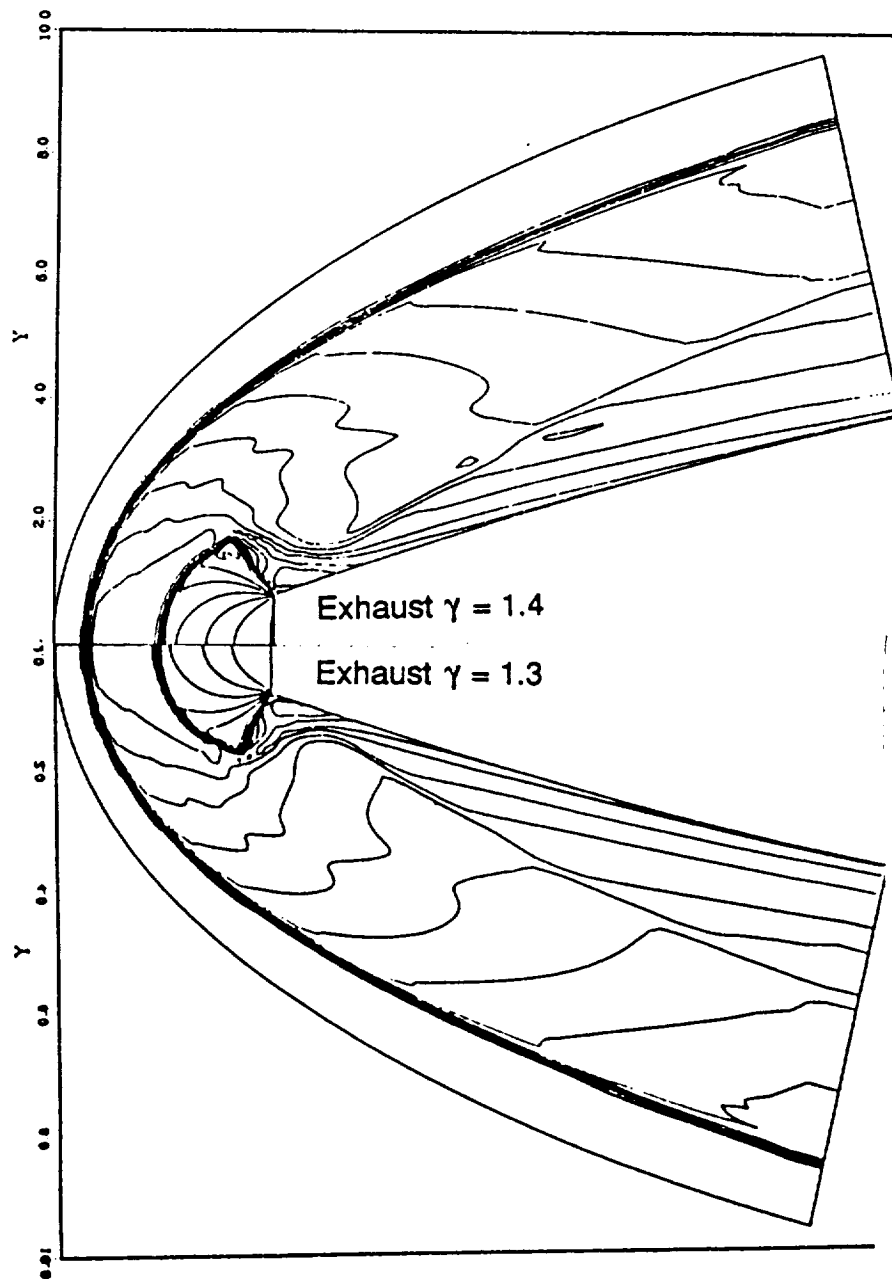


Figure 15: Mach Number Contour Comparison Between Exhaust Gamma Values of 1.4 and 1.3 (Free-Stream Gamma = 1.382)



**Appendix B**  
**Variable Gamma Computations for a**  
**Forward-Firing Space Shuttle Main Engine**

---

**REMTECH TECHNICAL NOTE**

---

**SUBJECT:** Variable Gamma Computations for a Forward-Firing Space Shuttle Main Engine

**DATE:** September 10, 1991

**AUTHORS:** Anthony J. Saladino and Sarat C. Praharaj

**CONTRACT NO.:** NAS8-38185

**PREPARED FOR:** NASA/MSFC

---

**Abstract**

A procedure for solving an axisymmetric SSME nozzle exhausting with an equivalent mass flow of two nozzles is presented for the return-to-launch-site (RTL) maneuver for an engine-out case. The algorithm incorporates a two-species variable gamma formulation along with diffusion terms associated with a species conservation equation. Coupling of this algorithm is accomplished explicitly to the Navier-Stokes PARC2DR and PARC3DR codes. Axisymmetric results indicate a very complicated flowfield with a bow shock extending to approximately 700 radii in front of the nozzle, and low temperatures on what would be an external tank (ET) aft of the nozzle.

**Background**

In the event of an SSME failure during the initial 160 seconds of the shuttle flight, a return-to-launch-site (RTL) maneuver will be implemented. The period of concern is the powered-pitch-around (PPA) maneuver where the vehicle is flying backward at angles-of-attack close to 180 deg. At these attitudes, a very complex flowfield involving severe free-stream/plume interaction effects results. This interaction includes mixing of a high Mach number hot exhaust gas from the two SSME's with the low Mach number free-stream flow. It is believed that the hot gas is basically frozen in concentration levels and is allowed to mix with air through convection and diffusion. The object of this technical note is to develop an algorithm for an axisymmetric case to study the effects of variable  $\gamma$  on the flowfield of a two-species mixture.

**Analysis****Species Solution Procedure**

The PARC2DR [1] and PARC3DR codes were used as the foundation for the Navier-Stokes solver, and the mass fraction,  $c$ , obtained from the species continuity equation (with and without diffusion) was coupled in an explicit fashion to the Navier-Stokes

equations via the variable gamma and diffusion terms if diffusion is considered. In two or three dimensions, the species continuity equation, after it was approximated by dropping the production term, is written in physical space coordinates  $(t, x, y)$  as

$$\frac{\partial \rho_i}{\partial t} + \nabla \cdot (\rho_i V) = \nabla \cdot (\rho D_{12} \nabla c_i) \quad (1)$$

where  $D_{12}$  is the binary diffusion coefficient,  $\rho_i$  and  $c_i$  are the density and mass fraction of species  $i$  respectively, and  $V$  is the velocity vector. Rewriting Eq. (1) using the definition of mass fraction

$$\frac{\rho_i}{\rho} = c_i \quad (2)$$

results in

$$\frac{\partial(\rho c_i)}{\partial t} + \nabla \cdot (\rho V c_i) = \nabla \cdot (\rho D_{12} \nabla c_i) \quad (3)$$

with  $\nabla = \frac{\partial}{\partial x} \bar{i} + \frac{\partial}{\partial y} \bar{j} + \frac{\partial}{\partial z} \bar{k}$  Eq. (3) can be reduced to the following form with the use of continuity

$$\rho \frac{Dc_i}{Dt} = \nabla \cdot (\rho D_{12} \nabla c_i) \quad (4)$$

where the global continuity equation was used to simplify Eq. (4) and  $\frac{D}{Dt}$  is the substantial derivative.

At this point Eq. (4) can be rewritten in a strong conservation form for three dimensions as

$$\frac{\partial(\rho c_i)}{\partial t} + \frac{\partial(\rho u c_i)}{\partial x} + \frac{\partial(\rho v c_i)}{\partial y} + \frac{\partial(\rho w c_i)}{\partial z} = \nabla \cdot (\rho D_{12} \nabla c_i) \quad (5)$$

where  $u, v$  and  $w$  are the velocities in the  $x, y$  and  $z$  directions, respectively. Either Eq. (4) or Eq. (5) can be used to compute the mass fractions. The reason for using the weak form instead of the strong conservation form will be discussed next.

Upon normalizing the variables according to reference values

$$\bar{\rho} = \frac{\rho}{\rho_{ref}}, \bar{u} = \frac{u}{a_{ref}}, \bar{v} = \frac{v}{a_{ref}}, \bar{p} = \frac{p}{\gamma_{ref} p_{ref}}, \bar{x} = \frac{x}{l_{ref}}, \bar{y} = \frac{y}{l_{ref}}, \bar{t} = t \frac{a_{ref}}{l_{ref}} \quad (6)$$

where  $a$  is the speed of sound, Eqs. (4) and (5) can be written as

$$\bar{\rho} \frac{Dc_i}{D\bar{t}} = \frac{1}{Re_{ref}} \bar{\nabla} \cdot \left( \bar{\mu} \frac{D_{12}}{Sc} \bar{\nabla} c_i \right) \quad (7)$$

$$\frac{\partial(\bar{\rho} c_i)}{\partial \bar{t}} + \frac{\partial}{\partial \bar{x}} (\bar{\rho} \bar{u} c_i) + \frac{\partial}{\partial \bar{y}} (\bar{\rho} \bar{v} c_i) + \frac{\partial}{\partial \bar{z}} (\bar{\rho} \bar{w} c_i) = \frac{1}{Re_{ref}} \bar{\nabla} \cdot \left( \bar{\mu} \frac{D_{12}}{Sc} \bar{\nabla} c_i \right)$$

$$Re_{ref} = \frac{\rho_{ref} a_{ref} l_{ref}}{\mu_{ref}}$$

$$Sc = \frac{\mu}{\rho D_{12}}$$

The Schmidt number,  $Sc$ , will be taken as a variable quantity in this development.

To transform Eqs. (6) and (7) from physical space to computational space  $(\xi, \eta, \zeta, \tau)$ , start with the functional relationship between the coordinates:  $\tau = t$ ,  $\xi = \xi(x, y, z, t)$ ,  $\eta = \eta(x, y, z, t)$ ,  $\zeta = \zeta(x, y, z, t)$ , so that the derivatives from physical to computational space become

$$\begin{aligned} \partial_t &= \partial_\tau + \xi_t \partial_\xi + \eta_t \partial_\eta + \zeta_t \partial_\zeta \\ \partial_x &= \xi_x \partial_\xi + \eta_x \partial_\eta + \zeta_x \partial_\zeta \\ \partial_y &= \xi_y \partial_\xi + \eta_y \partial_\eta + \zeta_y \partial_\zeta \\ \partial_z &= \xi_z \partial_\xi + \eta_z \partial_\eta + \zeta_z \partial_\zeta \end{aligned} \tag{8}$$

and the contravariant velocities are defined by

$$\begin{aligned} U &= \xi_t + u\xi_x + v\xi_y + w\xi_z \\ V &= \eta_t + u\eta_x + v\eta_y + w\eta_z \\ W &= \zeta_t + u\zeta_x + v\zeta_y + w\zeta_z \end{aligned} \tag{9}$$

where  $\xi_x = \frac{\partial \xi}{\partial x}$ , etc., are the metrics required for the transformation of the velocities  $u, v, w$  in the physical space to the computational space. The time derivatives of  $\xi, \eta$  and  $\zeta$  are zero since the grid is stationary.

The weak form of the species continuity equation in the computational space becomes

$$c_\tau + U c_\xi + V c_\eta + W c_\zeta = \frac{1}{Re_{ref}} \nabla \cdot \left( \mu \frac{D_{12}}{Sc} \nabla c \right) \tag{10}$$

where the overbars and subscript,  $i$ , have been dropped for convenience, and the derivatives are given by Eq. (8). In this form, the species conservation equation can be discretized and the left-hand side can be rewritten in direction-split or alternating-direction-implicit (ADI) form and the right-hand side is kept explicit:

$$[I + \Delta\tau U \partial_\xi][I + \Delta\tau V \partial_\eta][I + \Delta\tau W \partial_\zeta] c^{n+1} = RHSD \tag{11}$$

where

$$RHSD = c^n + \Delta\tau \left[ \frac{1}{Re_{ref}} \nabla \cdot \left( \mu \frac{D_{12}}{Sc} \nabla c \right) \right]^n \tag{12}$$

$I$  is the unit matrix,  $\partial_\xi = \frac{1}{\Delta\xi}$ , etc., and terms of second order in time have been neglected. At small  $\Delta\tau$ , these second-order terms are much smaller than terms of order  $\Delta\tau$ . Equation (11) would be advanced in time using current values at time step  $n$  as initial conditions for the next time stop  $n+1$  until steady-state convergence was achieved.

Similarly, the strong form of the species conservation equation can be transformed to the computational space after multiplying Eq. (7) by the inverse Jacobian  $J^{-1}$ , resulting in the delta form

$$[I + \Delta\tau U_\xi][I + \Delta\tau V_\eta][I + \Delta\tau W_\zeta] \Delta \left( \frac{\rho c}{J} \right)^{n+1} = RHS + RHSD \quad (13)$$

$$RHS = -\Delta\tau \left[ \left( \frac{\rho c U}{J} \right)_\xi + \left( \frac{\rho c V}{J} \right)_\eta + \left( \frac{\rho c W}{J} \right)_\zeta \right] \quad (14)$$

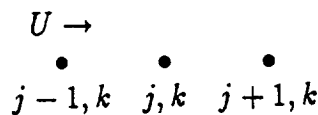
An additional term arising from this process

$$-\left( \frac{\rho c}{J} \right) \left[ \partial_\tau \left( \frac{1}{J} \right) + \partial_\xi \left( \frac{\xi_t}{J} \right) + \partial_\eta \left( \frac{\eta_t}{J} \right) + \partial_\zeta \left( \frac{\zeta_t}{J} \right) \right]$$

can be shown to be equal to zero [2].

The decision as to which of the diffusion equations to be solved — the weakly conserved form of Eq. (11) or the strongly conserved form of Eq. (13) — was made based upon the type of numerical stability scheme desired. Solving the strong conservation form of the species equation would require either central differencing that initially includes artificial dissipation (since Eq. (13) is the same form as the fluid dynamic, central difference equations in PARC), or upwinding. It was decided that since the species continuity equation can be quite easily upwinded, then Eq. (11) would be discretized accordingly.

One-sided differencing is utilized to bias the discretizing species continuity equation in the direction of the fluid flow; upwinding provides correct communication between neighboring points. For example, if computations are being performed at grid point  $(j, k)$ , and the



contravariant velocity  $U$  is in the direction toward  $(j, k)$  from  $(j-1, k)$ , then the derivative of  $c$  in the direction of  $\xi$  would be

$$c_\xi = c_{j,k} - c_{j-1,k}$$

Since  $c_{j,k}$  is unknown and  $c_{j-1,k}$  is a known value, upwinding also provides computational stability as it is naturally dissipative. Covering all possible signs for  $c$ , in two dimensions, upwinding for  $c$  in the  $\xi$ -direction becomes

$$\partial_\xi c = \begin{cases} c_{j,k} - c_{j-1,k} & , \quad U > 0 \\ \frac{c_{j+1,k} - c_{j-1,k}}{2} & , \quad U = 0 \\ c_{j,k} - c_{j+1,k} & , \quad U < 0 \end{cases} \quad (15)$$

and in the  $\eta$ -direction,

$$\partial_{\eta}c = \begin{cases} c_{j,k} - c_{j,k-1} & , V > 0 \\ \frac{c_{j,k+1} - c_{j,k-1}}{2} & , V = 0 \\ c_{j,k} - c_{j,k+1} & , V < 0 \end{cases} \quad (16)$$

Equations (15) and (16) are associated with the following form of Eq. (11), where absolute values have been taken of  $U$  and  $V$ :

$$[I + \Delta\tau|U|\partial_{\xi}][I + \Delta\tau|V|\partial_{\eta}]c^{n+1} = RHSD^n \quad (17)$$

The solution of Eq. (17) involves solving each direction separately:

$$[I + \Delta\tau|V|\partial_{\eta}]c^{n+1} = \overline{RHSD}^n \quad (18)$$

$$c^{n+1} = \overline{\overline{RHSD}}^n \quad (19)$$

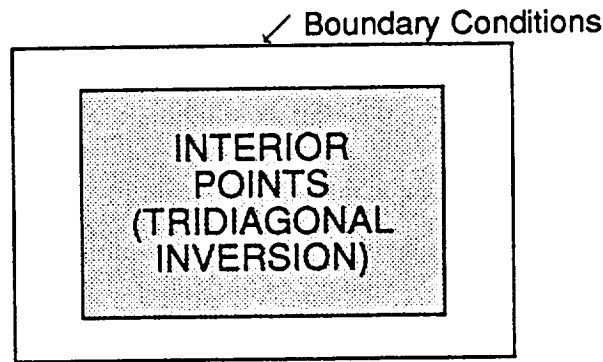
where

$$\overline{RHSD}^n = [I + \Delta\tau|U|\partial_{\xi}]^{-1}c^n \quad (20)$$

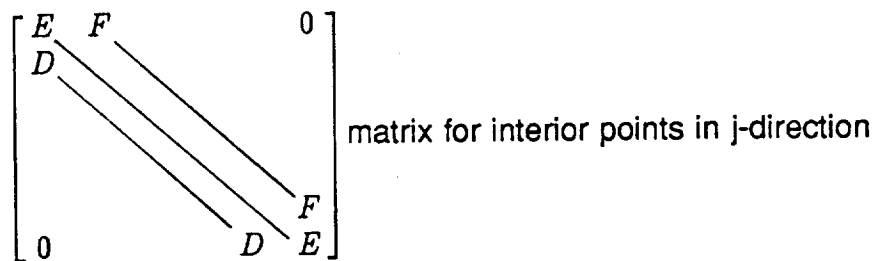
$$\begin{aligned} \overline{\overline{RHSD}}^n &= [I + \Delta\tau|V|\partial_{\eta}]^{-1} \overline{RHSD}^n \\ &= [I + \Delta\tau|V|\partial_{\eta}]^{-1}[I + \Delta\tau|U|\partial_{\xi}]^{-1}c^n \end{aligned} \quad (21)$$

Inversion of the bracketed terms in Eqs. (20) and (21) is accomplished by first noting that the resulting solution at point  $j, k$  will involve, at the condition  $U = 0$  (say) points  $j + 1, k$  and  $j - 1, k$ , which corresponds to an equation of no more than 3 points. Therefore, a tridiagonal solver is used to invert Eqs. (20) and (21). The value of  $\Delta\tau$  that is used in the species continuity equation is kept equal to the  $\Delta\tau$  computed from the Navier-Stokes flow solver portion of the code. Using the same  $\Delta\tau$  allows the solution to progress in "time" at the same rate in both the flow solver and the mass fraction solver. Furthermore, the tridiagonal inversion procedure incorporates the mass fraction boundary conditions implicitly to increase the accuracy of and reduce the convergence time of the species continuity solver. The reason for choosing an implicit, instead of an explicit, mass fraction solver is described briefly below.

When considering the explicit mass fraction solver, only the interior flowfield points are directly involved in the inversion procedure. The boundary points are imposed on the interior points explicitly. For example, if a boundary condition is fixed (free stream) or free (supersonic outflow), these conditions are set at the points corresponding to the indices associated with those boundaries. After this step, the flowfield points are inverted and the boundary points are supposed to feed back information into the interior through derivatives.



This is the same procedure which is used to invert the flow solver or Navier-Stokes (N-S) equations in PARC. However, whereas the interior points in the N-S solver transfer information to the boundary points via the derivative term in velocity, there is no such transfer from the interior [Eq. (17)] to the boundary for the mass fraction. For example, the tridiagonal terms in the matrix below are  $D$ ,  $E$  and  $F$ :



where  $E$  is along the diagonal and corresponds to the points  $(j, k)$ ,  $D$  corresponds to points  $(j - 1, k)$  and  $F$  corresponds to points  $(j + 1, k)$ . Equation (17) can be written for the  $j$ -direction only as

$$[I + \Delta\tau U \partial_\xi] c^{n+1} = RHSD^n \tag{22}$$

so that if  $U$  is greater than zero, then Eq. (22) can be written as

$$c_{j,k}^{n+1} + \Delta\tau U (c_{j,k}^{n+1} - c_{j-1,k}^{n+1}) = RHSD_{j,k}^n \tag{23}$$

for a single value of  $j$  and  $k$ . Equation (23) can be rewritten in matrix form for different values of  $j$  and constant  $k$  as

$$\begin{bmatrix} (1 + \Delta\tau U) & & & & 0 \\ (-\Delta\tau U)(1 + \Delta\tau U) & & & & \\ & \ddots & \ddots & \ddots & \\ 0 & & & (-\Delta\tau U) & (1 + \Delta\tau U) \end{bmatrix} \begin{bmatrix} c_{2,1} \\ c_{3,1} \\ \vdots \\ \vdots \\ c_{J_m,1} \end{bmatrix}^{n+1} = \begin{bmatrix} RHS_{D_{2,1}} \\ RHS_{D_{3,1}} \\ \vdots \\ \vdots \\ RHS_{D_{J_m,1}} \end{bmatrix}^n \quad (24)$$

where  $j$  goes from 2 to  $J_m$  ( $j = 1$  and  $j = j_{max}$  are boundaries),

$$J_m = j_{max} - 1 \quad (25)$$

and

$$\begin{aligned} D &= -\Delta\tau U \\ E &= 1 + \Delta\tau U \\ F &= 0 \end{aligned} \quad (26)$$

As Eq. (23) indicates for  $j = 2$ , values of  $c$  at location  $(1, k)$  would be required to evaluate  $c_{2,k}$ . However, location  $(1, k)$  is a boundary point and cannot be included in the vector of  $c$  values in Eq. (24) since this is a matrix inversion for interior points only. Consequently, the boundary information for  $c$  is not being communicated to the interior points, resulting in a non-changing value for  $c_{2,k}$ , regardless of the initial values (for  $U < 0$ , the same argument holds true at inflow boundaries; since there are boundaries in the forward-firing nozzle problem in which  $U < 0$  coexists with  $U > 0$ , the final value of  $c$  will be zero everywhere, regardless of the initial values, due to the influence of both types of boundaries on the interior point calculations).

Another way of describing the situation above is by making reference to the N-S equations. The explicit solution of the N-S equations as programmed in the original PARC code did not encounter such boundary communication problems for the solution to the interior points. The corresponding vector  $c$  in Eq. (24) would be a vector of  $Q$  values such that in a single direction,

$$[I + \Delta\tau \partial_\xi A] \Delta Q^{n+1} = RHS \quad (27)$$

where  $A$  is proportional to  $U$ . Since the N-S equations include terms related to the spatial derivative of velocity ( $(\partial_\xi U) Q^{n+1}$ ), the tridiagonal terms, for a boundary point at  $(j-1, k)$



and interior points at  $(j, k)$  and  $(j + 1, k)$ , are proportional to

$$\begin{aligned} D &\propto \Delta\tau U(j-1, k) \\ E &\propto 1 + \Delta\tau U(j, k) \\ F &\propto \Delta\tau U(j+1, k) \end{aligned} \quad (28)$$

The situation for the mass fraction equation is such that terms  $(U \partial_{\xi} c^{n+1})$  result, leading to

$$\begin{aligned} D, F &\propto \Delta\tau U(j, k) \\ E &\propto 1 + \Delta\tau U(j, k) \end{aligned} \quad (29)$$

where the  $U$  is now evaluated at point  $(j, k)$  only, so that there is no communication from the boundary to the interior through  $U$ . Although derivative terms for  $c$  do appear in Eq. (17), these are part of the solution vector  $c^{n+1}$  whose indices only include the interior points.

Therefore, the implicit method was applied to the solution of the mass fraction equation by appending the boundary condition equation to the interior point Eq. (17). The form for the boundary condition equations is different from those of the interior according to the boundary type — fixed (Dirichlet-type), isothermal (Neumann-type), etc. Along a solid boundary the mass fraction gradient is set to zero, while along a free boundary the mass fraction is either extrapolated from the interior flow as in the subsonic case or set equal to the value from the preceding grid point as in the supersonic case.

### Energy Equation

The contribution of diffusion to the energy equation appears in the heat flux term (neglecting the Dufour Effect)

$$q_D = \rho \sum_i h_i c_i V_i \quad (30)$$

where  $h_i$  is the enthalpy of component  $i$ , and the mass diffusion velocity  $V_i$  is related to Fick's Law of Diffusion [3] as

$$V_i \equiv \frac{-D_{ij}}{c_i} \nabla c_i \quad (31)$$

Normalizing Eq. (30) results in the following term in physical space

$$\bar{q}_D = \frac{1}{Re \bar{\rho}} \frac{1}{\bar{y}} \nabla \left( \frac{\bar{\mu} \bar{y}}{Sc} \nabla c_i \right) \quad (32)$$

where the Schmidt number,  $Sc$ , is defined by

$$Sc = \frac{\mu}{\rho D_{ij}} \quad (33)$$

The Schmidt number is allowed to vary in this formulation.

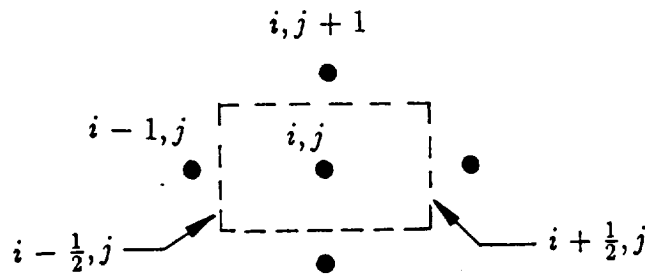
The diffusion coefficient was computed from the following equation obtained from the bifurcation approximation of Bird [4]

$$D_{ij} = \frac{\bar{D}}{F_i F_j} \tag{34}$$

where  $\bar{D} = \frac{1.719 \times 10^{-5}}{p} (T)^{1.659} \text{ cm}^2/\text{sec}$  with  $p$  in atmospheres and  $T$  in degrees Kelvin, and  $F_i = (m_i/26.7)^{0.489}$ , where  $m_i$  is  $i^{\text{th}}$  the species molecular weight. In discretizing  $D_{12}$ , it is advisable to smooth out the significant nonlinear variations in its value across adjacent cells. This reasoning, plus the differences in the cell sizes, suggests an average diffusion coefficient [5] which guarantees the flux entering an interface from the left of a discretized cell is equal to the flux exiting that interface at the right:

$$D_{i+\frac{1}{2}} = \frac{D_i D_{i+1} (\chi_{i+1} - \chi_i)}{D_{i+1} (\chi_{i+\frac{1}{2}} - \chi_i) + D_i (\chi_i - \chi_{i+\frac{1}{2}})} \tag{35}$$

where the species subscript 12 has been removed as it is understood that  $D$  is the binary diffusion coefficient, and where  $I + 1$  refers to the actual computational grid center and  $i + \frac{1}{2}$  indicates a cell interface:



**Additional Considerations**

Discretization of the species second derivative terms in computational space is accomplished according to whether the derivative is mixed or not mixed. For similar second-order derivatives, second-order central spatial difference operators are used; whereas, when applying a mixed derivative to  $c$ , average derivative values are computed at locations between the two grid points in a particular derivative direction.

$$\begin{aligned} \partial_\xi c_\xi &= (c_{j+1,k,l} - c_{j,k,l}) - (c_{j,k,l} - c_{j-1,k,l}) \\ \partial_\xi c_n &= \frac{1}{2} \left[ \frac{c_{j+1,k+1,l} - c_{j+1,k-1,l}}{2} + \frac{c_{j,k+1,l} - c_{j,k-1,l}}{2} \right] \\ &\quad - \frac{1}{2} \left[ \frac{c_{j,k+1,l} - c_{j,k-1,l}}{2} + \frac{c_{j-1,k+1,l} - c_{j-1,k-1,l}}{2} \right] \end{aligned} \tag{36}$$

Since the implicit equations are solved or inverted for the  $c_i$  along a single  $j$  or  $k$  or  $l$  line while changing one of the other indices (as opposed to solving for the species for the entire computational space in a single inversion), provisions were made to incorporate cyclic iteration between the possible sweep direction ordering.

Finally, to provide for axisymmetric diffusion, the species continuity

$$\rho \frac{\partial c_i}{\partial t} + \rho u \frac{\partial c_i}{\partial x} + \rho v \frac{\partial c_i}{\partial y} = \frac{\partial}{\partial x} \left( \rho D_{12} \frac{\partial c_i}{\partial x} \right) + \frac{1}{y} \frac{\partial}{\partial y} \left( \rho D_{12y} \frac{\partial c_i}{\partial y} \right) \quad (37)$$

in which  $v$  is the radial velocity and  $y$  is the radial coordinate, was transformed to computational space coordinates and coded in the upgraded PARC code, hereafter referred to as PARCSPEC.

### Species/Flow Solver Coupling

Coupling of the results from the species concentration solver to the fluid dynamic solver is accomplished in an explicit fashion. The continuity and momentum equations remained unchanged in form; however, due to the use of Wilke's mixture formula to calculate the transport properties, the energy equation changes its form to incorporate a variable thermal conductivity and  $c_p$ . The mass fractions, along with the species gas constants, are used to compute  $\gamma$  at every point in the flowfield, which replaces the constant  $\gamma$  required in the original version of PARC. The ratio of specific heats  $\gamma$  for the mixture is found as

$$\gamma_m = \frac{c c_{p1} + (1 - c)c_{p2}}{c c_{v1} + (1 - c)c_{v2}} = \frac{c_{p_m}}{c_{v_m}} \quad (38)$$

$c_p$  and  $c_v$  are the specific heats at constant pressure and constant volume, respectively, for species 1 or 2, and subscript  $m$  denotes a mixture. Coupling between the species continuity equation and the flow solver is accomplished through an equation of state of the form

$$p = (\gamma_m - 1)\rho e_{int} \quad (39)$$

where  $p$  is pressure,  $\rho$  is density and  $e_{int}$  is internal energy, with  $\gamma_m$  following from Eq. (38).

To accommodate the difference in the free-stream and exit nozzle value of gamma in the normalization of PARC, the following changes had to be made.

Within the PARC code, the equation of state variables are normalized with respect to free-stream conditions as indicated in Eq. (6) plus the additional terms

$$\bar{T} = \frac{T}{T_{ref}} \quad \bar{a} = \frac{a}{a_{ref}} \quad (40)$$

where  $T$  is the temperature, and  $a$  is the speed of sound.

In the calculation of the speed of sound or temperature, the updated code utilizes the nondimensional equations:

$$a^2 = \frac{\gamma_m p}{\rho} \quad \longrightarrow \quad \bar{a}^2 = \frac{\gamma_m \bar{p}}{\bar{\rho}} \quad (41)$$

$$p = \rho RT \longrightarrow \bar{T} = \frac{\gamma_{ref} \bar{p}}{\bar{\rho}} \quad (42)$$

where the  $\gamma_m$  in Eq. (41) was equal to  $\gamma_\infty$  in the original code [1], since  $\gamma$  was the same at every point in the flow. For the present variable gamma approach, the constant GAMAREF was changed to GAMMA(J,K) (as computed from Eq. 38), with the reference or constant (free-stream) value GAMAFS used in the calculation of temperature only and the local value of GAMMA(J,K) used to determine the speed of sound.

One final consideration is needed to correctly account for the two-species variable gamma effects on the flowfield. This becomes important whenever the two species have different molecular weights. The equation of state is written in the usual form for a single species as

$$p = \rho RT \quad (43)$$

where  $R = \frac{\hat{R}}{m}$ , and  $\hat{R}$  is the universal gas constant. Equation (43) can be normalized as

$$\begin{aligned} \bar{p} \rho_{ref} a_{ref}^2 &= \bar{p} \rho_{ref} R \bar{T} T_{ref} \\ \text{or,} \quad \bar{p} &= \bar{\rho} \bar{T} \frac{T_{ref} R}{a_{ref}^2} \\ \text{or,} \quad \bar{p} &= \frac{\bar{\rho} \bar{T}}{\gamma_{ref}} \end{aligned} \quad (44)$$

since

$$\gamma_{ref} R T_{ref} = a_{ref}^2 \quad (45)$$

For two species,  $R$  must be replaced by the gas constant for the mixture,  $R_m$ :

$$\begin{aligned} p &= \rho R_m T \quad \text{where,} \\ R_m &= \frac{\hat{R}}{m_m} \end{aligned} \quad (46)$$

and  $m_m$  is the local mixture mass, so that upon normalizing Eq. (46),

$$\bar{p} = \bar{\rho} \bar{T} \frac{R_m T_{ref}}{a_{ref}^2} \quad (47)$$

The mixture gas constant involves a summation over each species  $i$ ,

$$R_m = \sum_i c_i R_i \quad (48)$$

$$\begin{aligned}\bar{p} &= \bar{\rho} \bar{T} \frac{T_\infty}{a_\infty^2} \sum_i c_i R_i \\ &= \frac{\bar{\rho} \bar{T}}{\gamma_{ref} R_{ref}} \sum_i c_i R_i \quad \text{from Eq. (45)}\end{aligned}\quad (49)$$

Also,

$$R_i = c_{p_i} - c_{v_i} \quad (50)$$

Substituting Eq. (50) into Eq. (49) results in

$$\begin{aligned}\bar{p} &= \frac{\bar{\rho} \bar{T}}{\gamma_{ref}} \frac{\sum_i c_i (c_{p_i} - c_{v_i})}{R_{ref}} \\ &= \frac{\bar{\rho} \bar{T}}{\gamma_{ref}} \frac{c_{p_m} - c_{v_m}}{R_{ref}} \quad \text{from Eq. (38)} \\ &= \frac{\bar{\rho} \bar{T}}{\gamma_{ref}} \frac{(\gamma_m - 1) c_{v_m}}{R_{ref}}\end{aligned}\quad (51)$$

Finally, the equation of state for two species can retain the form it had for a single species by writing Eq. (51) as

$$\bar{p} = \frac{\bar{\rho} \bar{T}}{\bar{\gamma}} \quad (52)$$

where

$$\bar{\gamma} = \frac{\gamma_\infty R_\infty}{(\gamma_m - 1) c_{v_m}} \quad (53)$$

A similar normalization of the first law of thermodynamics results in

$$\bar{p} = (\gamma_m - 1) \bar{\rho} \overline{e_{int}} \quad (54)$$

in nondimensional form. The temperature is then obtained from Eq. (52) in place of Eq. (42).

## Results

In order to validate the above algorithm, a few cases were examined. Results for a forward-firing sonic jet [6] for two cases  $\gamma_N = 1.4$  and  $\gamma_N = 1.3$  at a  $\gamma_{fs} = 1.4$  compared very well with experimental results. Diffusion was not invoked in the code in that study.

The engine-out condition on a PPA maneuver in an RTLS trajectory was modeled as a single nozzle with a mass flux equal to twice that of one SSME, and with a radius scaled to  $\sqrt{2}$  times a single SSME radius. A grid was created with INGRID [7] assuming the nozzle to be a simple outflow plane, with a straight afterbody with a radius of  $1.05 r$ ; the location of flow impingement on the external tank (ET) (which is not part of the grid model) would then be approximated by examining the solution in the region where the ET would exist in relation to the SSME's.

Conditions on the nozzle and free stream are as follows:

Table 1: Nozzle and Free-stream Conditions

	Nozzle	Free Stream
$\rho$ (lbm/ft <sup>3</sup> )	$3.226 \times 10^{-3}$	$9.0328 \times 10^{-6}$
T (°R)	2193.0	409.18
p (lbf/in <sup>2</sup> )	2.619	$1.3681 \times 10^{-3}$
m (lbm)	14.132	28.858
Mach Number M	-4.67	1.464
$\gamma$	1.20	1.40

The free-stream conditions were taken as the reference conditions in PARCSPEC.

This study focuses on the possible impact on the thermal environment caused by the SSME firing in the same direction as the Shuttle flight direction. At a flight angle  $\alpha$  of 180 deg, the plume impingement on the ET may not occur; however, at a flight angle of 135 deg, the free-stream air may force back the plume which is expanding from the nozzle into a shear layer that impinges the ET.

#### Axisymmetric SSME

The extent of the grid ranges from 1454 (two-nozzle equivalent) radii in front of the nozzle and 300 radii behind the nozzle, exit plane along the axis, and 2800 radii in the radial direction. A grid size of 140 points (axially) and 340 points (radially) was constructed with clustering near the axis and nozzle expansion region (Fig. 1). The nozzle is located at the  $x = 0$  location on the figure. The large size of the grid prevents the nozzle from being seen on this scale. Due to the very large physical extent of this grid, the grid lines are highly compacted in the vicinity of the nozzle, and more sparse as the grid extends far away from the body. Smoothness between adjacent grid cells was adhered to as best as possible to limit the nonlinearities associated with computations across such cells. Diffusion was neglected in this set of runs.

Convergence was difficult to obtain when the conditions specified in Table 1 were imposed at once. Instead, the nozzle conditions were taken at their specified values, except that  $\gamma_N$  was set to 1.4, and the free-stream conditions were adjusted gradually between restart files until the specified conditions were reached. Each set of free-stream conditions was run to a reasonable convergence before adjusting the conditions for the next case.

Contour plots of streamlines are shown in Figs. 2-3 for the case where  $\gamma_N = \gamma_{fs} = 1.4$  and the molecular weight  $m_N = m_{fs} = 28.858$ . The demarcations on the axis specify a range of 200 radii. A smooth variation in the streamlines is indicated in these figures, where the flow turns back at a point equivalent to 180 radii in front of the nozzle on the axis.

The next step in the convergence process was to reduce  $\gamma_N$  and  $m_N$  from 1.4 and 28.858, respectively, to 1.2 and 14.132, which corresponds to the  $H_2 - O_2$  system value. Results for the PPA conditions at  $\alpha = 180$  deg are presented in Figs. 4 – 8. The bow shock is located at roughly 700 radii in front of the nozzle while the nozzle shock occurs at 250 radii before the nozzle (Fig. 4). Due to the high nozzle pressure and low atmospheric conditions, the nozzle shock extends a great distance away from the nozzle and is highly curved as a large expansion from the axis to the free-stream condition must occur. The values of gamma (Fig. 5) indicate a smooth variation in the extent of the mixing region. Along the axis, supersonic Mach numbers of Fig. 6 show the increase of the value of 4.87 at the nozzle to 10.9 about 170 radii before the nozzle and then a decrease to zero at an X/R value of 200 where the two opposing flows stagnate. The behavior of the streamlines (Fig. 7) in front of the nozzle is due to the small gamma and molecular weight of the exhaust gas compared to that shown in Fig. 2. Clearly, the hot plume gas does not impinge on what would be the ET. A close view of the nozzle exit temperature profiles (Fig. 8) indeed verifies the low temperature in the region just behind the exhaust. In fact, the temperature is close to the free-stream value.

### Results In Progress

When the nozzle gamma was changed from 1.4 to 1.2, it was found that the streamlines fluctuated over a large distance along the outflow plane. This is reasoned to be caused by flowfield and exit plane coupling which could be eliminated if the exit plane were extended farther downstream. An extension of 400 radii — or a total of 700 radii — comprise this new grid, and results are being generated at the current time.

In addition, the diffusion upgrade to the two species methodology is being checked out for the two-dimensional sonic jet to ascertain the effect that diffusion has on the variable gamma solution.

To study the three-dimensional effects on the RTLS flowfield, the axisymmetric grid was revolved about the axis and points between the outer boundary and the bow shock were eliminated, as these points were originally employed to capture the unknown location of the shock. Eighteen planes comprise a total space of 180 deg with half of the domain being a mirror image of the constructed grid domain. Computations are in progress for this case.

### References

1. Liver, P. A. and Praharaj, S. C., "Upgrade of and Numerical Experiment with PARC for Hypersonic Flow over a Hemisphere-Cylinder Configuration," REMTECH Report RTR 181-01, Feb. 1989.
2. Pulliam, T. H., "Euler and Thin Layer Navier-Stokes Codes: ARC2D, ARC3D," Notes for Computational Fluid Dynamics User's Workshop, The University of Tennessee Space Institute, Tullahoma, TN, March 12-16, 1984.
3. Kuo, K. K., *Principles of Combustion*, John Wiley and Sons, 1986, p. 638.

4. Evans, R. M., "Boundary Layer Integral Matrix Procedure," Aerotherm Report UM-75-64, Aerotherm Division/Acurex Corporation, Mountain View, California, July 1975.
5. Oran, E. S. and Boris, J. P., *Numerical Simulation of Reactive Flow*, Elsevier Science Publishing Co., Inc., 1987, pp. 237-240.
6. Saladino, A. J. and Praharaj S. C., "Two-Species Variable Gamma Formulation for a Forward-Firing Rocket Nozzle," AIAA Paper 91-1349, 26th Thermophysics Conference, June 24-26, 1991, Honolulu, HI.
7. Dorrell, E. W., Jr. and Soni, B. K., "INGRID: Interactive Two-Dimensional Grid Generation," AEDC-TR-86-49, Arnold Engineering Development Center, Tullahoma, TN, Feb. 1987.



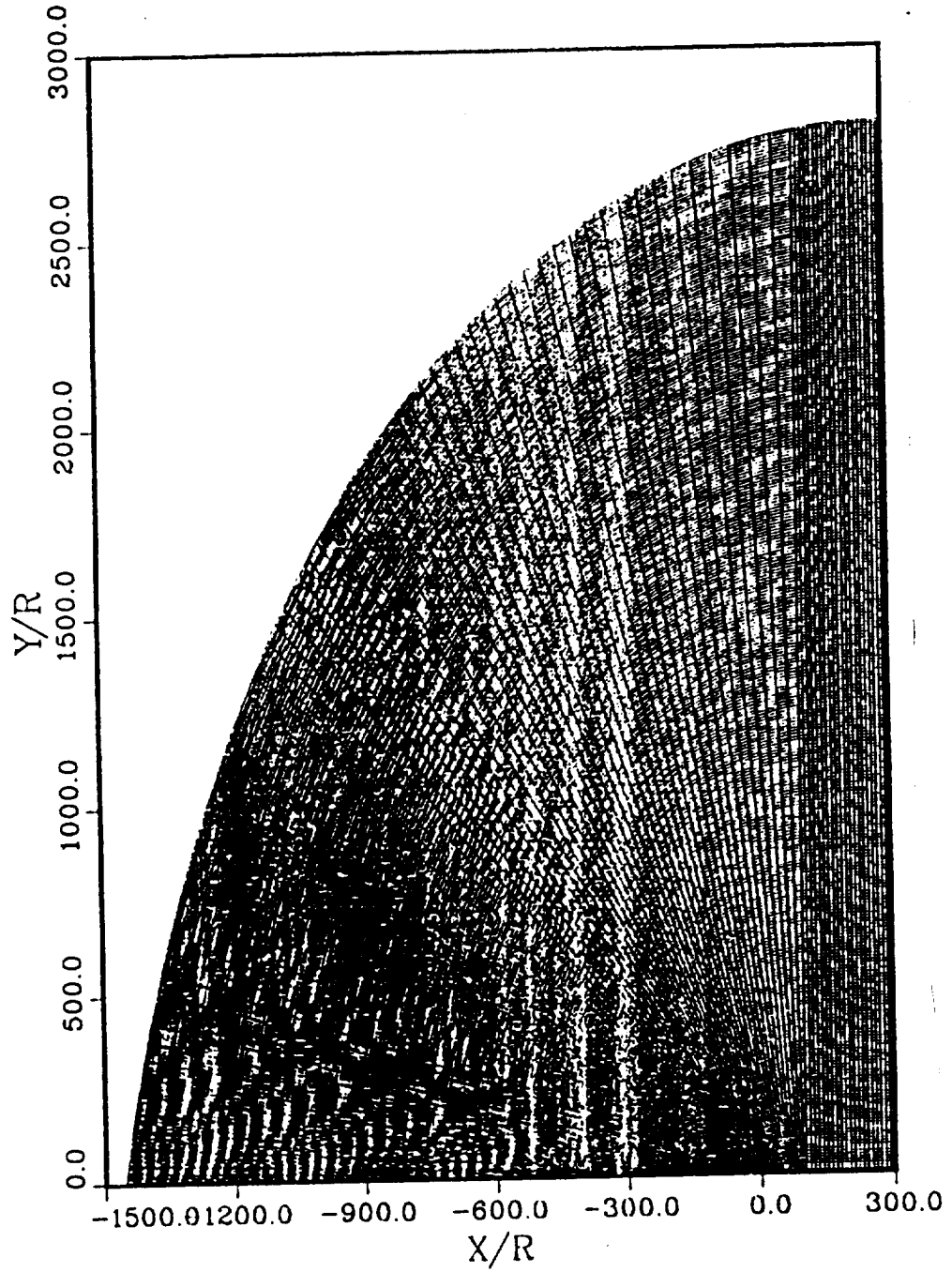


Figure 1: Grid

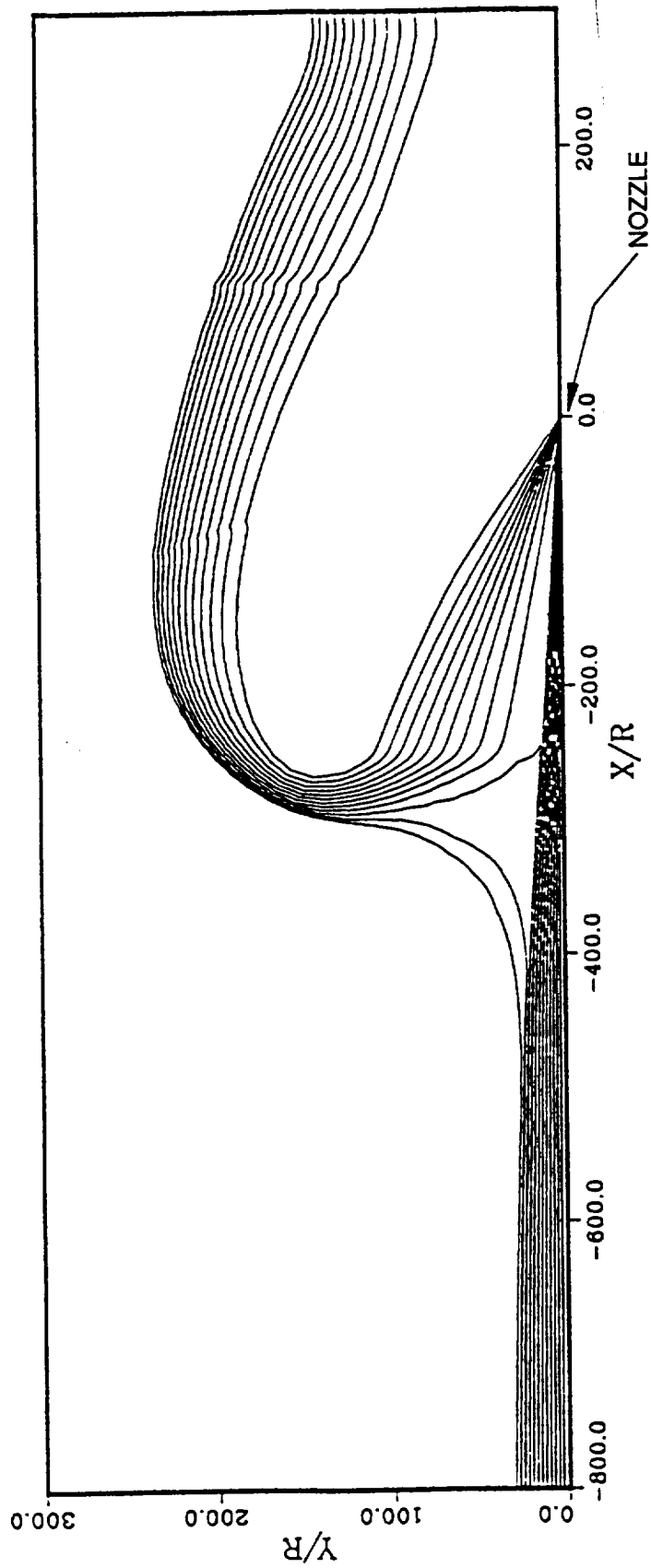


Figure 2: Streamlines for  $\gamma_N = \gamma_{fs} = 1.40$

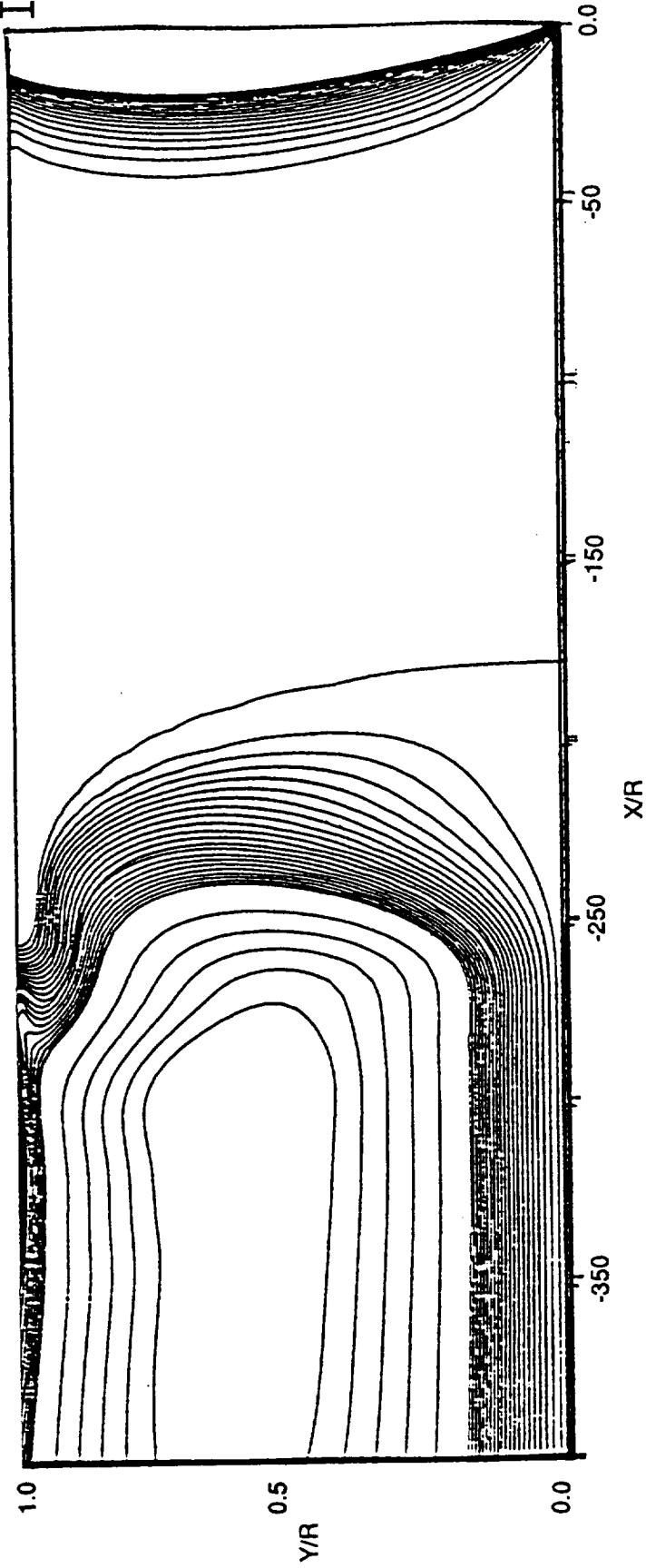


Figure 3: Streamlines Along Axis for  $\gamma_N = \gamma_{fs} = 1.40$

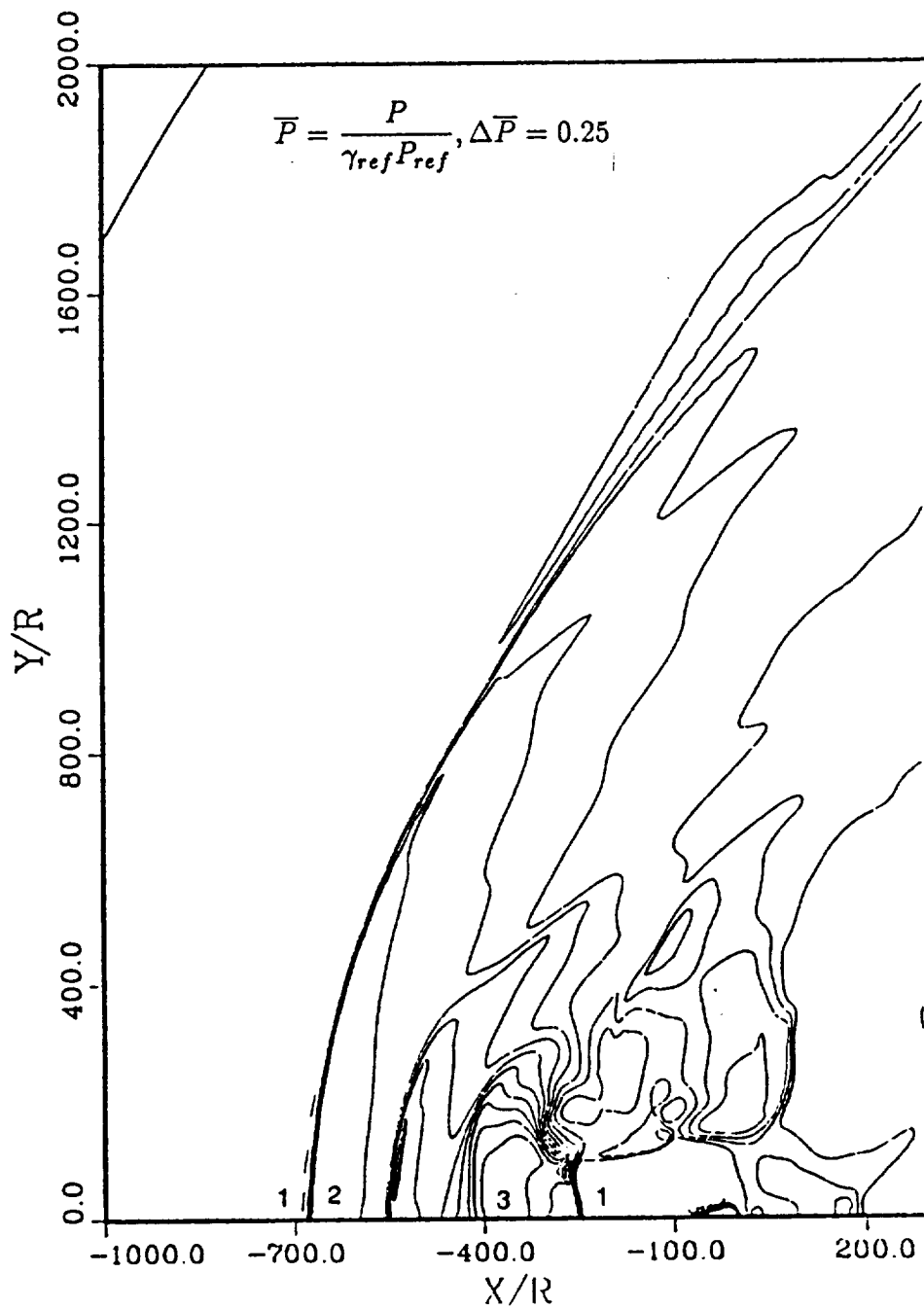


Figure 4: Pressure Contours for  $\gamma_N = 1.20, \gamma_{fs} = 1.40$

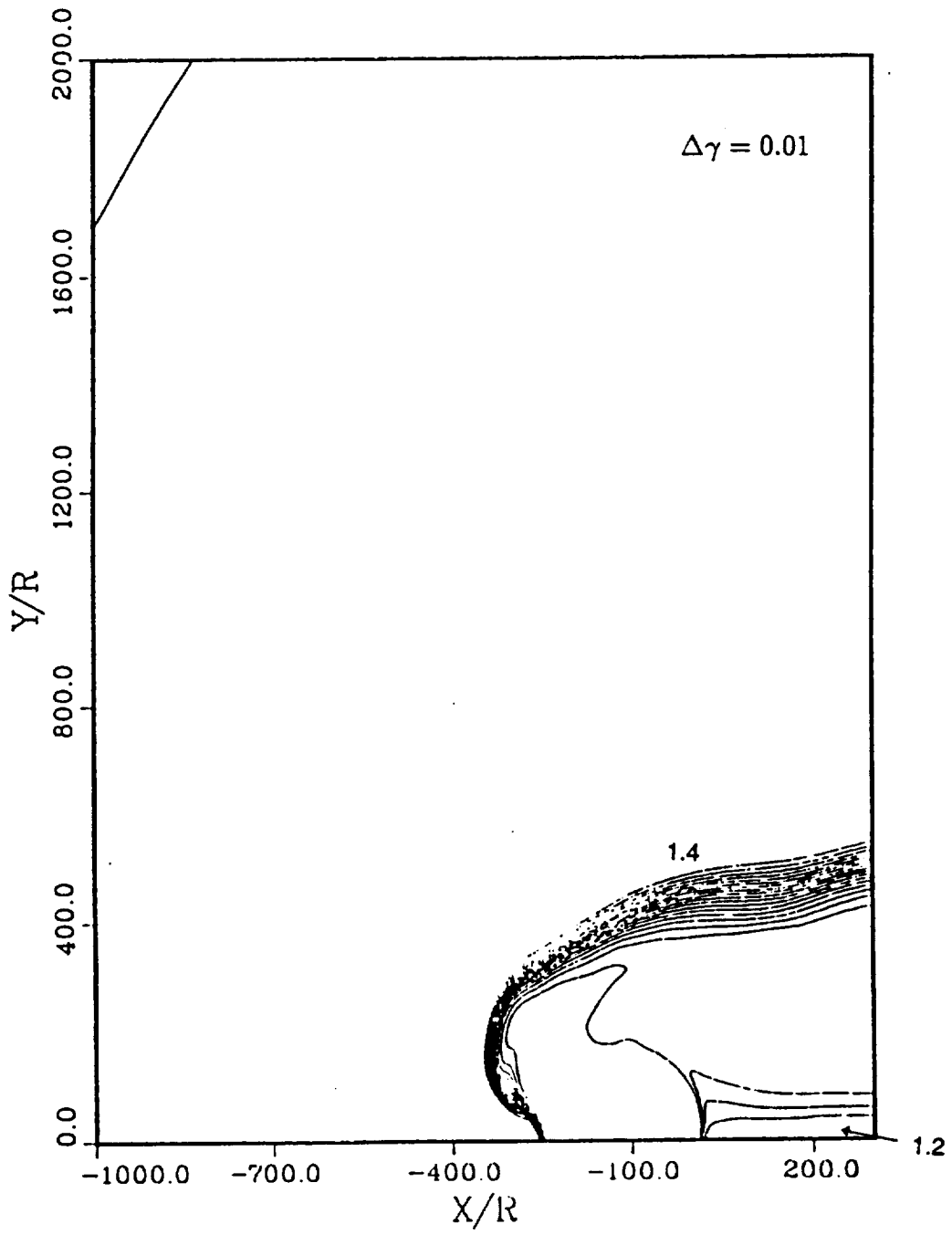


Figure 5: Gamma Contours for  $\gamma_N = 120$ ,  $\gamma_{fs} = 1.40$

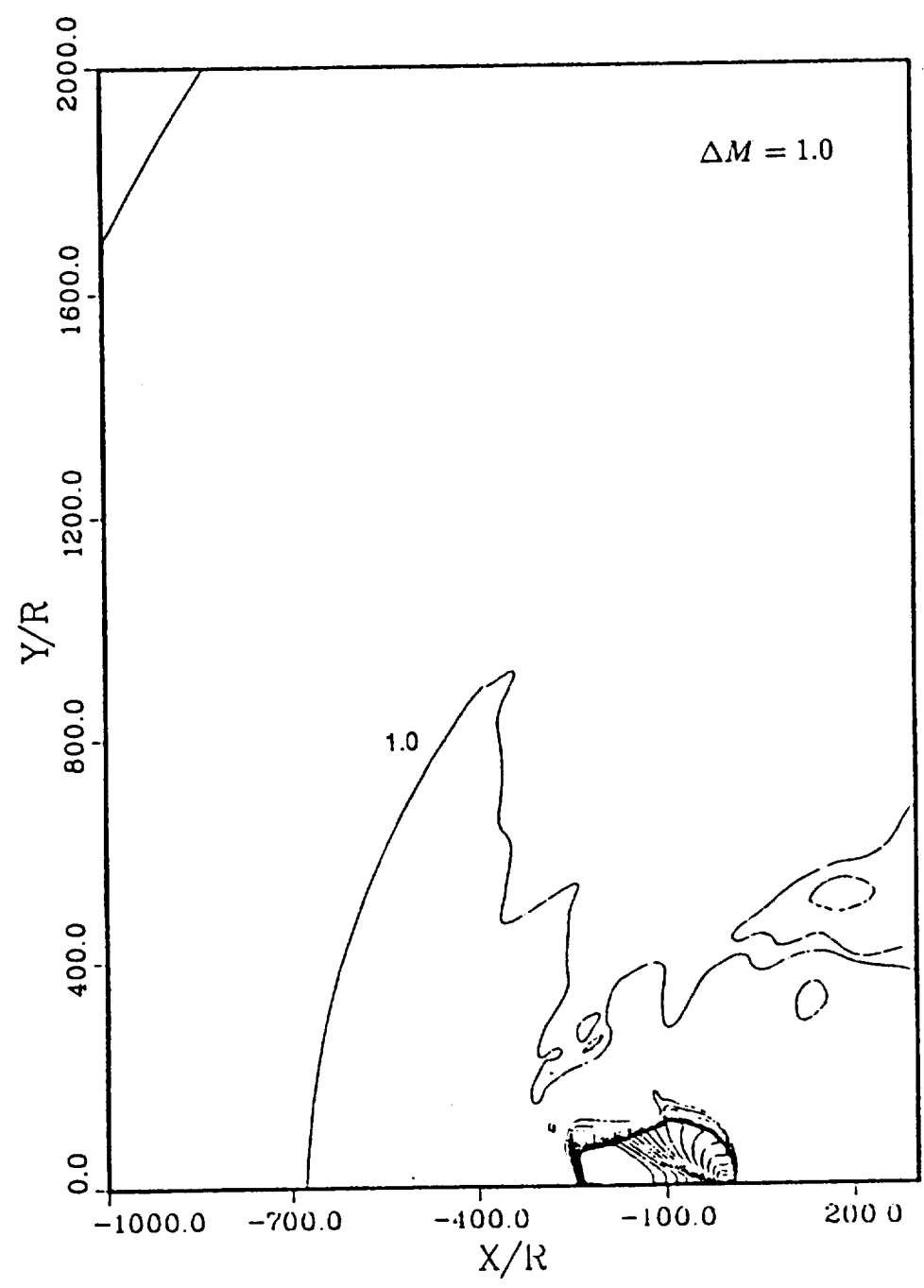


Figure 6: Supersonic Mach Contours for  $\gamma_N = 120$ ,  $\gamma_{fs} = 1.40$

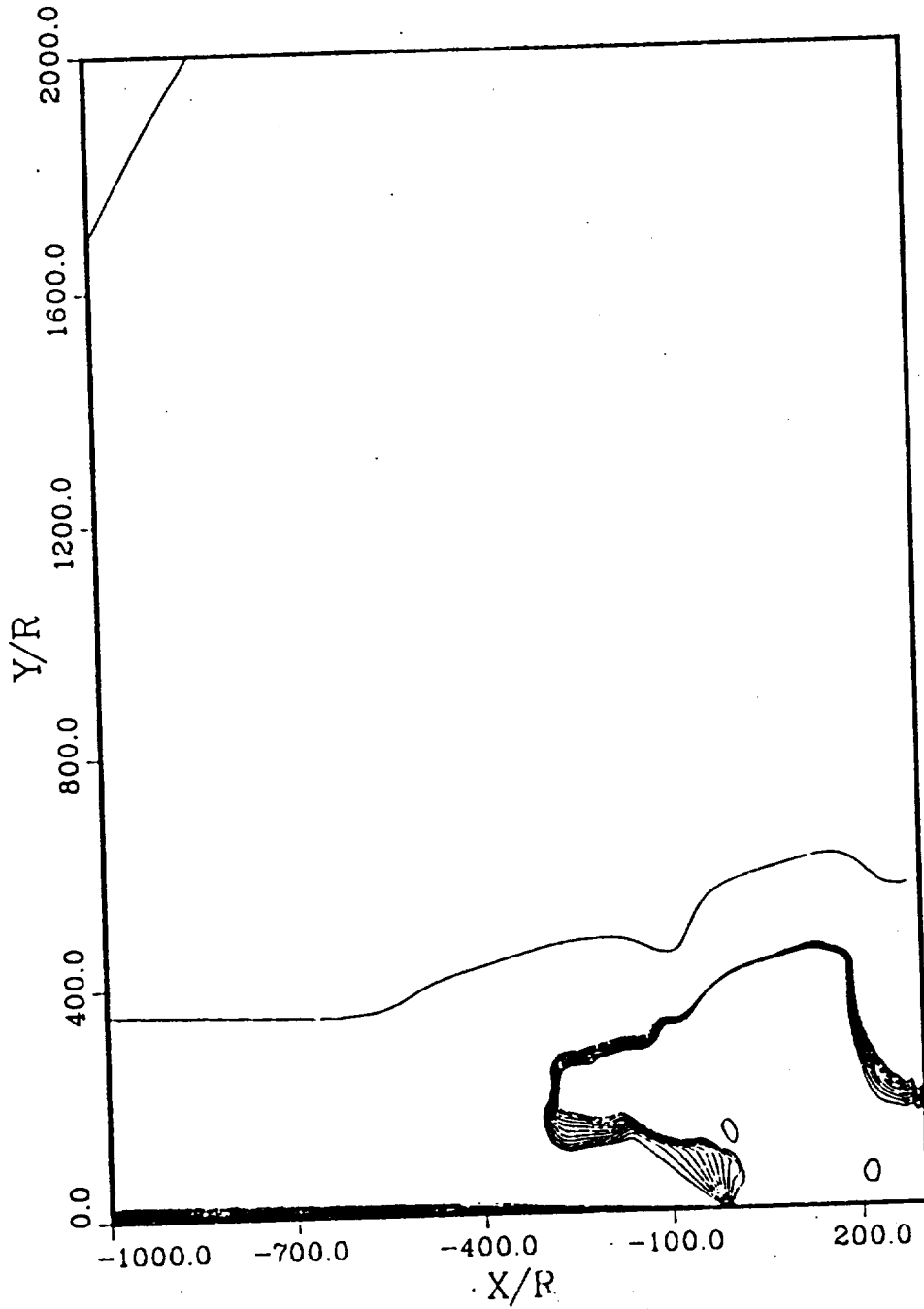


Figure 7: Streamlines for  $\gamma_N = 120$ ,  $\gamma_{fs} = 1.40$

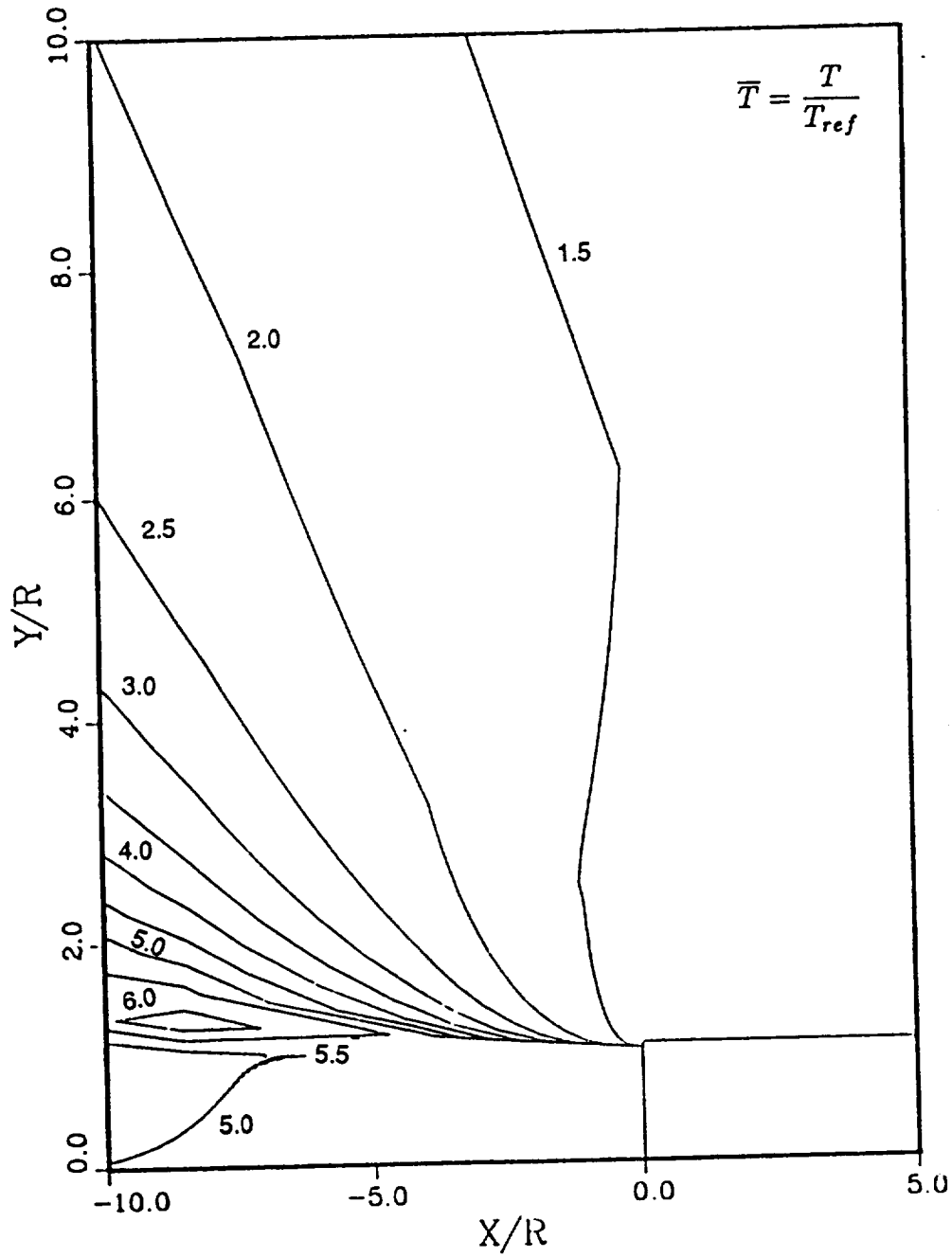


Figure 8: Temperature Contours for  $\gamma_N = 120, \gamma_{fs} = 1.40$